The influence of temperature on ion transport in nanofiltration membranes

by

Yagnaseni Roy

S.M., Mechanical Engineering
Massachusetts Institute of Technology, 2015

B.Tech. Mechanical Engineering
SRM University, 2013

SUBMITTED TO THE DEPARTMENT OF MECHANICAL ENGINEERING IN PARTIAL FULMILLMENT OF THE REQUIREMENTS FOR THE DEGREE OF

Doctor of Philosophy in Mechanical Engineering
AT THE
MASSACHUSETTS INSTITUTE OF TECHNOLOGY
September 2018

Signature of Author:

_____

Department of Mechanical Engineering
August 15, 2018

Certified by:

_____

John H. Lienhard V
Abdul Latif Jameel Professor
Thesis Supervisor

Accepted by:

_____

Rohan Abeyaratne
Chairman, Committee on Graduate Students

THIS PAGE IS INTENTIONALLY LEFT BLANK

The influence of temperature on ion transport in nanofiltration membranes

by

Yagnaseni Roy

Submitted to the Department of Mechanical Engineering
On August 15, 2018, in partial fulfillment of the
requirements for the degree of
Doctor of Philosophy in Mechanical Engineering

Abstract

Nanofiltration (NF) is a pressure-driven membrane-based solution treatment technology, similar to reverse osmosis (RO). The niche set of applications for NF includes those requiring selectivity between monovalent ions and multivalent ions. Incoming streams to be treated can occur over a wide range of temperature, usually between 20-100°C. The advantage of operating NF at higher temperatures is increased water recovery, while the key drawback is diminished salt retention. Although the change of these performance metrics is widely reported in literature, few sources explain the causative mechanisms. Temperature-variation of the mobilities of both solute and solvent species, the solute diffusivity and solvent viscosity are well-studied and are used to explain changes in transport through the membrane in most literature. However, NF membranes are defined by several structural and charge-based properties, which are likely to be affected by temperature. This thesis elucidates the effect of individual membrane properties and mobilities on NF permeate quality, and finally compares sets of parameters on the extent to which they explain the change in NF selectivity with temperature change. Modeling results show that neither membrane parameter changes nor mobilities can alone explain selectivity changes with temperature. With increasing pressure, however, the net effect of membrane parameters increasingly overshadows that of the mobilities.

As mentioned previously, NF is used particularly for monovalent-multivalent ion separations. The study of 'fractionation,' involving separation of sodium-chloride from sodium-sulfate is one such application, and is often conducted between 20-50°C. Previous studies do not indicate whether selectivity between the charged species improves or deteriorates at higher temperature. In this thesis, a selectivity metric, M, is introduced and an analytical framework is established to explain its variation with temperature variation, as well as other membrane and operating parameters. The conclusion is that selectivity decreases at higher temperature, which can be mitigated by design-focus on enhanced charge acquirement by the membrane at elevated temperature.

The final segment of this work introduces a common modeling framework for pressure-driven (NF and RO) and osmotically driven membrane processes (forward osmosis, FO) to identify both similarities and dissimilarities in salt transport mechanisms. RO and FO membranes are traditionally considered non-porous membranes, while NF membranes are known to possess nanometer-sized pores. However, experimental and spectroscopy results in the past decade report

detection of pores in RO and FO membranes. The modeling results in this thesis show that all three membranes can be modeled as porous, the key distinction being that the pressurized modes allow salt-water transport coupling.

Thesis Supervisor: John H. Lienhard V
Title: Abdul Latif Jameel Professor

Acknowledgements

I would like to thank Prof. Lienhard for his guidance and the opportunity to work in his group. All of my previous and current lab-mates have contributed to my learning and growth in the last five years at MIT. I would like to give a special mention to Jaichander Swaminathan, Emily Tow and Alex Benjamin for interesting discussions that led to new channels of research. I am grateful to the members of my doctoral committee, Prof. Rohit Karnik and Mr. Leon Awerbuch, for the stimulating interactions during the committee meetings, which constantly shaped my work in a more useful direction. My family has been my pillar of support through the numerous ups and downs in my research path. I would like to give a special mention to Debanjan for the help and support especially during my last few weeks at MIT.

THIS PAGE IS INTENTIONALLY LEFT BLANK

Contents

THIS PAGE IS INTENTIONALLY LEFT BLANK

List of Figures

THIS PAGE IS INTENTIONALLY LEFT BLANK

List of tables

Nomenclature

A	area	m^2
B	solute permeability of membrane active layer	$m\ s^{-1}$
A_k	porosity of membrane	
C	concentration	$mol\ m^{-3}$
C_X	membrane volumetric charge density	$mol\ m^{-3}$
C_p	heat capacity at constant pressure	$kJ\ kg^{-1}\ K^{-1}$
CP	Concentration polarization	
d	thickness of a single water molecule (0.28 nm) or pipe diameter (Chapter 6)	m
D	solute diffusivity	$m^2\ s^{-1}$
f	flash flow rate	$kg\ s^{-1}$
F	Faraday's constant	$C\ eq^{-1}$
h	enthalpy	$kJ\ kg^{-1}$
$\dot{h}$	convective heat transfer coefficient	$W\ m^{-2}\ K^{-1}$
i_v	Van 't Hoff coefficient	
J	solute flux	$mol\ m^{-2}s^{-1}$
J_w	solvent permeation flux	$m\ s^{-1}$
k	external mass transfer coefficient	$m\ s^{-1}$
K_{eff}	Effective salt mass transfer coefficient	$m\ s^{-1}$
K_c	hindrance factor for convection	
K_d	hindrance factor for diffusion	
L	latent heat	$kJ\ kg^{-1}$
LMTD	Logarithmic Mean Temperature Difference	^oC
$L_{support}$	support layer thickness	m
m	mass flow rate	$kg\ s^{-1}$
M	Fractionation metric	
N	number of stages in MSF	
N_c	number of components in the mixture	
P	pressure	Pa
PR	performance ratio	
ΔP_{net}	net driving pressure	Pa
r_i	Stokes radius of solute	m
r_{pore}	pore radius of membrane	m
R	universal gas constant	$J\ mol^{-1}\ K^{-1}$
Rej	rejection ratio	
sA	specific area requirement	$m^2\ s\ kg^{-1}$
T	temperature	K
TBT	top brine temperature	^oC

TDS	Total Dissolved Solids	mol m^{-3}
TF	Salt flux towards feed	mol $m^{-2}s^{-1}$
TM	Salt flux towards membrane	mol $m^{-2}s^{-1}$
ΔT	inter-stage temperature drop	^oC
u	flow velocity in feed heater pipes	m s^{-1}
U	overall convective heat transfer coefficient	W m^{-2} K^{-1}
V	cross-flow velocity	ms^{-1}
x	distance normal to membrane or quality factor (Chapter 6) (unitless)	m
Δx	membrane active layer thickness	
X	Operating condition dummy variable (pressure or temperature)	
y	salinity	mg kg^{-1}
z	valence of ionic species	

Greek symbols

δ	active layer thickness or boiling point elevation (Chapter 6)	m or ^oC
ε	dielectric constant of medium	
ε^*	dielectric constant of oriented water layer inside pores	
ζ_1	potential gradient at feed-membrane interface	V m^{-1}
ζ_2	potential gradient at draw-support interface	V m^{-1}
Θ	effective thickness ratio	
λ	ratio of solute Stokes radius to pore radius	
μ	Dynamic viscosity	Pa-s
ν	kinematic viscosity	m^2 s^{-1}
π	osmotic pressure	Pa
ρ	density	kg m^{-3}
τ	tortuosity	
Φ_i	steric partitioning factor	
Φ_B	Born solvation factor for partitioning	
ϕ	porosity	
ψ	membrane potential	V
ω	dummy variable used in Appendix E	

Subscripts

b	brine
bh	brine heater
c	convective
d	diffusive or distillate (Chapter 6)
D	Donnan potential
end	brine exiting MSF
f	feed solution

$feed$	feed
$flow$	Related to water flow
g	gas
i	ionic species or stage number in MSF (Chapter 6)
in	inlet
m	feed-membrane interface
out	outlet
p	permeate just outside the membrane or point just outside the active layer, within the support layer (cf. Fig. 1)
$pore$	inside pore
s	Salt or steam (Chapter 6)
sat	corresponding to saturation state
$support$	Relating to membrane support layer
v	vapor
w	solvent
water-side	water side (inside) of pipe carrying the incoming seawater through feed heater
∞	bulk

Dimensionless Parameters

$R_{C/E}$	ratio between the convective and electromigrative terms
$R_{E/D}$	ratio between the electromigrative and diffusive terms

THIS PAGE IS INTENTIONALLY LEFT BLANK

1. Introduction

Nanofiltration (NF) membranes evolved from reverse osmosis (RO), initially called 'loose RO membranes'. Its niche set of applications comprises those where selectivity between monovalent and multivalent ions is required (1,2). While the extremely small pore size in RO allows almost 100% removal of solute species, the nanometer-size pores in NF allows passage of various solutes to be determined by a combination of various factors (3). These factors are broadly of two kinds: membrane parameters and species mobilities (4). Membrane parameters either define geometric aspects of the passages through the membrane, such as pore size or effective path length, or charge-acquirement by the membrane material. The ion diffusivity and water viscosity together constitute the 'mobility' factors and indicate the species' motion rate. NF feed solutions can occur over a wide range of temperature, for example seasonal variations cause gulf seawater temperatures between 20-40^{o}C (5,6), while industrial effluent such as that from battery production and electroplating effluent ranges between 25-40^{o}C and 30-50^{o}C respectively (7,8).

Despite the relevance of temperature variation to NF operation, relatively few works have been devoted to understanding what performance-determining factors change with temperature and which of these changes have the greatest impact on NF permeate quality. Since the mobility factors are well-studied, NF studies usually make qualitative references to these to explain the effect of temperature on performance (9,10). Given the several membrane parameters significant for NF, the variations of these parameters with temperature and the resulting effect on salt removal and selectivity deserve attention. This thesis investigates this aspect of NF performance, the primary

question being: how does the net effect of membrane parameter change on NF permeate quality with temperature variation with that of the mobility factors. Chapter 2 and 3 study the variation of solute transport mechanisms with temperature, and the role of various parameters on permeate quality change with temperature respectively. Chapter 4 focuses on the change in monovalent-multivalent species selectivity with temperature, using an analytical framework to derive and explain general trends.

In chapter 5, the modeling capability for NF used in the previous parts of the thesis are extended to RO and forward osmosis (FO) to answer the question: can RO and FO be modeled as porous membranes? This question is motivated by the recent experimental evidence that free volume exists in these membranes and affect the species transport through the membrane (11,12). The pursuit of this question challenges conventional understanding held over several decades that RO and FO membranes are non-porous and species transport is purely diffusive (13–16). However, the work presented on this topic comes alongside others published in recent years that indicate either experimental evidence of pores or molecular dynamics describing species transport through free volume in RO and FO membranes. Finally, chapter 6 provides insight on the role of NF in improving energetic efficiency of seawater desalination plants. Results from this chapter show that NF allows the top brine temperature in Multi-Stage-Flash (MSF) distillation to increase from the conventional value of 120^{o}C to 160^{o}C, thereby increasing the energetic efficiency, measured by performance ratio (PR), by ∼41%.

2. Effect of Temperature on Solute Transport in Nanofiltration

2.1. Introduction

2.1.1. Significance of Nanofiltration for elevated feed temperatures

In a world where water-scarcity is a burgeoning issue, methods of water-treatment and reuse that are economic and minimize energy consumption are of vital importance for the safekeeping of the environment. Nanofiltration (NF) is a pressure driven membrane-based desalination technique. The pore sizes of NF membranes are between that of reverse osmosis (RO) and ultrafiltration (UF) membranes (17–20). NF has the unique capability to preferentially remove multivalent ions (1,21). In several applications, water temperature varies from point-to-point in the treatment plant or changes over time. For example, NF-MSF (nanofiltration with multistage flash) and NF-MSF-RO (nanofiltration with multistage flash and reverse osmosis), are widely studied applications of NF in hybrid with thermal desalination systems where feed (seawater or brackish water) temperature changes over the year and the performance of the nanofiltration membrane changes noticeably with temperature (22). Nanofiltration also has other high temperature applications: in the textile industry, water used for bleaching and dyeing may reach temperatures up to 90^{o}C; in the pulp and paper industry, the water temperature is often above 60^{o}C (10). Water temperature is usually reduced before membrane treatment. This practice requires expenditure on heat exchangers and also creates energy costs due to the inefficiencies of the heat exchangers (23). Thus, by designing NF membranes for optimal performance at above ambient temperature, capital costs and energy consumption in heat-exchangers, dependence on other energy-intensive water-treatment methods

such as RO, and the use of chemical additives to remove scale-forming ions can be reduced significantly (24). Detailed modeling of nanofiltration (NF) with variation in feed temperature is necessary to achieve this, as the rejection of undesired components can vary significantly as a result of changing temperature.

2.1.2. The DSPM-DE model of Nanofiltration

This work uses the Donnan Steric Pore Model with Dielectric Exclusion (DSPM-DE) to analyze the temperature dependence of nanofiltration. This model has been used widely into recent times to model and explain nanofiltration performance using a variety of feed solutions with success(25–28). DSPM-DE is a comprehensive model for nanofiltration. As the name suggests, the model provides information regarding the magnitudes of the different modes of solute exclusion occurring at the membrane-solution interfaces, namely steric exclusion (size-based exclusion at the pore opening), Donnan effect (repulsion or attraction effect due to membrane potential) and dielectric exclusion (resistance to the solute entering the membrane pores due to an energy barrier associated with shedding of the solute hydration shell in order to enter the pore) (3,29,30). The model uses the Nernst-Planck equation to describe solute transport through the membrane and hence provides information on the individual modes of transport within the membrane, namely diffusion (movement of solute down a concentration gradient), convection (solute transported by bulk fluid motion) and electro-migration (ion movement due to the membrane potential gradient). As inputs to this model, the membrane is characterized by certain structural parameters (pore radius and effective active layer thickness) and electrical parameters (membrane charge and pore dielectric constant) (3,31). These nanofiltration membrane properties are affected by experimental conditions such as feed composition, pH, concentration and temperature (32,33). An understanding of how membrane properties affect the modes of solute exclusion and solute transport for different

solutes is important in order to gain intuition about nanofiltration. Such understanding will ultimately allow one to gain intuition of how experimental conditions such as temperature affect rejection and solvent flux characteristics of nanofiltration membranes.

2.1.3. Conventional understanding of the effect of temperature on Nanofiltration

Usually, water flux through nanofiltration membranes increases with increase in temperature, while uncharged solute rejection reduces with increase in temperature and the variation of charged solute rejection with temperature depends on the ion and the membrane used. Although experimental evidence for these observations is abundant in literature, the understanding of how the membrane itself changes and related modeling work is missing in literature. For instance, from the study of Manttari et al.(10) on the nanofiltration of glucose and pulp mill effluent over a temperature range of 25^{o}C to 65^{o}C using several different membranes, the authors found that the rejection of uncharged solutes decreased by ~20% from 20^{o}C to 55^{o}C and the overall rejection of the ionic species remained almost unchanged (at ~90%) over the same range of temperature. Schaep et al.(9) experimentally studied the nanofiltration of ground water using the UTC-20 NF membrane over a temperature range of 10^{o}C to 30^{o}C and found that water flux at 30^{o}C is 1.5 times that at 10^{o}C. In their study, the rejection of monovalent ions (sodium, chloride and potassium) decreased significantly over the given range of temperature, while the rejection of divalent ions (calcium, magnesium and sulfate) was barely affected by temperature, showing only a slight increase with increase in temperature (9). In another study by Nilsson et al. (34), the Alfa Laval NFT-50 nanofiltration membrane was used over a temperature range of 20^{o}C-50^{o}C keeping solvent flux constant, and the results showed that the rejection ratio of potassium-chloride decreased less noticeably than that of glucose. While Schaep et al. (9) interpret the observed changes in ion

passage with temperature based on the increase in solute diffusivity with temperature, Nilsson et al. (34) justify their observations based on membrane charge effects.

Although there is abundant literature on nanofiltration of charged solutes at different temperatures, to the best of the authors' knowledge, none of them attempt to fit parameters as a function of temperature with respect to the DSPM-DE model, taking into consideration change in membrane charge and pore dielectric constant. Nilsson et al. (34)mention that there is no significant change in the isoelectric point of the Alfa Laval NFT-50 membrane with variation of temperature, hence indicating that the membrane charge properties are not greatly affected by temperature. However, it is unclear whether this is a general trend for all membranes without the relevant data from other membranes. Furthermore, as seen in the work of Schaep et al. (9), the rejection ratio of certain ions shows dramatic change with temperature, and it is questionable whether that is simply a result of a change in ion diffusivity as a function of temperature, as mentioned by the authors, or of changes in membrane charge and pore dielectric constant also.

Knowledge of the extent to which each of the quantities (solvent viscosity, solute diffusivity, membrane structural and electrical parameters) are affected by temperature and the resulting effect they have on ion passage would allow one to explain the experimental results with certainty. The work of Amar et al. (22) concludes that it is not sufficient to consider only the change in solvent viscosity and solute diffusivity in order to explain the increased water flux and reduced rejection of uncharged solutes with increase in temperature and that the change in membrane structural parameters with temperature are essential to correctly explain how nanofiltration of uncharged solutes is affected by temperature. However, their work is restricted by its applicability to only uncharged solutes.

2.1.4. Aims of this study

In this work, the effect of temperature on nanofiltration membrane properties and the resulting effect on ion and solvent transport through the membrane are studied, using three different feed compositions. The DSPM-DE model is used to model nanofiltration of charged solutes at different temperatures. The objective is to not only observe the resulting change in membrane performance but to gain intuition on how ions of different valence, size and diffusivity are affected differently by temperature.

2.2. Governing Equations

2.2.1. Historical development of the DSPM-DE model

As mentioned earlier, the model used for this study is the Donnan Steric Pore Model with dielectric exclusion (DSPM-DE). Despite its complexity, the model's thoroughness has made it become widely used for modeling nanofiltration, and it has been used successfully in the literature to model experimental membrane performance (3,31,33). This model evolved from the hindered transport theory of uncharged solutes in pores introduced by Anderson et al. in 1974 (35,36), which was later extended for ionic species by including the electrochemical potential gradient in the solute transport equation, leading to electrokinetic models that use the extended Nernst-Planck equation (e.g. the Space-charge model and TMS models) (37,38). One such model was the DSPM (Donnan-Steric Pore Model) introduced by Bowen et al. (39) in the late 1990s and it was the precursor of the DSPM-DE model. The DSPM considered only the steric and Donnan exclusion mechanisms. This model quickly became popular and was successful in modeling nanofiltration of a wide variety of solutions, even those consisting of multivalent co-ions (ions with the same charge as the membrane) (29,30). However, its major drawback was in its failure to model

experiments with multivalent counter-ions. This failure was attributed to the deficiency of the exclusion mechanisms considered. The DSPM-DE model includes an additional exclusion mechanism, known as dielectric exclusion which allowed researchers to overcome the difficulties in modeling multivalent counter-ions (29).

However, the concept of dielectric exclusion and the mechanism by which it works has been widely debated over the years. Some authors suggest that the Donnan exclusion mechanism is sufficient to explain rejection of ions, including counter-ions. For example, Higa et al. (40) showed that a solution with Ca^{2+}, K^{+} and Cl^{-} ions passing through a negatively charged membrane can be modeled successfully by considering only Donnan exclusion. Other authors have found Donnan exclusion to be insufficient in modeling nanofiltration, as mentioned previously while discussing the transition of the DSPM to DSPM-DE. Evidence from molecular dynamics simulation of membranes with nanopores, however, describes dielectric exclusion as an undeniable phenomenon (41,42). Yaroshchuk et al. (43) further mention that the dielectric exclusion is a 'universal phenomenon' and should be considered alongside steric and Donnan exclusion. Bandini et al. (30) mention two mechanisms for dielectric exclusion by nanofiltration membranes: image forces and the Born effect. However according to Bowen et al. (3), in nanofiltration, the Born effect of dielectric exclusion is more dominant than the effect of image charges that develop at the interface of the membrane and bulk solution. This is because the small pores in nanofiltration membranes cause the intra-pore dielectric constant of the solvent to be almost equal to that of the membrane material itself. Furthermore, the image charges are screened by electric double layers in electrolyte solutions(3). The DSPM-DE model in the form introduced by Bowen and Welfoot (3) has been used successfully by several authors, including in recent years for a variety of feed compositions (27,28,44). In reference (3), Bowen and Welfoot successfully implemented the DSPM-DE model

for the same membrane considered in the current work (Desal5DK) accounting for only the Born mechanism of dielectric exclusion for sodium-chloride and magnesium-chloride. In their study, they also showed experimental results over the same range of feed concentration considered in the current work, which justifies the use of this model for the simulations here.

In the current work the DSPM-DE model equations are implemented using MATLAB vR2015b following the approach by Geraldes et al. (29), in which only the Born effect on dielectric exclusion is incorporated (as per the formulation in (3)). This effect is described in detail in section 2.4.4. The DSPM-DE model in this form has been well validated with lab-scale experiments (29,33). In this model, the membrane is characterized by structural parameters (effective pore radius and active layer thickness) and electrical parameters (membrane charge and pore dielectric constant). The inclusion of the dielectric exclusion mechanism in addition to Donnan exclusion and steric exclusion for the current study allows the work to be broad and include all important effects determining solute transport through a nanofiltration membrane with temperature change.

2.2.2. Governing equation for solute flux

The solute flux through the membrane is governed by the Extended Nernst-Planck equation (ENP). For each solute *'i'*, the ENP equation is given by Eq. (2-1) (25) .

$$J_{i,pore} = -D_{i,pore}\frac{dC_{i,pore}}{dx} - \frac{z_i C_{i,pore} D_{i,pore}}{RT} F \frac{d\psi}{dx} + K_{i,c} C_{i,pore} J_w \qquad (2\text{-}1)$$

where $J_{i,pore}$ is the solute flux of the species 'i', consisting of the diffusive, electromigrative and convective terms respectively, in the order they appear in the equation. $D_{i,pore}$, $C_{i,pore}$ and z_i are the intra-pore diffusion coefficient, concentration and valence respectively of species i , $J_w$is the water flux through the membrane, ψ is the membrane potential. Due to the extremely small pore sizes in nanofiltration membranes, the 'hindered transport theory' is used and thus the terms of the

ENP are modified by hindrance factors $K_{i,c}$ (for the convective term) and $K_{i,d}$ (that multiplies the bulk diffusivity) to give the diffusivity in the pore, as found in the diffusive and electromigrative terms. Thus $D_{i,pore} = K_{i,d} D_{i,\infty}$. Both these factors are functions of the ratio of the solute radius to pore radius, λ_i (25). The model treats the pores as perfectly cylindrical and the solutes as perfect hard spheres. Figure 2-1 schematically describes each of the modes of solute transport considered in the Extended Nernst-Planck equation. The diffusive term exists due to the concentration gradient of each species within the membrane, while the convective term is the transport of the solute as a result of 'being carried' by the solvent through membrane pores. The electromigrative term is a result of the gradient of membrane potential through the membrane. The membrane potential is an electrostatic potential that develops to balance ionic fluxes and maintain quasi-electroneutrality within the membrane (29).

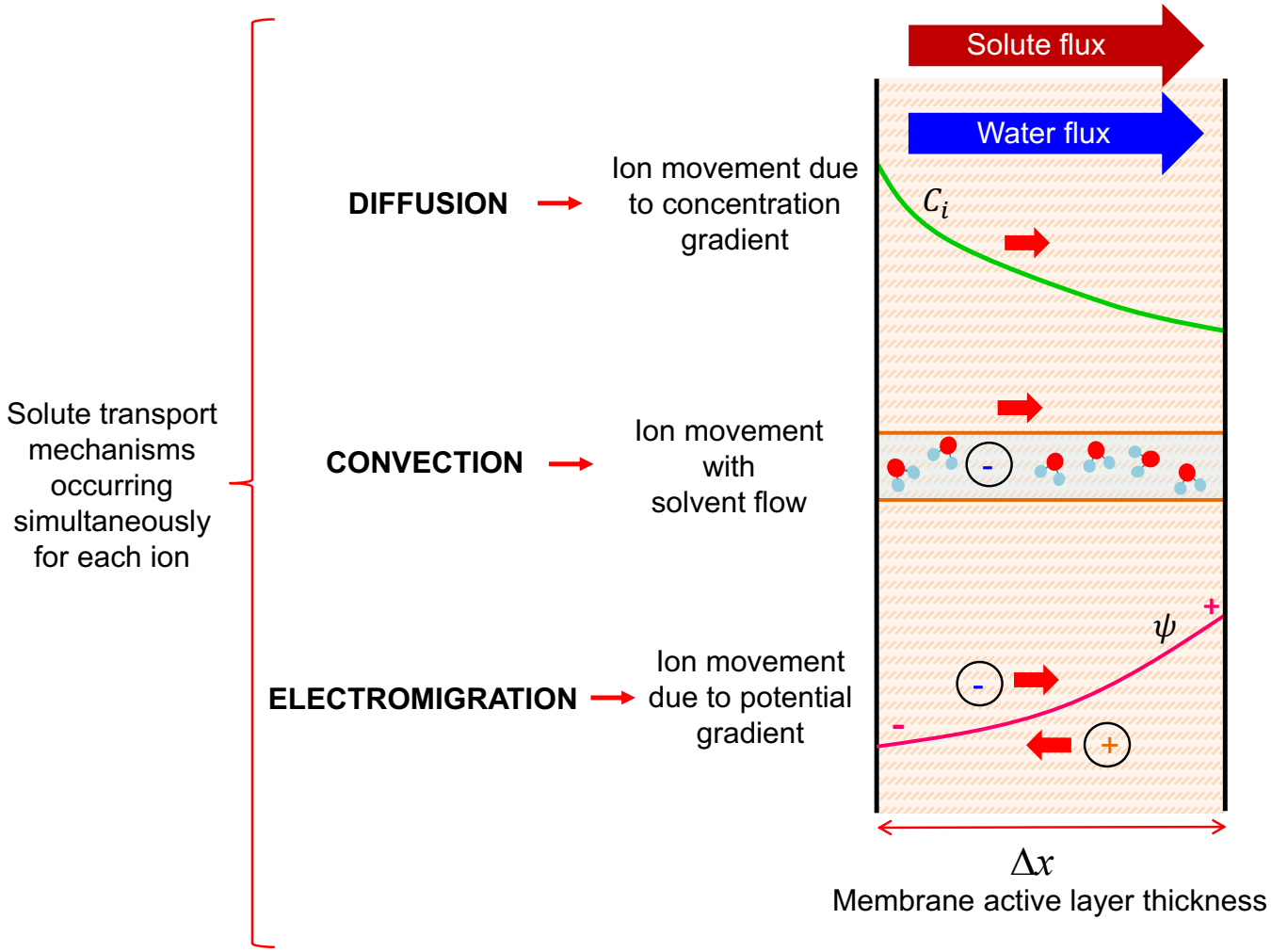

Figure 2-1. Schematic representation of solute transport mechanisms in the current model described by the Extended Nernst-Planck (ENP) equation, which is a component of the Donnan Steric Pore model with Dielectric Exclusion (DSPM-DE).

2.2.3. Equilibrium boundary conditions on membrane-solution interfaces due to solute exclusion mechanisms

At the membrane-feed solution interface, the equilibrium boundary condition is established due to the combination of the three exclusion mechanisms considered in the DSPM-DE model: the steric exclusion, dielectric exclusion (due to the Born effect, which accounts for the solvation energy

barrier for the ion to enter the pore, cf. section 2.4.4.) and Donnan exclusion. These mechanisms are represented schematically in Fig. 2-2.

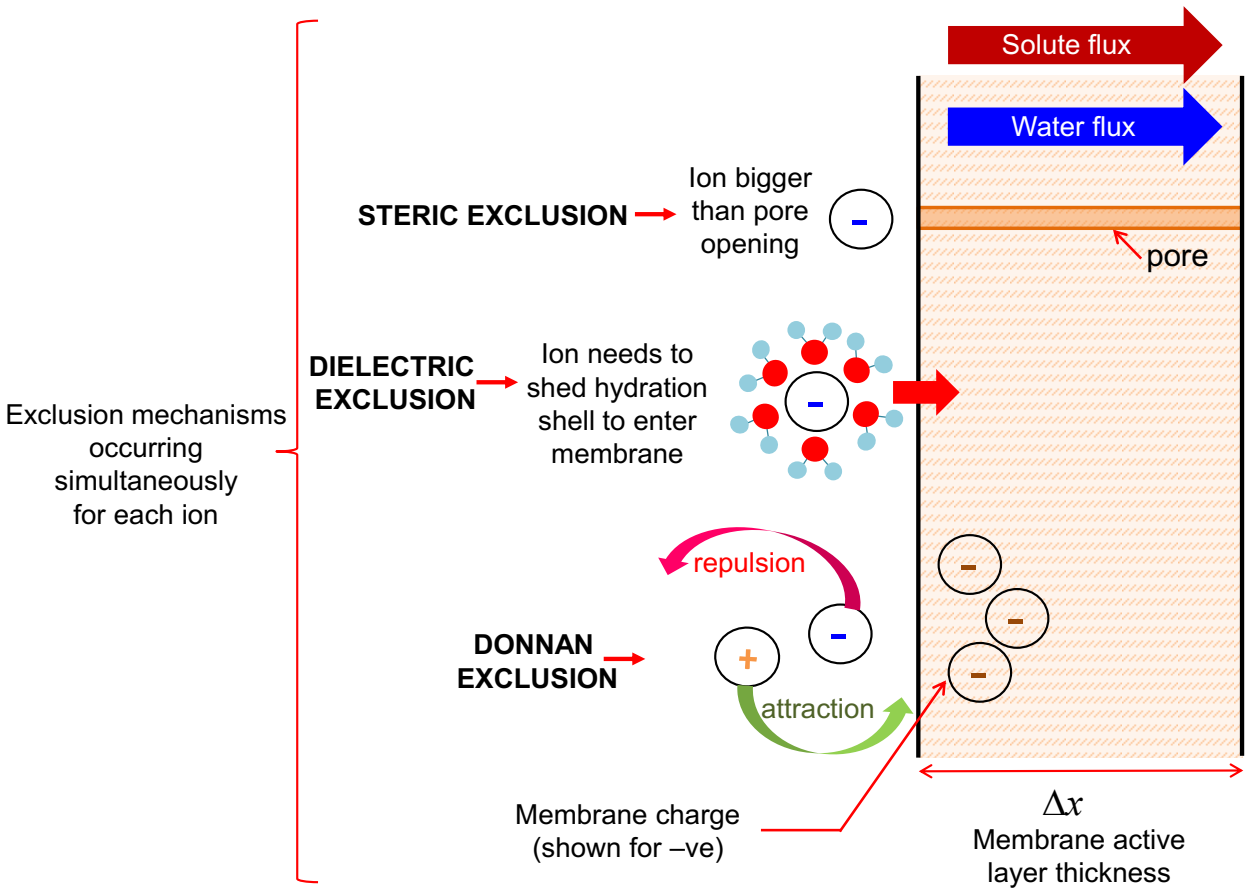

Figure 2-2. Schematic representation of solute exclusion mechanisms in nanofiltration as per the Donnan Steric Pore Model with Dielectric Exclusion (DSPM-DE).

Mathematically, these effects are described by Eq. 2-2:

$$\frac{\gamma_{i,pore}C_{i,pore}}{\gamma_{i,m}C_{i,m}} = \Phi_i \Phi_B \, exp\left(-\frac{z_i F}{RT}\psi_{D,m}\right)\Big|_{in} \qquad (2\text{-}2)$$

where $C_{i,pore}$ is the solute concentration just within the pore 'entrance'; $C_{i,m}$is the feed concentration at the membrane-feed solution interface; and $\gamma_{i,m}$, $\gamma_{i,pore}$, are solute i's activity

coefficients at the membrane-feed solution interface and just within the pore entrance respectively (calculated by the Davies equation). Φ_i,$\Phi_B$are the steric partitioning factor and Born solvation partitioning factor, respectively, which represent the extent of exclusion experienced by the ion due to these effects. These two partitioning factors are numbers smaller than unity such that a smaller value indicates higher exclusion. The effect of the partitioning factors is evident from the left hand side of Eq. 2-3, which indicates that a smaller value of Φ_i or Φ_B causes a reduction of the ratio between solute concentration within the membrane pore ($C_{i,pore}$) to the concentration immediately outside the membrane ($C_{i,m}$, due to concentration polarization). The term $\psi_{D,m}$ is the Donnan potential on the feed side, defined as the potential difference between the point just within the pore entrance and the solution (at the feed-membrane interface). The expressions for the steric partitioning factor, the Born solvation partitioning factor and the two hindrance factors are given in (Roy, Sharqawy, & Lienhard, 2015) and used in the present model.

Similarly, the boundary condition on the permeate side (i.e. at the membrane-permeate interface) is given by:

$$\frac{\gamma_{i,pore}C_{i,pore}}{\gamma_{i,p}C_{i,p}} = \Phi_i\Phi_{\mathrm{B}}\, exp\left(-\frac{z_iF}{RT}\psi_{D,p}\right)\Big|_{out} \tag{2-3}$$

where $C_{i,pore}$is now the concentration at the pore exit (just within the membrane) and $C_{i,p}$ is the permeate concentration, just outside the membrane; $\psi_{D,p}$ is the Donnan potential difference between these two points.

Equations (2-2) and (2-3) state that the ratio of concentrations just within the membrane and that at the membrane-feed/permeate solution is governed by the steric, dielectric and Donnan

exclusion effects. Figure 2-2 schematically explains each of the exclusion mechanisms considered in the DSPM-DE model.

2.2.4. Electroneutrality conditions

Within each domain considered in the model, i.e. the bulk feed solution, the concentration polarization boundary layer (membrane-feed interface), the membrane, and the permeate solution, there can be no net charge (the electroneutrality condition). Within the membrane, the electroneutrality condition is described as:

$$\sum_{i=1}^{N_c} z_i C_{i,pore} = -C_X \tag{2-4}$$

where N_c is the number of species/components in the mixture, z_i is the valence of the species i and $C_X$is the volumetric charge density of the membrane. Similar electroneutrality equations can be written for the bulk feed, membrane-feed interface and permeate by using the relevant concentration and setting the volumetric charge density to zero, since no net charge is present at any point outside the membrane.

2.2.5. Solvent flux

As described by Bowen et al. (3) and Wang et al. (37), the flow of water through the membrane has been successfully modeled by a creeping laminar flow in the form of the Hagen-Poiseuille equation. Therefore, the transmembrane solvent flux $J_w$as a function of membrane structural parameters and net driving pressure is given by:

$$J_w = \Delta P_{net}\left(\frac{r_{pore}^2}{8\nu\rho_w\left(\frac{\Delta x}{A_k}\right)}\right) \tag{2-5}$$

where r_{pore} is the membrane pore radius and $\Delta x/A_k$ is the effective active layer thickness, taking into account membrane porosity A_k. The fluid properties used in the expression are ν, the kinematic viscosity of the solvent and ρ_w, the density of the solvent. ΔP_{net} is the net pressure across the membrane, which is the hydraulic pressure applied, minus the osmotic pressure difference across the membrane.

Figure 2-3 illustrates how the exclusion mechanisms come together to influence the concentration profile across the membrane. A nanofiltration membrane with either positive or negative membrane volumetric charge density is shown. The feed side is pressurized so that water flux and solute flux both go from the feed to the permeate side. Cross-flow velocity over the membrane is assumed to be high enough so that no concentration polarization occurs. Concentration jumps from the feed value to that within the membrane on the feed side due to the feed side partitioning effect (cf. Eq. 2-2). A similar effect is seen on the permeate side (cf. Eq. 2-3). The partitioning results from a combination of the steric, dielectric and Donnan exclusion effects, as mentioned earlier. The ion with charge opposite to that of the membrane (membrane counter-ion) is in greater abundance inside the membrane, as shown by the green concentration profile, whereas the membrane co-ion is less abundant and is represented by the blue concentration profile. The concentration profiles shown in this diagram represent only the simple case of a binary 1:1 salt, i.e. a salt with one cation and one anion of equal and opposite valence. Thus, in order to maintain electroneutrality, the concentrations of both ions at any point outside the membrane have to be equal to each other whereas within the membrane, the electroneutrality condition is satisfied by

including the membrane charge density (cf. Eq. 2-4), thereby resulting in membrane counter-ion concentration to be larger than that of the co-ion inside the membrane. In most cases described subsequently, the rejection ratio is positive and the permeate concentration is less than that of the feed side.

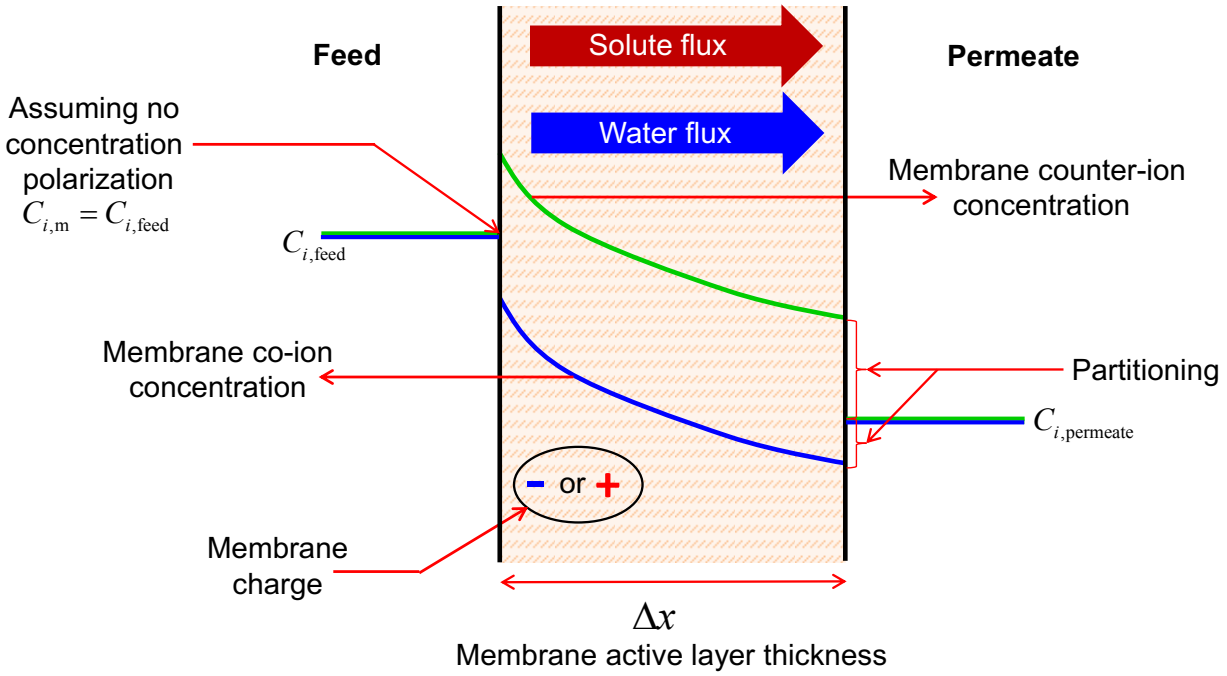

Figure 2-3. Concentration profiles of ions from a binary 1:1 salt through the membrane thickness in a nanofiltration membrane

2.3. Validation

In this study, the membrane structural parameter values at different temperatures are taken from experimental work by Amar et al. (Amar, Saidani, Deratani, & Palmeri, 2007) (cf. Appendix A). Those authors fit membrane pore radius and effective active layer thickness of the Desal5DK membrane at different temperatures using the hindered transport theory, assuming the solute

particles are hard spheres travelling through cylindrical pores. They obtain the effective pore size for the membrane at each temperature by taking the average fitted value from a number of uncharged solutes at those temperatures in the limit of high Péclet number where the rejection versus solvent flux plot plateaus. They provide the effective membrane thickness individually for each solute. Their work assumes that no concentration polarization occurs in the system. As mentioned previously, the model used for the present study is also based on the hindered transport theory, and so the fitting parameters obtained by Amar et al. (22) are expected to work well in the present work.

Figure 2-4 shows the experimental data from Amar et al. (22) along with results from the current model for arabinose, at the three temperatures to be considered in this study, 22^{o}C, 40^{o}C and 50^{o}C. In the model used for this work, equations 2-1 to 2-3 described above are discretized as shown in (29) and solved numerically using MATLAB (version R2015b). The difference between the experimental data and the modeling results are below 5% in most cases, except for the two data points at the lowest values of solvent flux at 40^{o}C and 50^{o}C. This is, however, in accordance to the modeling by Amar et al. (22)as can be seen in Fig. 12 in their paper, which shows the comparison between experimental data and their modeling when changes in all four modeling components required for uncharged solutes (two membrane structural parameters, solvent viscosity and solute diffusivity) with temperature are taken into account. The better agreement between modeling and experiment at higher values of water flux (and correspondingly higher Péclet number) both in the work of Amar et al. (22)and in this work is not surprising given that the fitting was done in the range of high Péclet number, as mentioned earlier. It is common practice to use membrane structural parameters obtained from fitting with respect to uncharged solute data for modeling

solutions containing charged solutes. Membrane charge and pore dielectric constant are then fitted in order to model nanofiltration of charged solutes accurately (33).

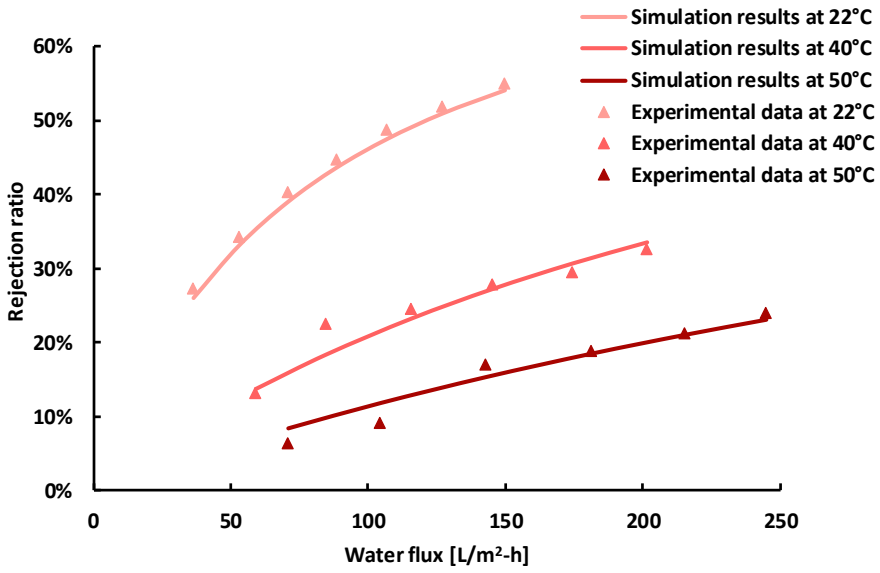

Figure 2-4. Validation of current DSPM-DE modeling with experimental NF data of Amar et al. (Amar, Saidani, Deratani, & Palmeri, 2007)

The objective of this paper is to explain the changes in ion transport through the Desal5DK membrane at different temperatures by taking into account the temperature dependence of all four membrane parameters as well as the change in solvent viscosity and solute diffusivity. Since the exact change of membrane charge for the Desal5DK membrane with respect to temperature is not currently known, a parametric study will be done with respect to this quantity, hence providing insight into a wide range of possible cases. An analytical expression for the pore dielectric constant, described in detail in a later section, will be used to estimate this quantity as a function of temperature.

2.4. Results and Discussion

In this section, solute transport mechanisms for sodium-chloride, magnesium-chloride and seawater ions at different temperatures are analyzed. Results are presented and discussed for 3 temperatures (22°C, 40°C and 50°C) for conciseness and simplicity. In the supplementary information section, results for 30°C in addition to the 3 temperatures described here are presented to show that the trends with temperature described in the current paper hold through the entire temperature range from 22-50°C.

2.4.1. Property variation at higher temperature

The principal new methodology applied in this work is the use of the DSPM-DE to conditions with increasing temperature. At higher temperature, numerous input variables for the model change. A summary of these parameters is given in table 1. To the best of the current authors' knowledge, this work is the first to consider the variation of these properties to the DPM-DE model for NF. The membrane structural parameters (r_{pore} and $\Delta x/A_k$) vary with temperature due to the restructuring of the polymer material. The variation of the pore dielectric constant with temperature is described further in section 2.4.4.1. and is due to the combined effect of membrane pore size variation and variation of solvent dielectric constant with temperature.

Table 2-1. Input variables to the DSPM-DE model that vary by temperature

Symbol	Variable	Units	Source	Change at higher temperature
ν	Solvent kinematic viscosity	$m^2\ s^{-1}$	Ref (Huber, et al., 2009)	Decreases
r_{pore}	Pore radius	m	(Amar, Saidani, Deratani, &	Increases

			Palmeri, 2007), Table 4	
$\Delta x/A_k$	Effective membrane thickness (for both solute and water)	m	(Amar, Saidani, Deratani, & Palmeri, 2007), Table 4,	Varies
D_i	Solute Diffusivity	$m^2\ s^{-1}$	Fig 17. Stokes-Einstein Eq., (Nilsson, Tragardh, & Ostergren, 2008)	Increases
ε_{pore}	Pore dielectric constant	-	Eq. 2-9	Increases

2.4.2. Sodium-chloride (NaCl) transport as a function of temperature

In this section, the transport of sodium and chloride ions through the membrane is analyzed at different temperatures. Sodium-chloride is the dominant salt by mass in most waters considered for desalination, and often a desirable property of NF membranes is sodium-chloride passage with exclusion of other salts that have scaling potential. The effect of temperature is captured in the change of the structural parameters of the membrane as obtained from Amar et al. (22)as well as the change in ion diffusivity and solvent viscosity. In addition, the effect of membrane charge on the ion transport and rejection is observed. A subsequent section will discuss the effect of dielectric exclusion in detail. In addition to the net solute transport, the convective, diffusive and

electromigrative fluxes are also observed individually. Since correlations for membrane parameter variation (both structural and electrical) with temperature are not available in literature, the simulation results are shown here at just the few temperatures for which structural parameters are given by Amar et al. (22). The range of temperature studied by Amar et al. (22) (22-50^{o}C) is practically relevant because the lower limit represents the temperature at which several lab-scale experiments are conducted ((3,33)) and at which membrane specifications from the manufacturer are provided. The upper limit of 50^{o}C is slightly lower than the upper limit of the temperature tolerance of the experimental setup used in reference (22) and represents the typical temperature of geothermal brackish water which is often used as NF feed(22).

For the results that follow, the feed concentration of sodium-chloride is 0.01 M for all cases. Concentration polarization is neglected, assuming a high cross-flow over the membrane with associated high mass transfer coefficients. Although concentration polarization may not be negligible in some common industrial applications, small lab setups can reach this condition. This approach allows us to ignore the flow properties on either side of the membrane in developing the results for membrane performance.

2.4.2.1. Net solute transport change with temperature

The model shows that the solvent transport and net solute transport always increase as temperature is increased. As a result, the rejection ratio always decreases with increasing temperature as seen in Fig. 2-5a. Furthermore, it is seen that each of the convective, diffusive and electromigrative contributions to solute flux increase in absolute value with temperature as well. These effects occur as a result of the change in membrane structural parameters, solvent viscosity and solute diffusivity due to temperature at each value of membrane charge.

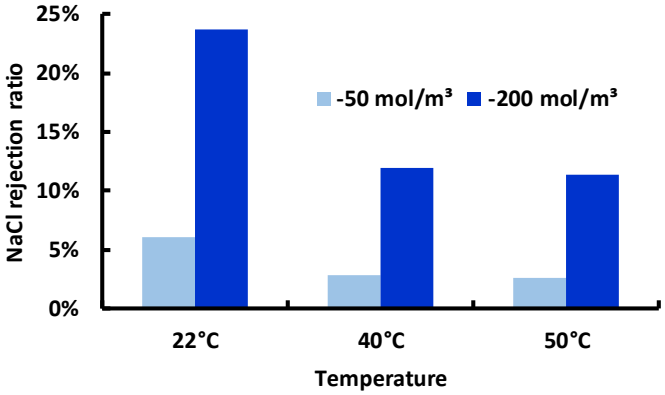

Fig. 2-5a. NaCl rejection ratio vs. T

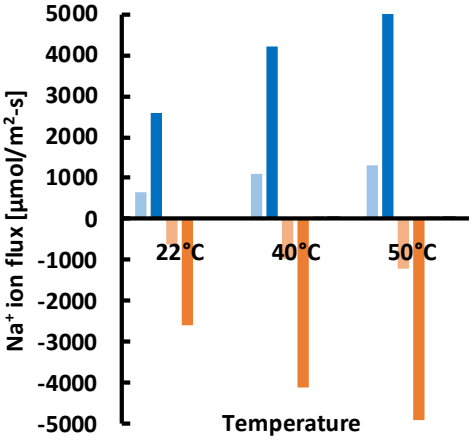

Fig. 2-5b. Na^+ flux vs. T

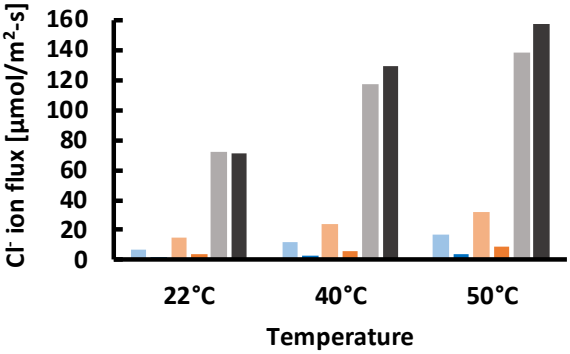

Fig. 2-5c. Cl^- flux vs. T

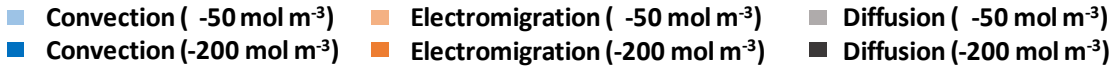

Figure 2-5. For a negatively charged NF membrane (−50 or −200 mol m^{-3}), modeling results for rejection and solute transport of Na^+ and Cl^- ions in a 0.01M NaCl solution at different temperatures: (a) rejection of NaCl; (b) transport of Na^+ ions by the three modes; and (c) transport of Cl^- ions by the three modes.

2.4.2.2. Change in solution and membrane properties with temperature

Some of the temperature-dependent properties mentioned in section 2.4.1. were more dominant in influencing solute flux (and hence rejection) and solvent flux through the membrane with temperature variation than others. As temperature increased, changes in the membrane structural

parameters (i.e., pore radius and membrane thickness) together had a much more prominent influence on membrane performance than the solvent and solute mobilities combined. The effects of these two sets of parameters can be separated by running the simulation in two steps. At first, all effects are considered to vary with temperature together. Subsequently, the effect of increased solute and solvent mobilities are isolated by running a simulation in which membrane parameters are kept constant. For example, from the fitting of Amar et al. (22) it is seen that going from 22°C to 40°C, the pore radius increased by 1.72% while the membrane thickness decreased by 53% with respect to solute transport and ~4% with respect to water transport (cf. Fig 17 in reference(22)). Over this temperature range, the diffusivities of the sodium and chloride ions increased by ~55% each while the solvent viscosity reduced by ~30%. In the simulation, when variation of pore radius and membrane thickness are accounted for in addition to that of the solvent and ion mobilities, the decrease in rejection of sodium-chloride going from 22°C to 40°C is ~50% (cf. Fig. 2-5). On the other hand, in the simulation, in order to isolate the effect of solvent and ion mobilities, if the membrane structural parameters are kept constant at the values corresponding to 22°C, and only solvent viscosity and ion diffusivity are varied corresponding to the temperature increase from 22°C to 40°C, the ion rejection reduces by only ~5%. Figure 2-5 shows that the change in membrane volumetric charge value from −200mol/m^3 to −50 mol/m^3 (decrease by 75%), when all other parameters (pore radius, effective thickness, solvent viscosity and ion diffusivity) are kept constant corresponding to values at 22°C, the membrane volumetric charge density by itself reduces the rejection ratio by almost four fold. These numbers clearly illustrate that the variation of the membrane parameters causes a larger percentage change in rejection ratio (and hence ion transport) than the solvent viscosity and the ion diffusivity combined.

2.4.2.3. Change in the three modes of solute transport: convection, diffusion and electromigration with temperature

When temperature increases, the higher solvent flux carries greater amount of solute with it, causing the increased solute convection (cf. Fig. 2-5). The overall term $K_{i,c}C_{i,pore}J_w$ is therefore larger for each solute at higher temperatures. Furthermore, at higher temperature, the increase in solute diffusivity causes the diffusive transport to increase. Regarding diffusive transport, a reduction in rejection ratio due to the increase in temperature implies that the concentration gradient across the membrane is also reduced since there is a smaller fall of concentration across the membrane, thereby causing the $\frac{dC_{i,pore}}{dx}$ term in the Nernst-Planck equation to be reduced in steady state. However, the increase in solute diffusivity due to increase in temperature over-compensates for this effect and overall, the diffusive term $-D_{i\ pore}\frac{dC_{i,pore}}{dx}$ is greater in magnitude at higher temperature. Similar to the concentration gradient, the potential gradient across the membrane is smaller in magnitude at higher temperature. However, the electromigrative flux increases at higher temperature predominantly due to the effect of increased solute diffusivity.

2.4.2.4. Effect of membrane charge on chloride ion transport

From Fig. 2-5c, showing the magnitudes of the different modes of transport of the chloride ion within the membrane at various negative values of membrane charge, we see that the diffusion is the dominant mode of transport and it becomes larger at larger magnitudes of membrane charge. This is because the negative chloride ion is repelled by the negatively charged membrane and so its concentration within the membrane $C_{Cl^-,pore}$ is small, leading the convective and electromigrative fluxes to be small, and they reduce further at a greater magnitude of negative membrane charge. The chloride ion must have equal solute transport through the membrane as the

sodium ion, however, in order to maintain electroneutrality and so the reduced convective and electromigrative fluxes are compensated for by the diffusive flux, which therefore becomes the dominant mode of transport for the chloride ion. At greater magnitudes of negative membrane charge, the intra-membrane concentration for the chloride ion reduces further and hence diffusion becomes increasingly dominant (Fig. 2-5c). Along a similar line of reasoning, for positive values of membrane charge (Fig. 2-6), the chloride ions are attracted into the membrane, causing its intra-membrane concentration to be large compared to that within negatively charged membranes. Thus, in membranes with a positive charge, chloride transport is predominantly convective and electromigrative (Fig. 2-6c). For a positively charged membrane (Fig. 2-6), the membrane potential is positive and decreases in magnitude across the membrane from feed to permeate side. The electromigration of the negatively charged chloride ions is in the direction towards the more positive membrane potential (from permeate to feed side), opposite to the overall solute transport. The solute transport and rejection of sodium and chloride ions when the membrane is positively charged is given in Fig. 2-6.

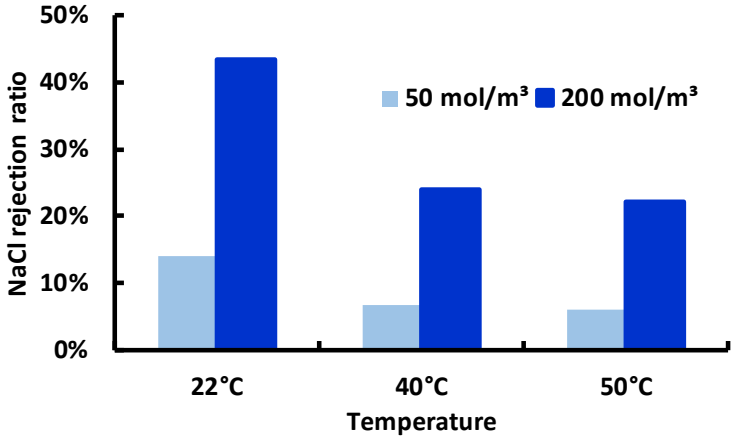

Fig. 2-6a. NaCl rejection ratio vs. T

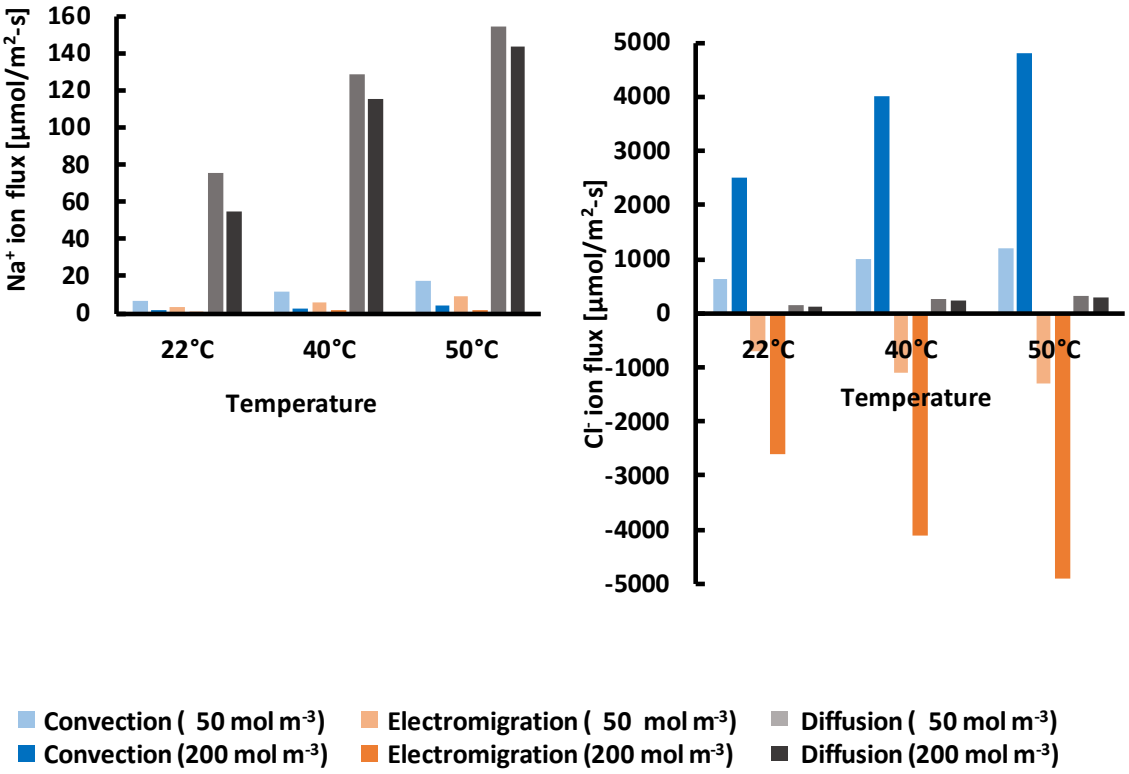

Fig. 2-6b. Na^+ flux vs. T **Fig. 2-6c. Cl^- flux vs. T**

Figure 2-6. For a positively charged NF membrane (50 or 200 mol m^{-3}), modeling results for rejection and solute transport of Na^+ and Cl^- ions in a 0.01 M NaCl solution at different temperatures: (a) rejection of NaCl; (b) transport of Na^+ ions by the three modes; and (c) transport of Cl^- ions by the three modes.

2.4.2.5. Sodium ion transport

For sodium ions, for each value of membrane charge at each temperature, the convective flux is always greater in magnitude than the electromigrative i.e. opposite to the behavior of chloride ions flux (Fig. 2-5 and Fig. 2-6). The reason is that the ratio of convective to electromigrative flux $R_{i,C/E}$ is greater for sodium than for chloride, where $R_{i,C/E}$ is defined as:

$$R_{i,\,C/E} = \frac{Convection_i}{Electromigration_i} = \frac{K_{i,c} J_w \Delta x R T}{z_i D_{i,pore} \Delta \psi F} \qquad (2\text{-}6)$$

where $\Delta\psi$ is the potential drop across the section of the membrane under consideration (or the entire thickness of the membrane if the potential profile is linear) and is equal for all ions in the system. Thus the ratio of magnitudes of $R_{Cl^-,\,C/E}$ to $R_{Na^+,\,C/E}$ is given by:

$$\frac{\left|R_{Cl^-,\,C/E}\right|}{\left|R_{Na^+,\,C/E}\right|} = \frac{K_{Cl^-,c}\, D_{Na^+,pore}}{K_{Na^+,c}\, D_{Cl^-,pore}} \tag{2-7}$$

This ratio is less than unity, and therefore convection is dominant over electromigration for sodium ions while it is the opposite for chloride ions.

2.4.2.6. Summary and implications of NaCl transport at higher temperature

1. Solvent and net solute transport increase with increase in temperature.
2. All of the individual modes of solute transport, i.e. convection, diffusion and electromigration, increase in magnitude with temperature.
3. The cumulative effect of changes in membrane properties with temperature is more dominant in influencing solute transport than the combined effect of the corresponding changes in solvent viscosity and ion diffusivity with temperature.
4. The convective mode of solute transport increases in magnitude with temperature predominantly due to the increase in solvent transport. The diffusive and electromigrative modes of transport increase in magnitude with temperature predominantly due to increase in solute diffusivity with temperature.

5. In negatively charged membranes, anion transport is predominantly diffusive while cation transport is predominantly convective. The situation is reversed for positively charged membranes.

2.4.3. Magnesium-chloride ($MgCl_2$) transport as a function of temperature

This section considers magnesium-chloride, following a similar path to that for sodium-chloride in the previous section. Mg^{2+} rejection is desirable for scale control in common thermal desalination processes, and in several aspects, Mg^{2+} rejection is representative of other divalent ions. However, from the current section and from section 2.4.5., it is clear that rejection of this ion is highly dependent on the feed composition. In this study, the concentration of magnesium-chloride salt is taken as 5 mol/m^3 (0.005 M) so that the feed solution contains 10 mol/m^3 (0.01 M) of chloride ions. Thus the concentration of chloride ions in the study of sodium-chloride and magnesium-chloride are equal.

2.4.3.1. Change in solution and membrane properties with temperature

As mentioned in section 2.4.2., simulation results are provided only at temperatures for which Amar et al. (22) provide structural parameter values. Again, similar to the case of sodium-chloride, in going from 22^{o}C to 40^{o}C, the diffusivities of both ions increased by ~55%, and the fitting parameters of Amar et al. show an increase of pore radius by 1.72% and decrease in membrane thickness by ~53% with respect to solute transport and ~4% with respect to water transport . The simulations show that the combined effect of the change of solvent viscosity and ion diffusivity play a relatively small role in explaining the change in ion rejection (and hence transport) for the

given change in temperature compared to the combined effect of the membrane structural parameters. Similar to the approach in section 2.4.2., the effects of these two sets of parameters (solute and solvent mobilities versus membrane structural parameters) can be separated by running the simulation in two stages. At first, all effects are varied with temperature together and subsequently another simulation is done in which membrane parameters are kept constant. To that end, in the simulation, if the pore radius and membrane thickness are kept at values corresponding to 22°C and only the solvent viscosity and ion diffusivity values are changed to those at 40°C, the ion rejection increases by 5.3% and 0.1% respectively for a membrane charge of -50 mol/m^3 and 50 mol/m^3, going from 22°C to 40°C. However, when all parameters in the simulation (pore radius, effective thickness, solvent viscosity and ion diffusivity) are allowed to change to values corresponding to 40°C, the rejection ratio of the ions decreases by ~60% and 3% for these cases. The effect of reducing the negative value of membrane charge from −200 mol/m^3 to −50 mol/m^3 independently at 22°C reduces the rejection ratio by 129%.

2.4.3.2. Comparison of $MgCl_2$ and NaCl transport in negative and positively charged membranes

The larger charge on multivalent ions, and in most cases, their larger Stokes radii and lower diffusivities compared to monovalent ions cause significant differences in the rejection performance by NF. This aspect is of crucial importance for membrane design at higher temperatures, as in many cases, such as seawater desalination, it is desirable to reject mainly the divalent ions. Solute transport by the different modes and rejection ratio for the Mg^{2+} and Cl^- ions at different temperatures for membranes with negative and positive charges are shown in Fig. 2-7 and Fig. 2-8 respectively.

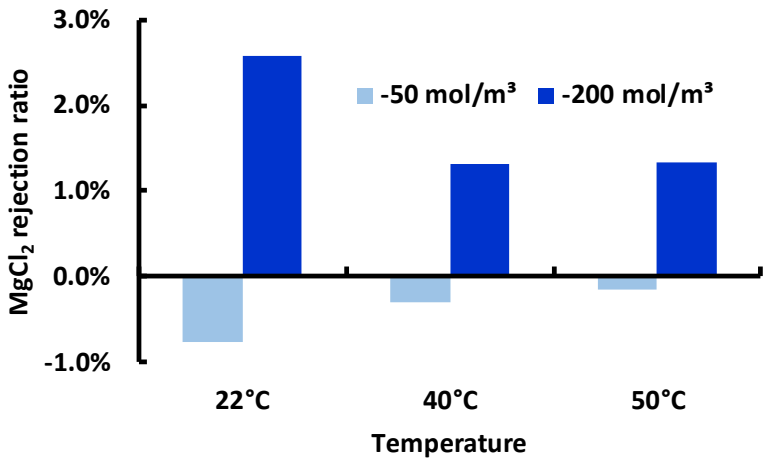

Fig. 2-7a. $MgCl_2$ rejection ratio flux vs. T

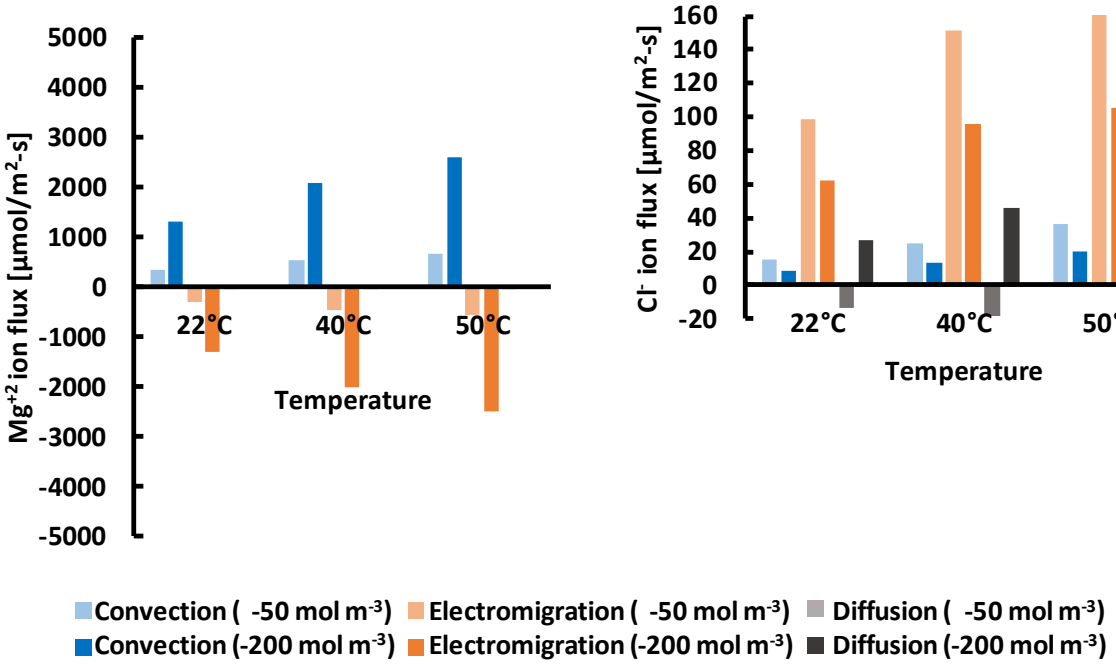

Fig. 2-7b. Mg^{2+} flux vs. T **Fig. 2-7c. Cl^- flux vs. T**

Figure 2-7. For a negatively charged NF membrane (−50 or −200 mol m^{-3}), modeling results of rejection and solute transport of Mg^{2+} and Cl^- ions in a 0.005M $MgCl_2$ solution at different temperatures: (a) rejection of $MgCl_2$; (b) transport of Mg^{2+} ions by the three modes; and (c) transport of Cl^- ions by the three modes.

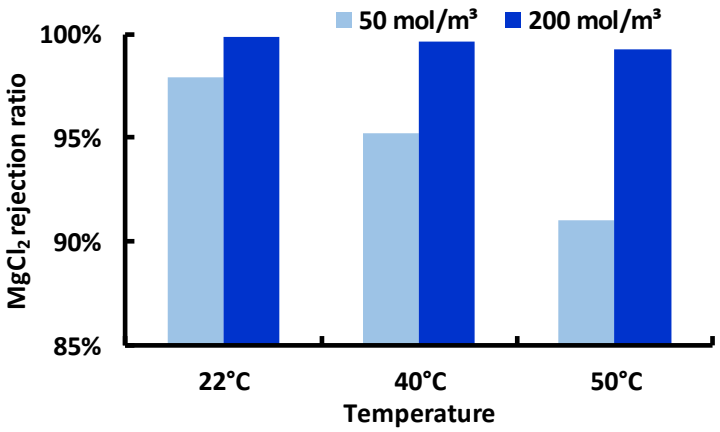

Fig. 2-8a. $MgCl_2$ rejection ratio vs. T

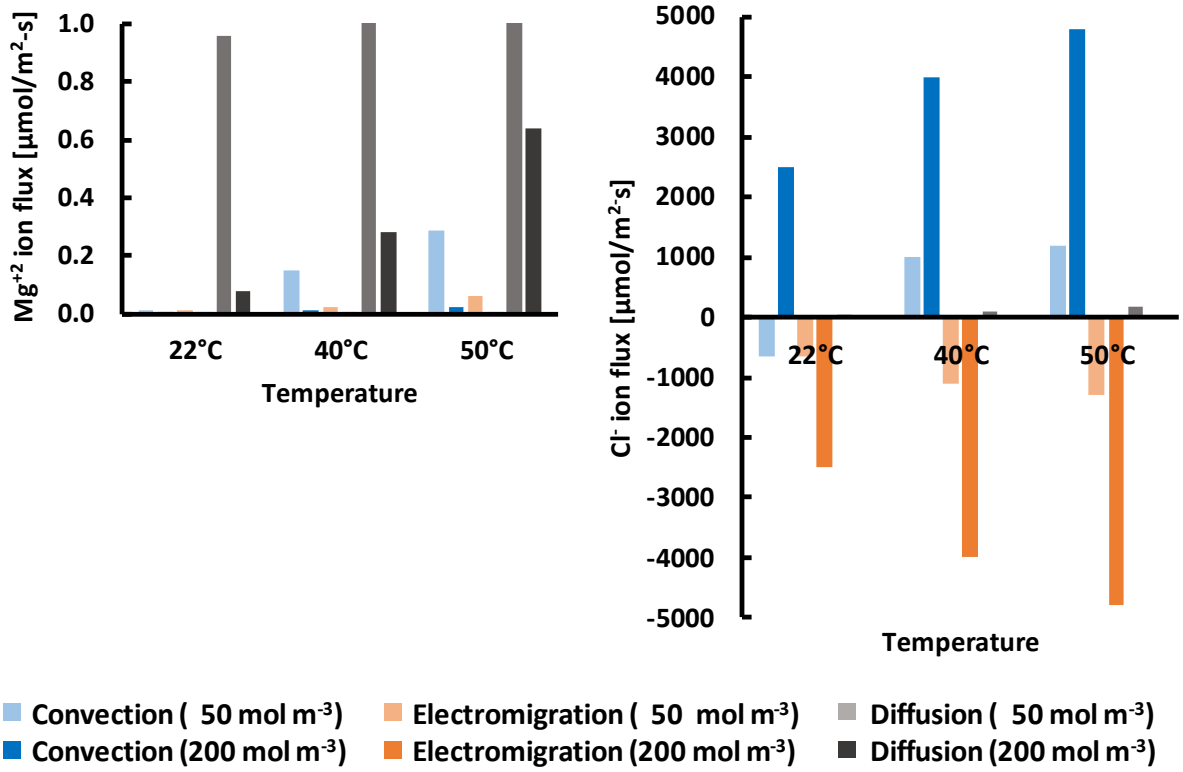

Fig. 2-8b. Mg^{2+} flux vs. T **Fig. 2-8c. Cl^- flux vs. T**

Figure 2-8. For a positively charged NF membrane (50 or 200 mol m^{-3}), modeling results of rejection and solute transport of Mg^{2+} and Cl^- ions in a 0.005M $MgCl_2$ solution at different temperatures and positive membrane charges: (a) rejection of $MgCl_2$; (b) transport of Mg^{2+}ions by the three modes; and (c) transport of Cl^- ions by the three modes.

The trends observed for the magnesium ion for different values of membrane charge (Fig. 2-7 and Fig. 2-8) are very similar to those observed for the sodium ion (Fig. 2-5 and Fig. 2-6). For both

magnesium-chloride and sodium-chloride, salt rejection is higher for a positive membrane charge compared to a negative membrane with equal magnitude of charge, due to steric exclusion. Since both cations are larger than the chloride ion, they experience a high steric exclusion, resulting to reduced movement of itself and its counter-ion into a positive membrane. One exception to the similarities between the salts is that for the chloride ion, as seen from Fig. 2-7c, when negatively charged membranes are considered, electromigration is dominant over diffusion for the magnesium-chloride solution (while for sodium-chloride solution, diffusion was greater in magnitude than electromigration for the chloride ion). This can be explained by looking at the ratio $R_{i,E/D}$:

$$R_{i,\,E/D} = \frac{Electromigration_i}{Diffusion_i} = \left(\frac{C_{i,pore}\Delta\psi}{\Delta C_{i,pore}}\right)\left(\frac{z_i F}{RT}\right) \tag{2-8}$$

Here $\Delta C_{i,pore}$ is the concentration drop across the section of the membrane under consideration, or the entire thickness of the membrane if the concentration profile is linear. The ratio $\left|R_{Cl^-,\,E/D}\right|$ is greater than one in the magnesium-chloride solution while it is smaller than one for sodium-chloride in a negatively charged membrane, which explains why one mode of transport is dominant over the other for the two salts considered. This can be further explained by observing the non-constant terms $C_{i,pore}$, $\Delta\psi$ and $\Delta C_{i,pore}$ in Eq. (2-8) for the magnesium-chloride and sodium-chloride solutions, as discussed presently. For the chloride ion, at any given value of negative membrane charge, the mean concentration within the membrane $C_{i,pore}$ and potential drop across the membrane $\Delta\psi$ are higher for the magnesium-chloride solution compared to the sodium-chloride solution. On the other hand, the concentration drop across the membrane $\Delta C_{i,pore}$ is lower for the magnesium-chloride solution compared to the sodium-chloride solution. The reason for the

higher intra-membrane concentration of chloride ions in the case of magnesium-chloride compared to sodium-chloride is due to the higher valence of magnesium compared to sodium, thereby drawing more chloride into the membrane to maintain intra-membrane electro-neutrality. Although the number of equivalents (i.e. number of units of charge provided by the ion) of Na^+ and Mg^{2+} inside the membrane are approximately equal (and equal to the membrane volumetric charge density), the concentration of the ion of higher valence is marginally higher (and increases as the valence of the ion increases, even if the feed concentration of the Cl^- is kept same overall all cases to ensure a fair comparison). Since the Cl^- has a lower concentration in the membrane (it has the same charge as the membrane and is electrically repelled by it), even a small difference in the number of equivalents of Na^+ and Mg^{2+} in the membrane causes a large difference in the number of equivalents of Cl^- present. For example, considering the NaCl solution, for a membrane of −200 mol/m^3 charge at 50^{o}C, the mean intramembrane concentration of Na^+ is 200.2 mol/m^3 and that of Cl^- is thus 0.2 mol/m^3. In comparison, for the $MgCl_2$ case, the intramembrane concentration of Mg^{2+} is 100.4 mol/m^3 (i.e., 200.8 equivalents of Mg^{2+} per m^3), and the Cl^- concentration is 0.8 mol/m^3 (four times as large as the NaCl case). Thus, a difference of only 0.3% in the number of equivalents of Mg^{2+} compared to Na^+ resulted in the Cl^- concentration to be four times in the $MgCl_2$ case compared to the NaCl case. As mentioned above, the concentration drop of Cl^- across the membrane $\Delta C_{i,pore}$ is lower for the magnesium-chloride solution compared to the sodium-chloride solution. This is explained by the lower rejection ratio in the magnesium-chloride case, leading to a smaller drop of concentration from feed to permeate side. The potential drop across the membrane is higher in magnesium-chloride since the magnesium ion is larger: in negatively charged membranes, electromigration counteracts convective transport thus limiting accumulation of positive charges in the permeate solution (29). Consequently, a larger ion requires a higher

potential gradient to drive it back through the membrane to the feed side. Thus, the preceding comparison between the respective $C_{i,pore}$, $\Delta\psi$ and $\Delta C_{i,pore}$ terms of Cl^- in the magnesium-chloride case and the sodium-chloride case explains why the ratio $R_{Cl^-,\,E/D}$ is larger than one in the former case and smaller than 1 in the latter case. This discussion thus explains the reason for the exception to the similarities between trends observed for magnesium-chloride and sodium chloride; that for the chloride ion, in a negatively charged membrane electromigration is dominant over diffusion in the magnesium-chloride solution.

2.4.3.3. Negative rejection of $MgCl_2$

For a membrane with −50 mol/m^3 charge, the magnesium-chloride solution shows a negative rejection ratio (Fig. 2-7a), meaning that, in steady state, the concentration of the salt is higher on the permeate side than the feed side. This also results in the diffusive flux of both ions to be in the negative direction, from permeate to feed, opposite to the overall solute flux (diffusion always takes place from the region of higher concentration to lower concentration). The rejection ratio becomes positive as soon as the charge is slightly increased or decreased (by about 40 mol/m^3). The rejection ratio is negative at −50 mol/m^3 because the membrane offers adequate attractive force to the magnesium ions, while not allowing the repulsion towards the chloride ions to dominate. On the other hand, making the membrane more positive offers increased repulsion towards the magnesium ions. Even at zero membrane charge, a small positive rejection of magnesium-chloride is observed, since the ions still experience steric exclusion and there is no help from the membrane charge to draw the ions in. At −50 mol/m^3 membrane charge, the rejection ratio is negative for all three temperatures, and the rejection ratio of magnesium-chloride increases (becomes less negative) with increasing temperature, in contrast to all other cases studied. This increase in rejection ratio with increase in temperature occurs because the permeate-side

partitioning effect (Eq. 2-3) for the dominant intra-membrane ion, Mg^{2+}, increases with temperature and hence the drop in concentration from within the membrane to the permeate solution becomes sharper. Despite the increase in rejection ratio with temperature, the net solute transport of magnesium-chloride increases with temperature due to the increasing water flux, thereby increasing the convective salt flux. The mean intramembrane concentration of both ions also increase with increase in temperature.

2.4.3.4. Summary and implications of $MgCl_2$ transport at higher temperature

1. Similar to the case of NaCl in section 2.4.2., the dominant influence on solute transport with increasing temperature was the cumulative temperature-induced changes in membrane properties, while only a small impact was made by temperature-induced changes in solvent viscosity and solute diffusivity combined.
2. Similar trends were observed for the Mg^{2+} and Na^{+} ions (c.f. section 2.4.2.) for the impact of temperature and membrane charge density on solute transport modes and ion rejection.
3. For both NaCl and $MgCl_2$, the salt rejection is higher for a positively charged membrane of a given magnitude, compared to a negatively charged membrane of equal magnitude.
4. In a negatively charged membrane, the intramembrane concentration of Cl^{-} is higher for the $MgCl_2$ case compared to the NaCl case because the Mg^{2+} ion (which has a higher valence than the Na^{+}) pulls in more chloride ions. In general, a cation of higher valence has a marginally higher intramembrane concentration for a given fixed (negative) membrane charge value, but this has a magnified effect on the anion concentration, and the anion intramembrane concentration increases significantly for cations of larger valence. For a fair comparison in this discussion, as the valence of the cation is increased, the chloride ion

concentration in solution is kept equal for all salts by reducing the net salt concentration. For example, 0.01M NaCl and 0.005M $MgCl_2$ have the same molar concentrations of Cl^- ions in solution.

5. It is possible to obtain a negative rejection ratio of $MgCl_2$ for a certain value of negative membrane charge density, such that the rejection ratio increases (becomes less negative) with increase in temperature.

2.4.4. Effect of dielectric exclusion on solute transport

In nanofiltration, dielectric exclusion is an important mode of solute exclusion, along with steric and charge-based exclusion. In the previous sections of this work, the effect of dielectric exclusion was not considered, since our approach is to examine the impact of membrane parameters individually. In the model used for this work, dielectric exclusion governed only by the Born effect is considered, which accounts for the solvation energy barrier for the ion to enter the pore, resulting in a decreased dielectric constant of the solvent within the pore. Thus, the Born effect accounts for the energy penalty for an ion to shed its hydration shell when moving from a fully solvated state in bulk solution to the constricted passage within the pore, where there isn't enough 'space' for all of the ion's hydration shells. Dielectric exclusion works to reject ions irrespective of their charge, unlike the charge-based exclusion (wherein the charged membrane attracts counter-ions while repelling co-ions).

2.4.4.1. Variation of pore dielectric constant with temperature

According to Bowen et al. (3), the expression for dielectric constant within the membrane pores can be given by the expression in Eq. 2-9 which assumes that the solvent, i.e. water molecules,

occur in a thin annulus lining the inner pore periphery and the enclosed region has bulk dielectric properties.

$$\varepsilon_{pore}(T) = 80 - 2(80 - \varepsilon^*(T))\left(\frac{d}{r_{pore}(T)}\right) + (80 - \varepsilon^*(T))\left(\frac{d}{r_{pore}(T)}\right)^2 \quad (2\text{-}9)$$

In Eq. 2-9, ε_{pore} is the effective dielectric constant of water within the pore, ε^* is the dielectric constant of the annulus of water covering the inner wall of the pore, r_{pore} is the pore radius and d is the thickness of one water molecule. The above expression gives the temperature-dependent pore dielectric constant as a function of the temperature-dependent pore radius and dielectric constant of the annulus of water lining the pore inner surface. According to Bowen et al. (3), the dielectric constant of the ordered layer of water forming the annulus, ε^* was found to be 31 from their experiments at 25°C. Since the extensive experimentation to determine the exact variation of this quantity as a function of temperature is beyond the scope of the current work, the dielectric constant of the oriented water molecules is assumed to change similarly to that of bulk water over the given temperature range and thus to decrease by 10.87% from 22°C to 50°C (45). Equation 2-9 is thus used to estimate the pore dielectric constant at 50°C, by using fitted values of pore radius from Amar et al. (22), assuming the size of the water molecule does not change with temperature. According to this calculation, the intra-pore dielectric constant at 50°C is found to be 45.37. Using the same approach, the pore dielectric constant is 44.11 at 22°C. Although Roy et al. (25)use a pore dielectric constant of 56.5 for the Desal5DK membrane to match the results for seawater desalination in the SWCC Umm Lujj plant at 25°C, Eq. 2-9 provides a different value. Without further efforts on experimental determination of the pore dielectric constant, it is not possible to

arrive at a more conclusive value of pore dielectric constant; furthermore, the value may also depend on the feed composition. Bowen et al. (3) used a sodium-chloride solution to obtain their value for the dielectric constant of the ordered water layer (ε^*) used in Eq. 2-9.

2.4.4.2. Sensitivity of NaCl rejection to pore dielectric constant

In this section, the impact of the pore dielectric constant on solute transport will be illustrated. For instance, the simulation results show that in going from a pore dielectric constant value of 80.4 to 45 (decrease by ~44%), the solute transport of sodium-chloride at 50°C at membrane charges of 0, −50 mol/m^3 and −200 mol/m^3 reduced by about 6%, 56% and 82% respectively. The value of pore dielectric constant to compare against, 80.4, was chosen because it is the bulk dielectric constant of water and hence when the pore dielectric constant is set equal to this value, the Born solvation energy barrier is zero, effectively removing the effect of dielectric exclusion. As stated in section 2.4.4.1., the pore dielectric constant of the Desal5DK membrane at 50°C was estimated to be around 45. The above percentage changes in net solute transport due to pore dielectric constant at fixed values of membrane charge give an indication that dielectric constant is an important factor to consider in explaining the change in rejection ratio of ions with temperature.

2.4.4.3. Effect of dielectric exclusion on solute transport modes and rejection

Due to dielectric exclusion, the convective and electromigrative modes of transport for the chloride ion are significantly reduced, since the dielectric exclusion allows less chloride ions to enter the membrane. Therefore, the intra-membrane concentration $C_{Cl^-,pore}$ is reduced. The intra-pore concentration of the sodium ion has to remain almost unchanged in order to satisfy electroneutrality and so the electromigrative and convective terms for the sodium ion remain practically unaffected by dielectric exclusion in a negative membrane. Although the rejection ratio

is higher due to dielectric exclusion, the concentration gradient across the membrane thickness $\frac{dC_{i,pore}}{dx}$ (and hence diffusive transport) is less compared to when dielectric exclusion is not considered for both Na^+ and Cl^- ions. For a given feed concentration, a higher rejection usually implies a higher concentration gradient through the membrane because of the smaller permeate-side concentration. Conversely, a higher concentration gradient usually signifies a higher rejection ratio. However, due to dielectric exclusion, the net solute transport for both ions is drastically reduced due to the Born exclusion effect and the higher rejection is reflected in a large partitioning effect on the permeate side (cf. Eq. 2-3); hence there is a steeper fall in concentration between a point just within the membrane (on the permeate side) and the permeate concentration.

2.4.4.4. Summary and implications of dielectric exclusion on NF solute transport

1. Increased dielectric exclusion (caused by reduced magnitude of pore dielectric constant) causes the rejection of all ions to increase.
2. Increased dielectric exclusion causes increased partitioning effect at the membrane-solution interfaces and reduced solute transport through the membrane.

2.4.5. Seawater Nanofiltration at different temperatures

In this section, the solute transport and rejection ratio for each ion in seawater is analyzed at two different temperatures. This analysis is pertinent to NF as a pretreatment for thermal desalination systems, in which the feed water temperature may vary over the course of the day or over the year. All membrane parameters (both structural and electrical) were used for the analysis. The minimum and maximum temperatures used in the study thus far (22^{o}C and 50^{o}C) were considered, in order to clearly discern the effect of temperature. The concentrations of the ions in seawater are taken

from Table 2 from Roy et al. (25). The values of the membrane structural parameters and dielectric constant as obtained previously for the Desal5DK membrane at 22°C and 50°C (cf. Table 2-2) are used to simulate the nanofiltration of seawater at these temperatures. In order to simplify the analysis and since the membrane charge of the Desal5DK membrane at different temperatures for seawater feed composition are not known at present, the membrane charge will be kept fixed at −80 mol/m^3 (the value fitted by Roy et al. in (25)). Thus, the present analysis provides insight into the changes in seawater nanofiltration due to the change in membrane structural parameters and pore dielectric constant with temperature. Although the exact fitted values of membrane charge for this feed at both of the two temperatures considered would be desirable for the analysis, the dielectric exclusion effect evaluated using the pore dielectric constants mentioned in section 2.4.4.1 (44.11 and 45.37 respectively for 22°C and 50°C) is significant and is in fact the dominant mode of exclusion (over steric and Donnan exclusion) at both temperatures. For the analysis, one spiral-wound membrane element will be simulated using the model developed by Roy et al. (25)and the variation of water recovery ratio and rejection ratio with temperature will be observed in addition to the solute transport of each ion.

Table 2-2. The following table summarizes the membrane parameters used at 22°C and 50°C:

Parameter	Pore radius r_{pore}[nm]	Effective active layer thickness $\Delta x / A_k$ [µm]		Membrane volumetric charge density C_X[mol/m^3]	Pore dielectric constant ε_{pore}
		from solute	from water		
Value at 22°C	0.58	0.98	2.20	−80	44.11
Value at 50°C	0.67	0.56	2.67	−80	45.37

Source	Amar et al. (22)	Amar et al. (22)	Roy et al. (25) (assumed constant for this analysis)	Calculation using Eq. 2-9

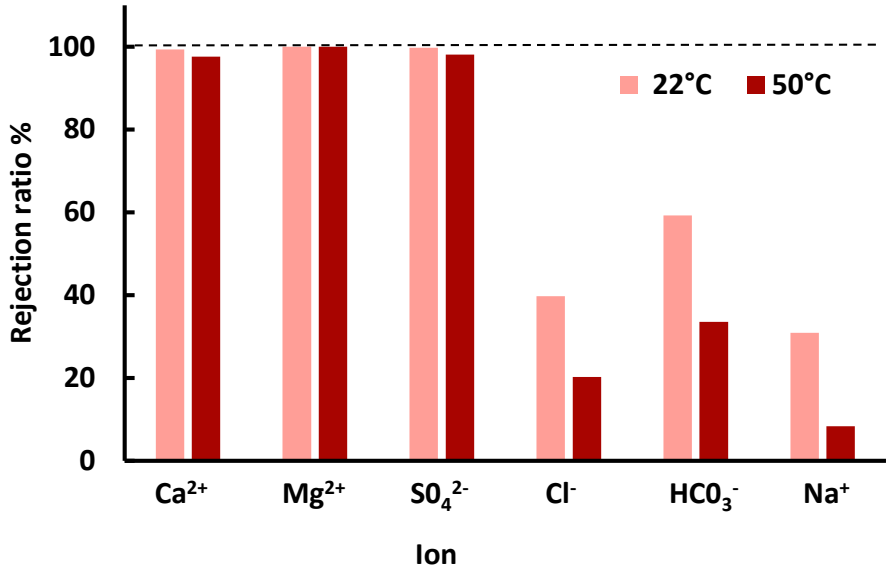

Figure 2-9. Rejection ratios of the primary ionic constituents of seawater at 22°C and 50°C as obtained from modeling a single element of a spiral-wound module at those temperatures.

Figure 2-9 shows that the rejection ratios of the divalent ions calcium, magnesium and sulfate are almost 100% at both temperatures, although the rejection ratio decreases slightly at the higher temperature. The monovalent ions are rejected to a much lesser extent and the maximum rejection among them is observed for the bicarbonate ion.

Figure 2-10 shows the solute transport by each mode for each ion at the two temperatures considered. In Fig. 2-10, the diffusion values for the Na^+ and Cl^- ions at 50°C (dark grey) are not shown entirely since they are too large. In this figure, the value shown is ~7000 µmol/m^2-s at 50°C for both ions, but in fact they go up to ~15700 µmol/m^2-s and ~16700 µmol/m^2-s respectively.

Results for seawater ions other than Na^+ and Cl^- are shown in the supplementary information to focus on the non-dominant ions.

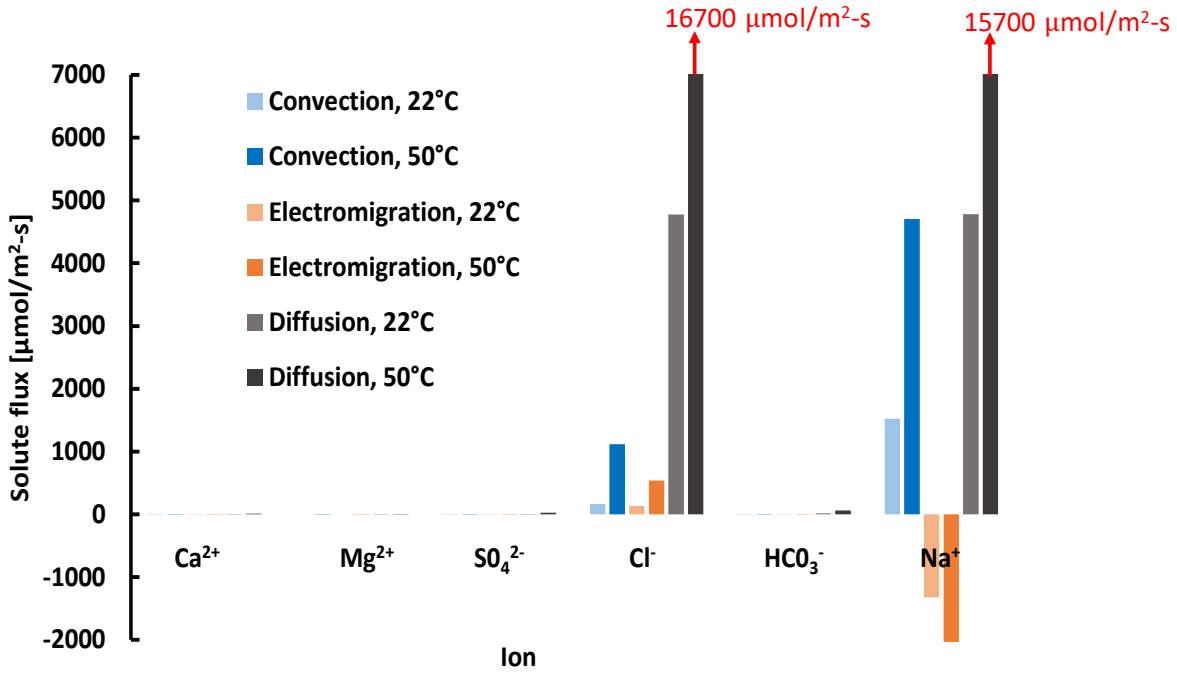

Figure 2-10. Flux of ions in seawater through a negatively-charged (-80 mol m^{-3}) NF membrane, by the three different modes (convection, electromigration, and diffusion) at 22°C and 50°C. Conditions were obtained from modeling a single element of a spiral-wound module at those temperatures. The diffusion values for the Na^+ and Cl^- ions at 50°C (dark grey) are not shown entirely since they are too large. In this figure, the value shown is ~7000 µmol/m^2-s at 50°C for both ions, but in fact they go up to ~15700 µmol/m^2-s and ~16700 µmol/m^2-s respectively. Results for seawater ions other than Na^+ and Cl^- are shown in the supplementary information to focus on the non-dominant ions.

2.4.5.1. Effect of feed concentration and membrane exclusion modes on seawater ions

Considering a seawater feed, the net solute transport for each of the divalent ions and bicarbonate is a few orders of magnitude less than that of the chloride and sodium ions (Fig. 2-10). This is partly due to the fact that the feed concentration of the sodium and chloride ions are much higher than that of the other ions in seawater; and partly due to the much larger exclusion experienced by

the divalent ions, mainly in the form of dielectric exclusion. The dielectric exclusion is highest for the magnesium ion, followed by the calcium ion, the sulfate ion and then the monovalent ions. The negative charge on the membrane is predominantly neutralized by the sodium ions, since it has the highest intra-membrane concentration. Although this is slightly surprising, considering the negatively charged membrane attracts the positive divalent ions most strongly into the membrane, it can be explained by the fact that the dielectric exclusion is higher for the two divalent cations and this effect dominates that of the charge-based attraction. Furthermore, the feed concentration of calcium and magnesium are much lower than that of the sodium ion, thereby reducing the amount of these ions 'available' to enter the membrane. The two monovalent anions chloride and bicarbonate experience similar magnitudes of steric, dielectric and Donnan exclusion, however the intra-membrane concentration of the bicarbonate is much lower than that of the chloride due to its smaller feed concentration and hence lesser 'availability'. Unsurprisingly, the divalent anion sulfate experiences the largest amount of charge-based exclusion and also has high steric and dielectric exclusion causing high rejection. The above arguments explain why the intra-membrane concentration in the descending order is sodium, chloride, bicarbonate, sulfate, calcium and magnesium. In seawater, the convective mode is more dominant than the electromigrative mode for the sodium and chloride ions, as shown in Fig. 2-10. This dominance of convection occurs because the membrane potential for the seawater case is sufficiently low to bring the weight of the electromigrative term down.

2.4.5.2. Percentage change in rejection of individual ions with temperature

In regard to seawater feed, the net solute transport of the divalent ions is a few orders of magnitude less than that of the monovalent ions at both temperatures. However, the increase in net solute

transport from 22°C to 50°C is higher for the divalent ions (10-30 fold) than the monovalent ions (3-5 fold). For the divalent ions, the mode of transport that increases the most sharply is the diffusive mode, while for the monovalent ions, it is the convective mode. The exception to this trend is Na^+, for which diffusion increases marginally greater than convection. Such a sharp increase in the diffusive mode for the divalent ions is attributed to the sharp increase in the intra-membrane concentration on the feed side (just within the membrane), for the temperature rise from 22°C to 50°C due to the sharp change in the partitioning effects. This increase in concentration within the membrane facing the feed side results in a larger concentration gradient within the membrane and thus increased diffusion. The percentage change of the rejection ratio of the divalent ions with increase in temperature is lower than that of the monovalent ions, however, partly because their numerical values are larger. Overall, for the membrane studied and the given feed composition, the rejection ratio of the calcium ion shows the greater sensitivity to temperature (higher percentage decrease in rejection ratio with increase in temperature) between the two divalent cations. The sodium ion rejection has the largest percentage decrease in rejection ratio with increase in temperature among monovalents, and the chloride and bicarbonate rejections show almost equal percentage change in rejection ratio for the temperature change. Finally, the recovery ratio for the single element was seen to increase from 8.3% at 22°C to 23.9% at 50°C.

2.4.5.3. Summary and implications for seawater transport at higher temperature

1. Rejection ratio of all divalent ions is ~100% at both temperatures studied, although it reduces slightly at the higher temperature. The rejection ratios of the monovalent ions are significantly less than that of the divalent ions at both temperatures and reduce notably with increase in temperature.

2. Solute transport of each ion through the membrane depends on its feed concentration. Regarding each of the divalent ions and the bicarbonate ion, their feed concentrations are significantly lower than that of sodium and chloride ions in seawater. This factor contributes to their net solute transport being a few orders of magnitude less than that of the sodium and chloride ions.
3. Each of the divalent ions experience large exclusion by the membrane, predominantly in the form of dielectric exclusion, resulting to their lower transport through the membrane relative to sodium and chloride ions. In fact, the sodium and chloride ions have the greatest intramembrane concentration. Even though the negatively charged membrane attracts the divalent cations more strongly, their entry is restricted by exclusion effects.
4. The percentage increase in net solute transport with temperature is significantly higher for the divalent ions compared to the monovalent ions. This trend in solute transport among the ions in seawater is due to the reduction in the exclusion mechanisms at the higher temperature, which affects the divalent ions more strongly.
5. The percentage decrease in rejection ratio with increase in temperature is lower for the divalent ions compared to the monovalent ions.
6. As a result of the change in membrane parameters and the decrease in solvent viscosity, overall membrane water flux increases substantially at higher temperatures. For a spiral-wound element operating on Arabian Gulf seawater, the water recovery increases from 8.3% at 22^{o}C to 23.9% at 50^{o}C as per the modeling analysis.

2.4.6. Summary of temperature effects

A summary of how the important model parameters and results change with temperature is provided in the following table. For this analysis, only one parameter is changed at a time and a positive rejection ratio regime, as seen in most cases described in the paper, is assumed.

Table 2-3. The following table summarizes how the important model parameters and results change with temperature

Expression	Variable	Change at higher temperature	Impact on membrane performance
ν	Solvent kinematic viscosity	Decreases	Increase in solvent flux, which by itself increases rejection ratio. However as per Stokes-Einstein Eq. (ref. (Nilsson, Tragardh, & Ostergren, 2008)) a decrease in viscosity increases ion diffusivity, which lowers rejection ratio.
r_{pore}	Pore radius	Increases (c.f. ref (22))	Increase in solvent flux Reduction in steric hindrance of solutes.

$\left(\Delta x/A_k\right)_{solute}$	Effective membrane thickness (from solute)	Varies (c.f. ref(22))	A reduction in this parameter causes reduced rejection ratio
$\left(\Delta x/A_k\right)_{water}$	Effective membrane thickness (from water)	Varies (c.f. ref (22))	A reduction in this parameter causes increased solvent flux
D_i	Solute diffusivity	Increases	Reduced rejection ratio
ε_{pore}	Pore dielectric constant	Increases	Increase in this parameter causes reduced dielectric exclusion and hence reduced rejection ratio
	Ion rejection	Generally decreases, increases (becomes less negative) when ion rejection is in negative regime	
$-D_{i\,pore}\frac{dC_{i,pore}}{dx}$	Diffusive transport	Increases in magnitude	
$K_{i,c}C_{i,pore}J_w$	Convective transport	Increases in magnitude	
$-\frac{z_i C_{i,pore} D_{i,pore}}{RT} F \frac{d\psi}{dx}$	Electromigrative transport	Increases in magnitude	

Φ_i	Steric exclusion	Decreases due to pore expansion
Φ_B	Dielectric exclusion	Decreases due to increase in pore dielectric constant
$exp\left(-\frac{z_i F}{RT}\psi_D\right)\Big\|_{interface}$	Donnan partitioning	Reduces for membrane counter-ion, increases for membrane co-ion

2.5. Chapter 2 conclusions and outlook

To the authors' knowledge, the present work is the first to examine the impact of temperature on nanofiltration, examining the mechanisms of solute transport and exclusion in different feed solutions at different temperatures. The DSPM-DE model is used in which solute transport is described by the Nernst-Planck equation within the membrane, thereby capturing three different modes of solute transport: the convective, diffusive, and electromigrative modes. The DSPM-DE model involves three exclusion mechanisms governing entry of solute into the membrane: the steric, dielectric, and Donnan exclusion mechanisms. Each of these modes of transport and exclusion for individual ions vary with temperature, thereby affecting how a given membrane rejects ions differently at different temperatures. Ions differ from one-another in terms of size, valence, and diffusivity and these factors, coupled with changes in the membrane itself due to temperature determine which ions show greater change of rejection with temperature change.

Apart from those mentioned in the section summaries/implications, the following conclusions are obtained from this study:

1. Electroneutrality within the membrane is the key driving factor in determining how much of each ion enters the membrane at a given value of water flux. When several ions of like charge are present, the exclusion mechanisms are the deciding factor for competition among the different ions and determine which ions are 'preferred' to enter the membrane.
2. In the analysis of seawater ions, one major effect causing large rejection of scale-causing divalent ions (Mg^{2+}, Ca^{2+}, SO_4^{2-}) is the large dielectric exclusion experienced by these ions. Thus, lower ε_{pore} causing greater dielectric exclusion is beneficial for NF membranes aiming to remove these scalants.
3. In light of the preceding discussions, for higher temperature applications, membranes with lower temperature-dependent structural changes are desirable. Specifically, membranes whose pore radius increases less are preferred not only because they can maintain high steric exclusion, but also low intra-pore dielectric constant (cf. Eq. 2-9) resulting in high dielectric exclusion. Regarding membrane charge, the desired value depends on the ions to be rejected. For membranes attempting to remove Mg^{2+} and Ca^{2+}, an increased negative charge with temperature is disadvantageous. A higher negative membrane charge will aid rejection of the SO_4^{2-} ions, however.

Experimental work to accurately fit the membrane charge and pore dielectric constant as a function of temperature is desirable in future, although the present analysis provides clear insight into the nature of changes in solute transport and rejection that occur as a result of temperature change.

3. Contributive factors to the change in permeate quality upon temperature variation in nanofiltration

3.1. Introduction

Nanofiltration (NF) is a pressure-driven membrane-based solution treatment method, similar to reverse osmosis (RO). Streams entering NF may occur over a wide range of temperatures, depending on the source. For example, effluents from textile, electroplating and pharmaceutical industries can range between 25-70^{o}C (8,46–48). The introduction of specialty high temperature membranes by Dow in 2016 testifies to the practical significance of high temperature NF and RO (49). While several examples in the literature discuss changes in salt rejection and water flux with change in temperature (9,10,23), relatively few explore why species transport through the membrane changes with temperature. Because the temperature-dependence of solute diffusivity and solvent viscosity are well-studied, authors generally attribute reduced uncharged solute retention rate and increased solvent flux at higher temperature to the increased diffusivity and solvent viscosity respectively (9,50) However, transport in NF is known to depend on various membrane properties, including pore size, membrane charge, and selective layer tortuosity (3,25). Therefore, accounting for temperature-induced changes of these quantities may be significant in explaining variations in membrane selectivity due to temperature. Certain references do discuss membrane properties in the context of temperature variation: Amar et al. (22) prove through their modeling work on uncharged solutes that only species mobilities (solute diffusivity and solvent viscosity) cannot account for the observed changes in rejection ratio with temperature change, and

references (46) and (34) qualitatively discuss pore radius change with temperature as a potentially significant contributor to selectivity changes. However, a quantitative comparison of various contributors relevant to charged species is lacking in literature.

The study of charged species is more complicated than uncharged solutes: salt retention may stay unchanged, increase or decrease with temperature (9,10). Furthermore, both structural aspects of the membrane and membrane charge could change with temperature, thereby affecting selectivity. The change in membrane charge with temperature has been studied previously (51,52), but there is lack of clarity on the relative magnitude of this effect, compared to membrane structure changes or mobilities. In this work, the effects of individual membrane properties and species mobilities, as well as various groups of parameters (membrane properties vs. mobilities and membrane structural properties vs. charge) on NF selectivity will be studied. Conclusions are drawn based on results from three feed compositions and two membranes, and the results are explained using an analytical framework. Changes in membrane selectivity will be accounted for through changes in salt permeate concentration, since this quantity directly indicates permeate quality.

3.2. Governing Equations

The governing equations for species transport in nanofiltration (NF) are implemented numerically using MATLAB vR2016a for this work. These equations together constitute the Donnan Steric Pore Model (DSPM) and are summarized in Table 3-1 (53). Successful use of this model for NF has been widely reported (29,31,44,51,53,54). For all experimental data sets studied, concentration polarization is considered negligible, hence Eq. 3-2 uses the bulk feed concentration $C_{i,f}$. The expression for the reflection coefficient σ (Eq. 3-5) applicable to charged species is derived by Bandini et al (50). Temperature dependence of solute mobility (diffusivity $D_{i,\infty}$) is accounted for

by the Stokes-Einstein equation (55,56) and water mobility (μ_w) values are taken from reference (45).

Table 3-1: Governing equations for species transport in NF

Equation	Significance	
$J_i = -D_{i,\infty}K_{i,d}\frac{dC_{i,pore}}{dx} - \frac{z_iF}{RT}D_{i,\infty}K_{i,d}C_{pore}\frac{d\psi}{dx} + K_{i,c}C_{i,pore}J_w$	Ion flux	(3-1)
$\frac{\gamma_{i,pore}C_{i,pore}}{\gamma_{i,f}C_{i,f}} = \phi_i \exp\left(-\frac{z_iF}{RT}\Delta\psi_{D,f}\right)\Big\vert_{in}$	Extent of ion partitioning by membrane between feed solution and pore-entry	(3-2)
$\frac{\gamma_{i,pore}C_{i,pore}}{\gamma_{i,p}C_{i,p}} = \phi_i \exp\left(-\frac{z_iF}{RT}\Delta\psi_{D,p}\right)\Big\vert_{out}$	Extent of ion partitioning by membrane between pore-exit and permeate solution	(3-3)
$\left(\sum_{all\ ions} z_iC_{i,pore}\right) + C_X = 0$	Electroneutrality inside membrane pores	(3-4)
$J_w = \frac{r_{pore}^2}{8\mu_w\Delta x_w}(\Delta P_{applied} - \sigma\Delta\pi)$	Water flux	(3-5)
$J_s = J_wC_{s,p}$	Salt flux in pressure-driven membrane processes, in terms of J_w and $C_{s,p}$	(3-6)
$\Rightarrow \frac{dC_{s,p}}{C_{s,p}} = \frac{dJ_s}{J_s} - \frac{dJ_w}{J_w}$	Change in $C_{s,p}$ in terms of changes in J_s and J_w, following differentiation of Eq. 3-6	(3-7)

3.3. Validation with experimental data and temperature-dependent parameter change

As shown in Fig. 3-1, the model was validated for the lowest and highest temperatures for 4 data sets (0.001M NaCl (with the TFCS membrane by Koch Fluid Systems) (51),0.1M NaCl, 0.1M Na_2SO_4 and 0.001M NaCl (the last three data sets used the Desal5DK membrane by GE Osmonics) (52)). These four data sets are named A, B, C and D respectively. Table 3-2 provides a summary of the reference data sets. Pore radii at each temperature were taken from the associated references and values for δ_w were obtained from rearranging Eq. 3-5. The two fitting parameters were Δx_s and C_X and unique pairs of optimal values for each data set were obtained after minimizing the least square error on salt flux. This fitting procedure is similar to that of Sharma et al. (51) and hence comparable values of these parameters are obtained (Fig. 3-2). Upon fitting with the other data sets, temperature-dependent trends are obtained: as shown in Fig. 3-3, net path length through the selective layer of both water and salt (Δx_w and Δx_s), and the magnitude of negative membrane charge increased due to temperature increase. The increase in path length for all species is explained by the increase in selective layer tortuosity (57), and the larger membrane charge is due to the combined effect of enhanced anion-adsorption and membrane functional-group dissociation at higher temperatures. These mechanisms are discussed in further detail in section 2.4.4. Increase in pore radius with temperature rise is commonly reported ((22,51,55,58)) and is also observed for the current data sets. Values for pore size were taken from the reference literature containing the experimental data, and were obtained by fitting with uncharged solute data by those authors (22,57).

Table 3-2: Summary of experimental data sources:

Data set	Reference	Feed composition	Membrane	Temperatures	Highest applied pressure
A	(51)	0.001M NaCl	TFCS	5°C and 35°C	7.5 bar
B	(52)	0.1M NaCl	Desal5DK	22°C and 50°C	15 bar
C	(52)	0.1M Na_2SO_4	Desal5DK	22°C and 50°C	15 bar
D	(52)	0.001M NaCl	Desal5DK	22°C and 50°C	15 bar

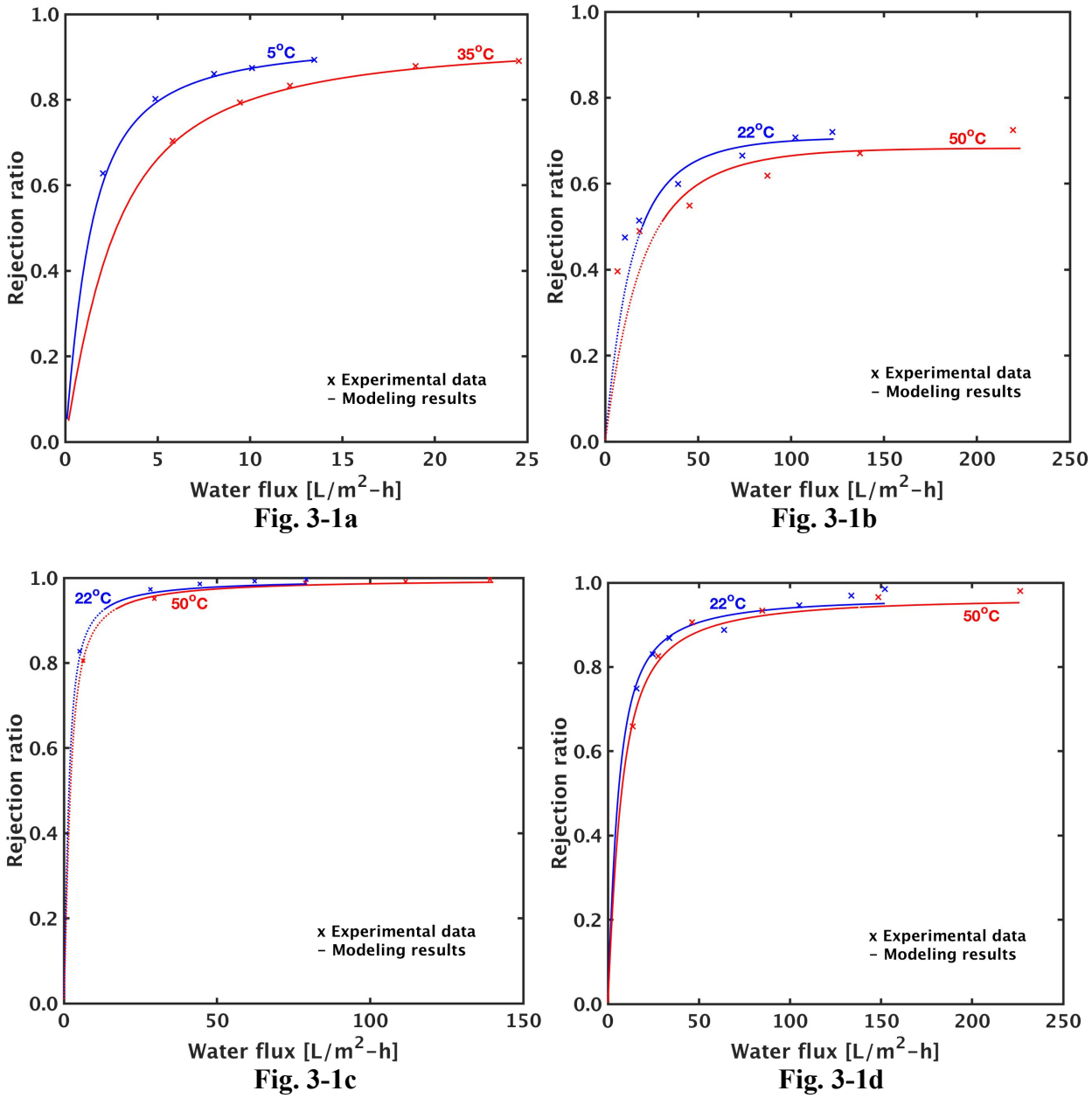

Figure 3-1. Model validation for data sets A, B, C and D (Figs. 3-1a-d)

3.3.1. Change in membrane parameters due to temperature

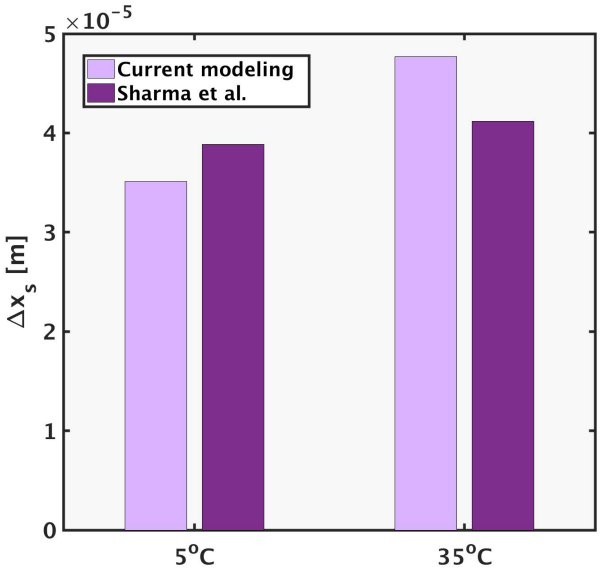

Fig. 3-2a

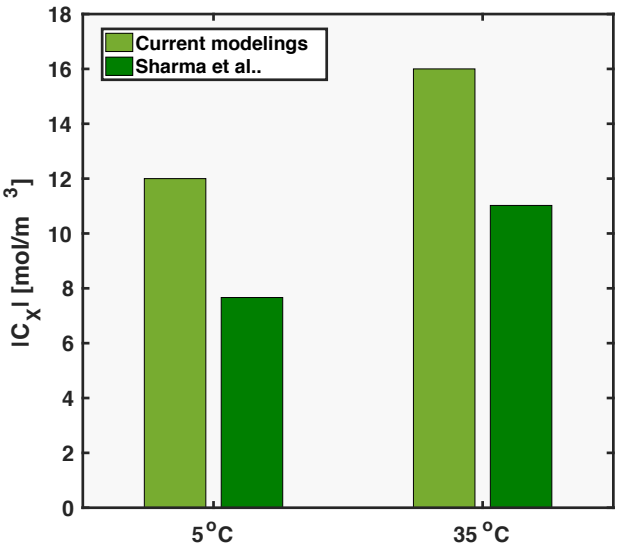

Fig. 3-2b

Fig 3-2. The two independent fitting parameters obtained in the current work are comparable to those in reference (51) for the same experimental data set.

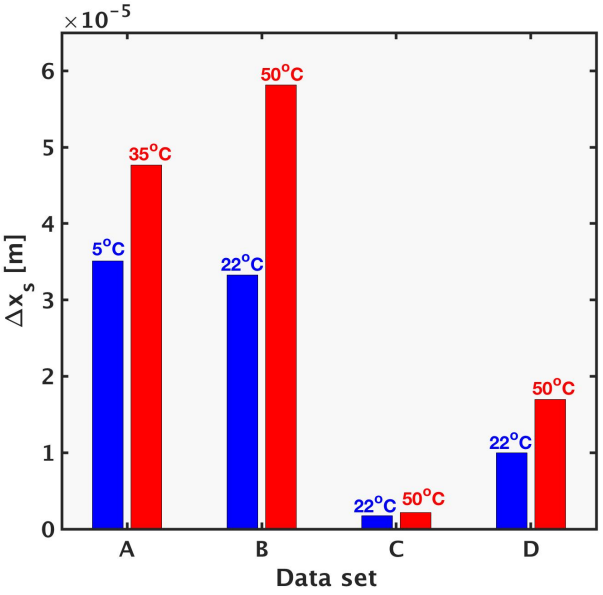

Fig. 3-3a

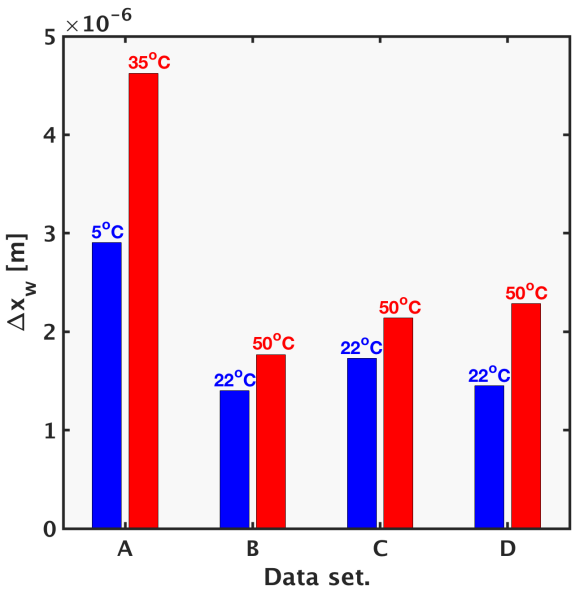

Fig. 3-3b

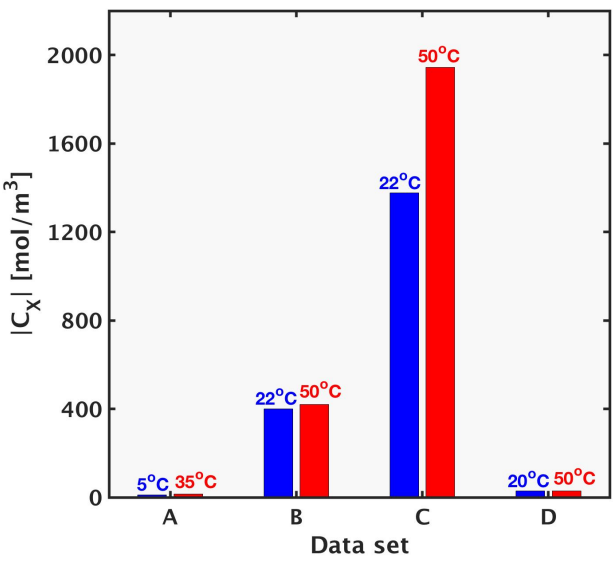

Fig. 3-3c

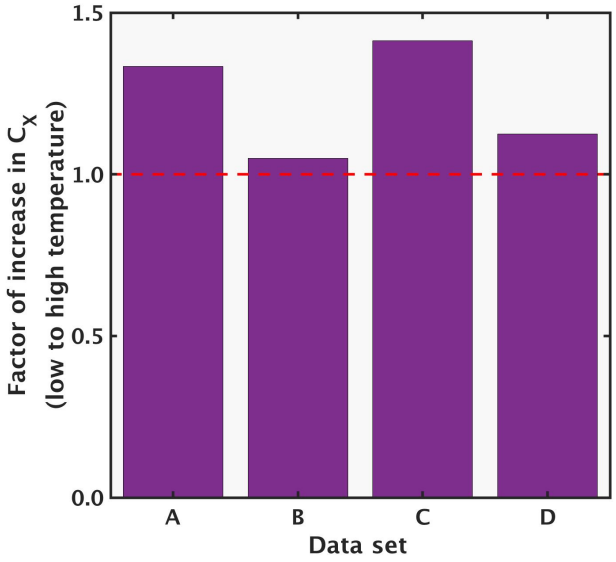

Fig. 3-3d

Fig 3-3. For all data sets (A-D), the same trends due to temperature variation were obtained: increase in pore size, δ_w, Δx_s and magnitude of negative membrane charge, $|C_X|$.

3.4. Results and discussion

In this section, changes in salt permeate concentration,$C_{s,p}$, due to changes in temperature-dependent parameters will be discussed and explained. For instance, the contribution of membrane parameters to changes in $C_{s.p}$ will be shown in certain sections. In those sections, only changes in membrane parameters at the higher temperature (illustrated in Section 3.3.2.) will be implemented in the model, and the corresponding permeate concentration plotted. Similarly, the contribution of mobilities to permeate concentration refers to $C_{s,p}$ values when only mobilities $(\mu_w$ and $D_{i,\infty})$ are changed to higher temperature values. This work focuses on permeate concentration because permeate quality (measured by concentration of solute species) is the focus of treatment methods like NF. Results for data set D are not shown in this section due to numerical instability while varying sub-sets of parameters.

3.4.1. Temperature-based changes in membrane properties and mobilities each alter C_p notably

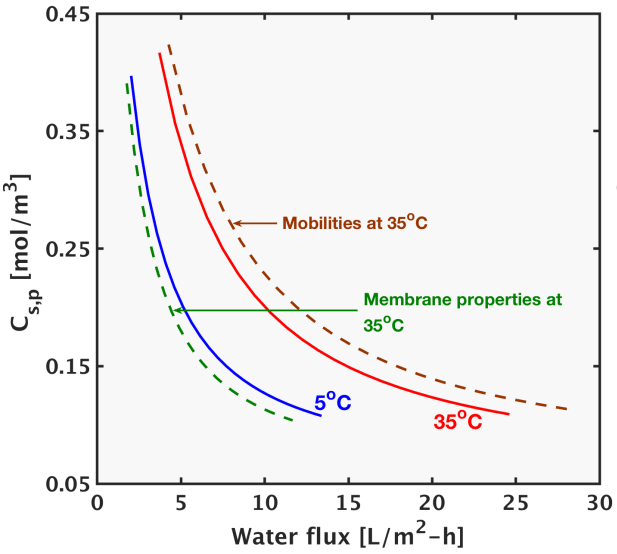

Fig. 3-4a

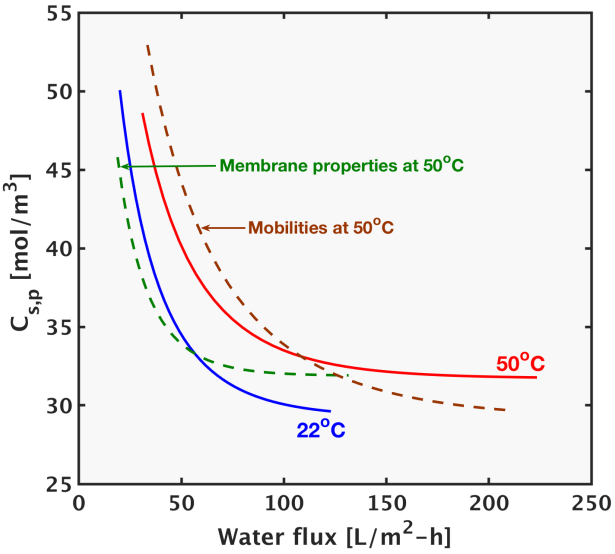

Fig. 3-4b

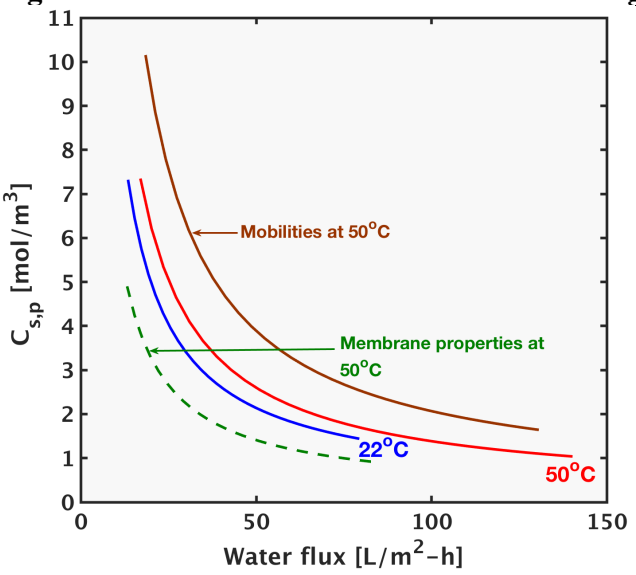

Fig. 3-4c

Fig 3-4. For all data sets (A-C), neither the membrane parameters nor mobilities could by themselves account for the net change in permeate quality from low to higher temperature. Along with the $C_{s,p}$ curves for the low and high temperature for each data set, two other lines are shown: 1. the curve obtained from changing mobilities to values at the higher temperature (holding membrane properties at lower temperature values), 2. The curve obtained by changing membrane parameters at higher temperature values (holding mobilities constant). Since neither one of these lines are coincident with the higher temperature line, both sets of parameters need to be accounted for during temperature variant studies.

For all data sets, the change in $C_{s,p}$ from low to high temperature could not be accounted for due to either the membrane parameters or the mobilities by themselves. The increase in $D_{i,\infty}$ at the higher temperature increases the permeate concentration and is the dominant contribution, between the two mobility factors. Consequently, for data set A and C, and a large range of B, the mobilities line not only lies above the lower temperature line, but also exceeds the higher temperature values. The cumulative contribution of the membrane parameters in almost all cases reduces $C_{s,p}$ below the lower temperature line.

3.4.2. Analytical framework to explain the influence of temperature-dependent parameters on C_p

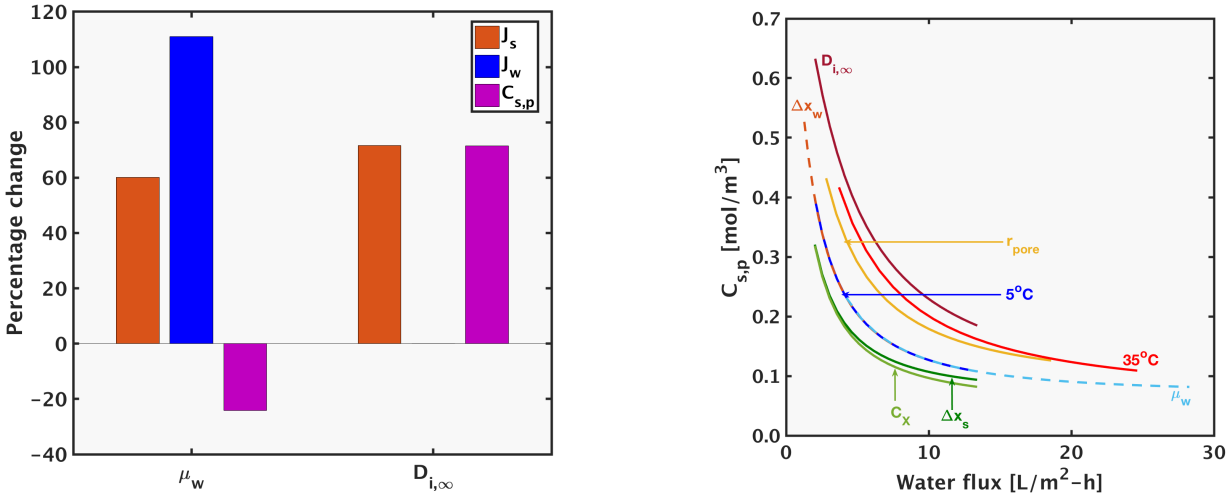

Fig. 3-5a **Fig. 3-5b**

Fig 3-5. Fig 3-5a: The analytical framework (based on Eq. 3-7) can be used to explain the opposing effects of μ_w and $D_{i,\infty}$ on permeate quality. Fig. 3-5b: The effect of individual parameters on permeate concentration (data set A). Each line is obtained by fixing the labelled parameter to its value at the higher temperature of 35°C, while all other model inputs are at the lower temperature (5°C) values.

Equation 3-6 shows the expression for salt flux in terms of water flux and permeate concentration applicable to pressure-driven membrane processes, such as NF and RO. Equation 3-7 gives the differential form of Eq. 3-6. The differential form states that the relative change in permeate

concentration $\left({}^{dC_{s,p}}/_{C_{s,p}}\right)$ is determined by a 'race' between the relative changes in salt flux $\left({}^{dJ_s}/_{J_s}\right)$ and water flux $\left({}^{dJ_w}/_{J_w}\right)$. For example, due to a given change in operating condition, if the salt flux increases to a greater extent than the water flux, the permeate concentration of the salt will increase. This framework can be used to analyze the influence of each temperature-dependent parameter on $C_{s,p}$. Figures 3-5 and 3-6 can therefore be explained using this approach. The relative changes $\left({}^{dC_{s,p}}/_{C_{s,p}}\right)$ and $\left({}^{dJ_s}/_{J_s}\right)$ can be interpreted as percentage changes in the respective quantities: $\left({}^{\Delta C_{s,p}}/_{C_{s,p}}\right)$ and $\left({}^{\Delta J_s}/_{J_s}\right)$ (as discussed in Eqs. 3-8, 3-9 and Fig. 3-5).

Between the mobilities, $D_{i,\infty}$ primarily increases the ion fluxes (and hence salt flux). Its influence on the water flux is negligible in comparison, occurring through a change in permeate osmotic pressure value (Eq. 3-5). Consequently, Eq. 3-7 can be re-written as Eq. 3-8 to explain the influence of $D_{i,\infty}$ on salt permeate concentration. The notation $D_{s,\infty|22^oC} \rightarrow D_{s,\infty|50^oC}$ indicates that only effects due to the change in salt diffusivity from the initial temperature to a higher temperature (22 to 50°C) is accounted for.

$$\left.\frac{\Delta C_{s,p}}{C_{s,p}}\right|_{D_{s,\infty|22^oC}\rightarrow D_{s.\infty|50^oC}} \approx \left.\frac{\Delta J_s}{J_s}\right|_{D_{s,\infty|22^oC}\rightarrow D_{s,\infty|50^oC}} > 0 \tag{3-8}$$

The solvent viscosity appears in Eq. 3-5. Accordingly, the decrease in $\mu_w$with increase in temperature has the effect of increasing solvent flux. The dominant term in Eq. 3-9 is the relative change in J_w, even though $\left({}^{dJ_s}/_{J_s}\right)$ is also affected by the change in water flux. The result is a decrease in $C_{s,p}$ due to the temperature-induced decrease in solvent viscosity.

(3-9)

$$\left.\frac{\Delta C_{s,p}}{C_{s,p}}\right|_{\mu_{w|22^oC}\to\mu_{w|50^oC}} = \left(\frac{\Delta J_s}{J_s} - \underbrace{\frac{\Delta J_w}{J_w}}_{dominant}\right)_{\mu_{w|22^oC}\to\mu_{w|50^oC}} < 0$$

Like $D_{i,\infty}$, the membrane parameters Δx_s and C_X primarily affect $\left({}^{dJ_s}/_{J_s}\right)$. However both of these parameters results in decreased J_s, and hence decreased $C_{s,p}$. The influence of Δx_w is explained similarly to that of μ_w, although the increase in its magnitude with temperature by itself reduces J_w $\left({}^{\Delta J_w}/_{J_w} < 0 \Rightarrow {}^{\Delta C_{s,p}}/_{C_{s,p}} > 0\right)$. The increase in r_{pore} with temperature increases both $C_{s,p}$ (due to lowered steric hindrance) and J_w (Eq. 3-5), hence increasing J_s (Eq. 3-6). For all data sets studied, $\left({}^{dJ_s}/_{J_s} > {}^{dJ_w}/_{J_w}\right)\Big|_{r_{pore|22^oC}\to r_{pore|50^oC}} \Rightarrow \Delta C_{s,p}\big|_{r_{pore|22^oC}\to r_{pore|50^oC}} > 0.$

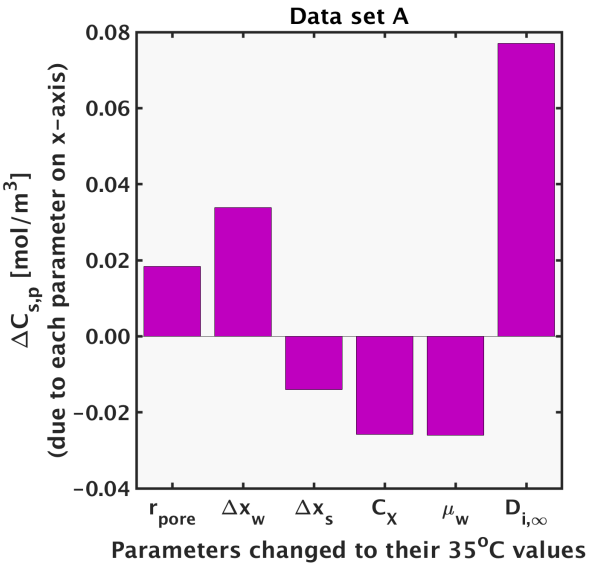

Fig. 3-6a

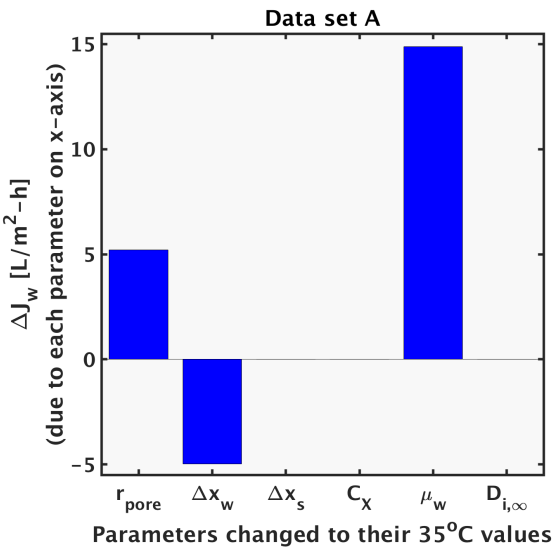

Fig. 3-6b

Fig 3-6. Effect of individual parameters on permeate concentration and water flux due to temperature change (each parameter on the x-axis is changed to its value at the higher temperature holding all other model inputs at the lower temperature). Results are shown for data set A (low and high temperature are 5 and 35ºC respectively), and trends of increase or decrease of $C_{s,p}$ due to each parameter holds for all data sets.

3.4.3. Dominance of membrane parameters over mobilities with increasing pressure

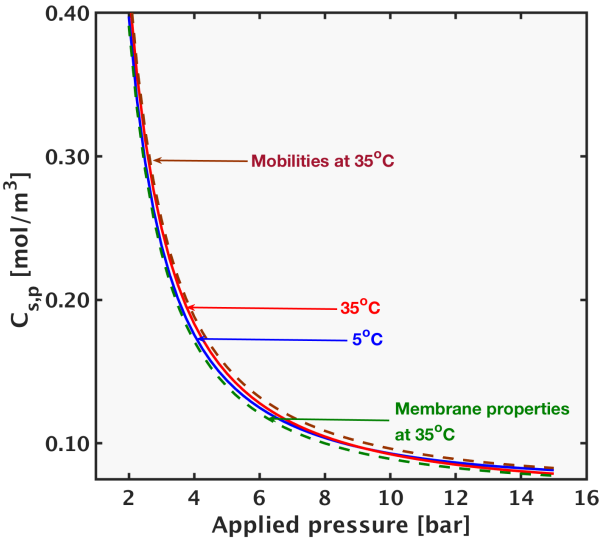

Fig. 3-7a

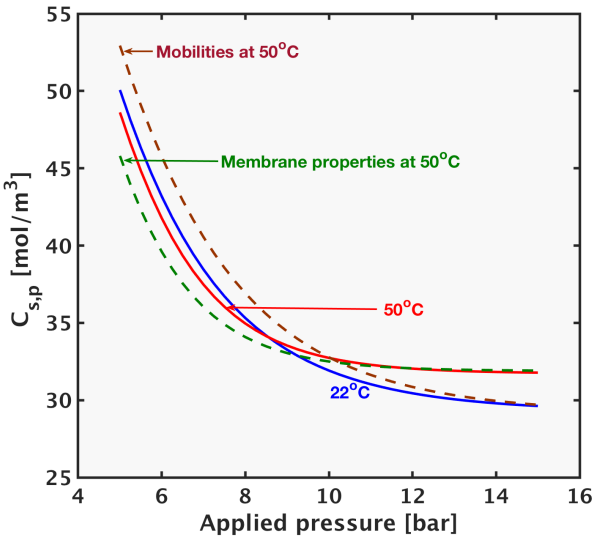

Fig. 3-7b

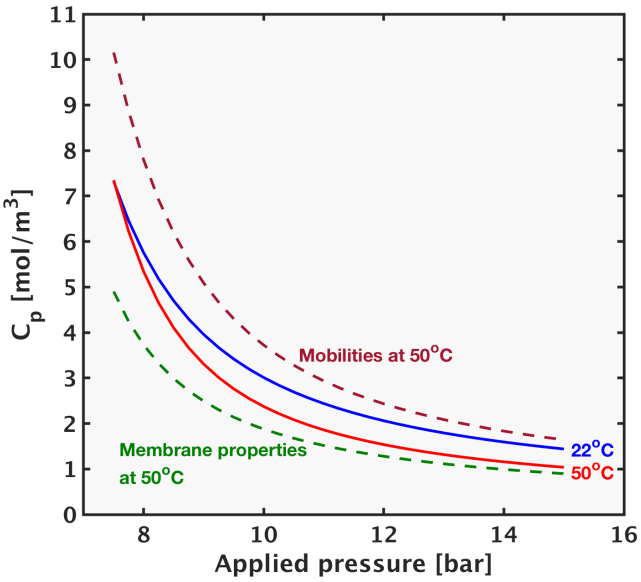

Fig. 3-7c

Fig 3-7. For all data sets (A-C), the net effect of membrane parameters supersedes that of mobilities at increasing applied pressure values.

Figure 3-7. shows the variation of $C_{s,p}$ against applied pressure up to 15 bar. Results by Sharma et al. (51) have been extended to 15 bar using the fitting parameters obtained during validation. For

all data sets, the $\Delta C_{s,p}$ due to mobilities is positive over the entire range of pressure ($C_{s,p}$increase due to $D_{i,\infty}$is larger than the decrease caused by μ_w). Consequently, the line contributed by the mobilities lies above the lower temperature line in all cases. Furthermore, the mobilities line almost merges with the lower temperature line as the applied pressure increases. The deviation of $C_{s,p}$ $(\Delta C_{s,p})$ due to each parameter from the lower temperature values reduces at higher pressure. Accordingly, the reduced contribution of $D_{i,\infty}$ at higher pressure results in the reduced net effect of the mobilities.

3.4.4. Improved selectivity at higher temperature - overcoming unfavorable membrane property changes

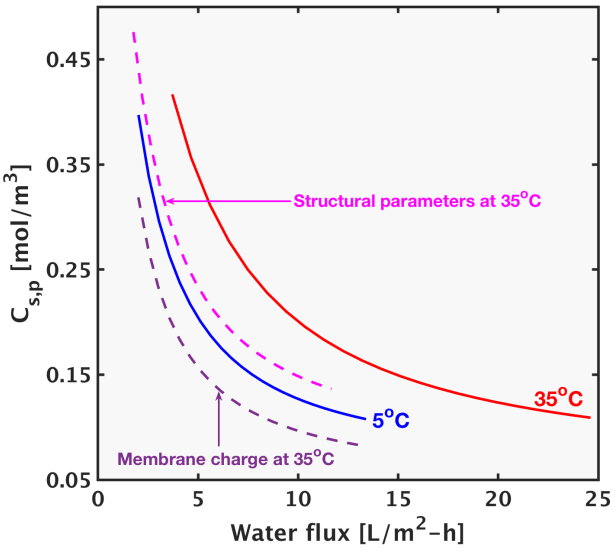

Fig. 3-8a

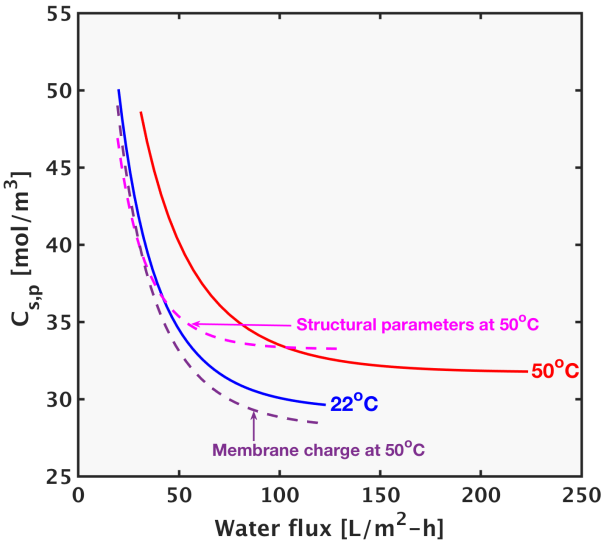

Fig. 3-8b

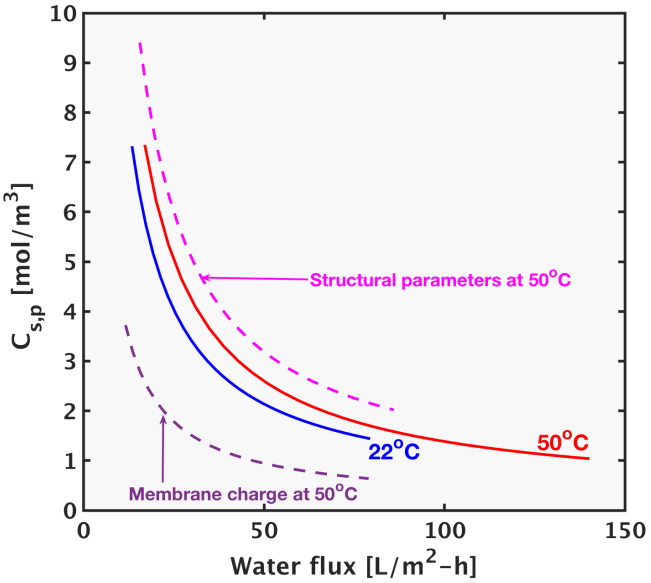

Fig 3-8c

Fig 3-8. Generally, changes in structural properties ($r_{pore}, \Delta x_w, \Delta x_s$) at higher temperature result to increase in permeate concentration (reduced permeate quality), while the increased magnitude of membrane charge lowers permeate concentration. Consequently, membrane construction that reduces propensity to re-structure at higher temperature, as well as membrane material with higher anion-adsorption tendency with increasing temperature would maintain high permeate quality at elevated temperatures.

For all data sets, the temperature-based changes in structural parameters ($r_{pore}, \Delta x_w$ and Δx_s) results to increased $C_{s,p}$ (reduced membrane selectivity), while the increase in negative membrane charge lowers the permeate concentration (enhanced membrane selectivity). These conclusions suggest that membrane-design for higher temperature applications requires focus on reduced structural reorientation and improved anion-adsorption propensity. One method to reduce material restructuring upon temperature increase is the introduction of crystalline that act as 'physical cross-linkers' (i.e. effectively acting as clamps) to minimize polymer-reorientation with temperature change. Such crystalline domains were identified in the Desal5DK membrane Amar et al. (55). Previous literature has reported difference in charge acquiring propensity in solution for different membranes (59). A possible explanation for enhanced ion-adsorption in some membranes is larger

hydrophilicity; better understanding of the involved mechanism is hindered by the proprietary nature of membrane chemistry details.

3.5. Chapter 3 conclusions

Conclusions from this study are enumerated as follows:

1. Membrane parameters each change with temperature increase: pore size, net species path length and membrane charge increase in magnitude.
2. Neither the set of membrane parameters nor mobilities by themselves can account for change in membrane selectivity with temperature variation by themselves.
3. The changes in solvent viscosity and ion diffusivity (the mobilities) decrease and increase permeate concentration with increasing temperature, thereby partially cancelling each-other's effects. The influence of ion diffusivity is dominant and hence the net effect of the mobilities is to increase permeate concentration at higher temperature.
4. At larger pressures, the change in permeate concentration due to each membrane parameter and mobility factor is diminished. Consequently, the net contribution of the two mobilities is superseded by the membrane parameters, which account for almost the total change in permeate concentration due to temperature change.
5. Generally, the membrane structural changes and changes in membrane charge with increase in temperature cause increase and decrease of the permeate concentration respectively. Improved salt retention at higher temperatures can be attained by reducing the membrane material's tendency to restructure, as well as using material with higher anion-adsorption or functional group dissociation propensity at elevated temperatures.

4. A framework to analyze sulfate-chloride selectivity in nanofiltration

4.1. Introduction

Nanofiltration (NF) is a pressure-driven membrane-based separation technology, similar to reverse osmosis (RO). The niche of this technology is for applications requiring high removal efficiency for only multivalent ions. The separation of sodium sulfate from sodium chloride upon nanofiltration treatment of an incoming mixture, is a well-studied application. For convenience, the separation of sodium sulfate from sodium chloride will be referred to as 'fractionation' in this work.

The temperature of industrial effluents that undergo this treatment depends on the source, although NF-treatment is limited by membrane material limits. References (60) and (61) study nanofiltration for fractionation with feed temperatures ranges 32-59^{o}C and 30-40^{o}C respectively, but do not discuss the change of fractionation efficacy due to temperature change. Other sources, such as reference (62) discuss the decrease in rejection of all ions due to increase in feed temperature during NF-based fractionation. Indeed, in academic literature, the change of rejection ratio due to various operating conditions is reported as the primary metric for membrane-based separation. Studies of other NF applications, such as seawater desalination, that depend on the preferential selectivity to multivalent ions also report rejection ratio. However, comparing rejection ratio change due to variation in operating conditions does not provide a direct response to the question: is the nanofiltration membrane more selective to sulfate or chloride ions at a different operating condition? Moreover, as explained in Section 4.4.1, rejection ratio can provide an incorrect answer to this question on some occasions.

In the present work, a performance metric that answers the above question is introduced and its variation with temperature and pressure are analyzed. An analytical framework to explain the observed variations is developed. Applicability to all membrane types used in pressure-driven technologies is the key advantage of the proposed method of analysis. Furthermore, the analysis informs the membrane operator on how to improve selectivity in their system, and identify focus areas for improved membranes for the given application.

Five feed compositions (A-E) representing a range of NaCl-Na_2SO_4 concentration ratios will be considered and the changes in their selectivity metric with temperature, pressure and membrane charge variation will be studied. Fig. 1 describes the molar compositions of solutions A-D, while solution E has the same ratio of salt concentrations as A, but at ten times the total salinity. For compositions A to D, the total equivalents of anions is fixed. For example, in A and D, the anion equivalents are 30+2x15=60 and 12+2x24=60 respectively. Composition E contains ten times the anion equivalents in A-D: 300+2x150=600. In contrast to the other compositions, D has a greater percentage by moles of sodium sulfate than sodium chloride.

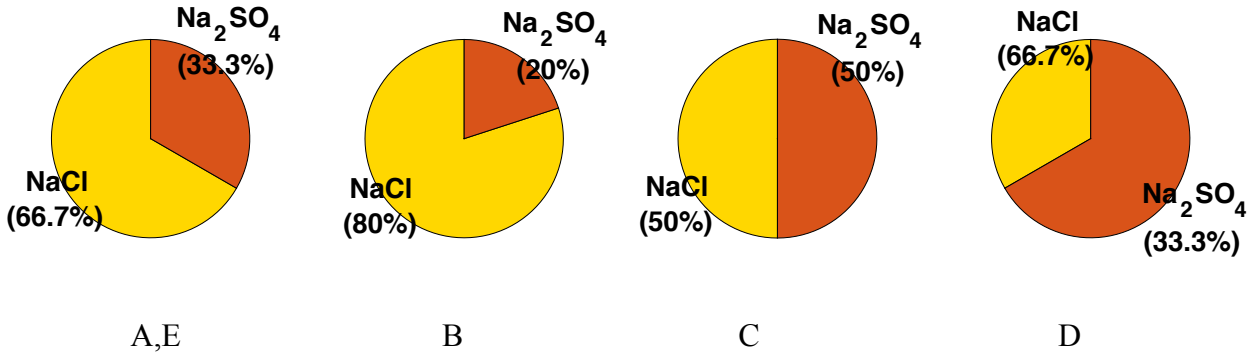

Fig. 4-1. Percentage of moles of NaCl and Na_2SO_4 in each feed composition. Specifically, the compositions of solutions A to E are : 30 mol/m^3 NaCl + 15 mol/m^3 Na_2SO_4 (A), 40 mol/m^3 NaCl + 10 mol/m^3 Na_2SO_4 (B), 20 mol/m^3 NaCl + 20 mol/m^3 Na_2SO_4 (C), 12 mol/m^3 NaCl + 24 mol/m^3 Na_2SO_4 (D) and 300 mol/m^3 NaCl + 150 mol/m^3 Na_2SO_4 (E) respectively.

4.2. Governing equations

4.2.1. Analytical framework

The desired outcome of fractionation is to minimize Na_2SO_4 concentration and maximize NaCl concentration in the permeate stream. Consequently, the primary metric for fractionation performance is defined by Eq. 4-1 in this work:

$$M = \left({}^{C_{p,NaCl}} \Big/ _{C_{p,Na_2SO_4}} \right) \tag{4-1}$$

In pressure driven processes such as NF and RO, the salt (i.e. NaCl or Na_2SO_4) flux and water flux directions are the same, and the following equation holds (25,29,63):

$$C_{p,s} = {}^{J_s} \Big/ _{J_w} \tag{4-2}$$

The above equation holds in case of negative rejection (refer Fig. 4-6c), since in pressure driven processes the transport in the support layer is convection-dominated and back-diffusion is eliminated due to a flat concentration profile in this region.

Using quotient rule of differentiation on Eq. 4-2,

$$\frac{dC_{p,s}}{C_{p,s}} = \frac{dJ_s}{J_s} - \frac{dJ_w}{J_w} \tag{4-3}$$

For each salt, the quantity on the right hand side of Eq. 4-3 can be thought of as a 'competition' between the relative increase in salt flux, J_s, and the relative increase in water flux, J_w.

The derivative of M with respect to a quantity X (temperature, membrane charge or pressure in this paper) is:

$$\frac{dM}{dX} = \frac{d}{dX}\left({C_{p,NaCl}}/{C_{p,Na_2SO_4}}\right) = \frac{C_{p,Na_2SO_4}\dfrac{dC_{p,NaCl}}{dX} - \dfrac{dC_{p,Na_2SO_4}}{dX}C_{p,NaCl}}{C_{p,Na_2SO_4}^2} \tag{4-4}$$

Dividing Eq. 4-4 through by M,

$$\frac{dM}{M} = \frac{dC_{p,NaCl}}{C_{p,NaCl}} - \frac{dC_{p,Na_2SO_4}}{C_{p,Na_2SO_4}} \tag{4-5a}$$

Equation 4-5a gives the relative change in M due to dX. The equation states that when M increases $\left({dM}/{M} > 0\right)$, the relative change in $C_{p,NaCl}$ $\left({dC_{p,NaCl}}/{C_{p,NaCl}}\right)$due to dX is larger than that of C_{p,Na_2SO_4}. Conversely, when M decreases, the relative change in $C_{p,NaCl}$ is smaller than that of C_{p,Na_2SO_4}.

Now using Eq. 4-3 in Eq. 4-5a, and cancelling the ${dJ_w}/{J_w}$ terms for the two salts,

$$\Rightarrow \frac{dM}{M} = \frac{dJ_{NaCl}}{J_{NaCl}} - \frac{dJ_{Na_2SO_4}}{J_{Na_2SO_4}} \tag{4-5b}$$

In summary, an increase in M implies that the relative change in $C_{p,NaCl}$ and J_{NaCl} due to dX are higher than the corresponding values for Na_2SO_4. All inequality signs can be reversed to account for a decrease in M.

Finally, the mass balance on the concentration polarization boundary layer will be used to explain 'breakthrough' in section 4.5.2. As derived in Appendix C for salts containing two ionic species, the electrical potential-gradient component can be replaced by an expression in terms of ion mass

transfer coefficients and diffusivities. Hence, for each salt, the equation effectively reduces to the form shown in Eq. 4-6a. The first term on the right is the convective flux for each salt towards the feed-membrane interface and the second term is the diffusion flux away from this interface.

$$J_s = J_w C_{m,s} - K_s(C_{m,s} - C_{f,s}) \tag{4-6a}$$

Using Eq. 4-2 to replace J_s,

$$J_w C_{p,s} = J_w C_{m,s} - K_s(C_{m,s} - C_{f,s}) \tag{4-6b}$$

4.2.2. Nanofiltration modeling

The current work will use the analytical framework developed in Section 4.2.1 to explain known trends of fractionation performance due to temperature and pressure variation. The trends are mentioned in Section 4.3 based on results from a commercial software and are reproduced (and explained) in Section 4.4 using the widely-used NF model described in our previous work (25,56). This model provides values of salt and water fluxes and concentrations that are necessary for the explanations in Section 4.4. Since the aim of this work is to demonstrate a membrane-independent analytical procedure, details of membrane parameters will not be described here. Phenomena related to temperature-dependence have been accounted for while generating results shown here: ion diffusivity and water viscosity changes are accounted for as shown in our previous work (56), and typical trends of membrane geometry variations are included (22,57,64). Numerical values of membrane pore radius and active layer thickness used are reproduced in Appendix B (further details in reference (65)).

4.3. Known trends on selectivity

In this section, the metric M for various feed conditions are obtained from the commercial software, ROSA created by Dow. As discussed in section 4.4, these trends are also predicted by the NF model used presently. This paper explains these results using the approach developed in section 4.2.1. Fig. 4-2 shows the ratio of M values for the feed composition labeled on the horizontal axis, by that of composition A at reference conditions (22°C and 10 bar applied pressure). For both the NF90 nanofiltration membrane and the SW30 reverse osmosis membrane, common trends (increase or decrease from the reference state) are: M decreases at the higher temperature (the first bar is below 1); compositions B, C and D are in decreasing order of magnitude, with the ratio for B greater than 1; and the M value for E is smaller than A under the same operating conditions.

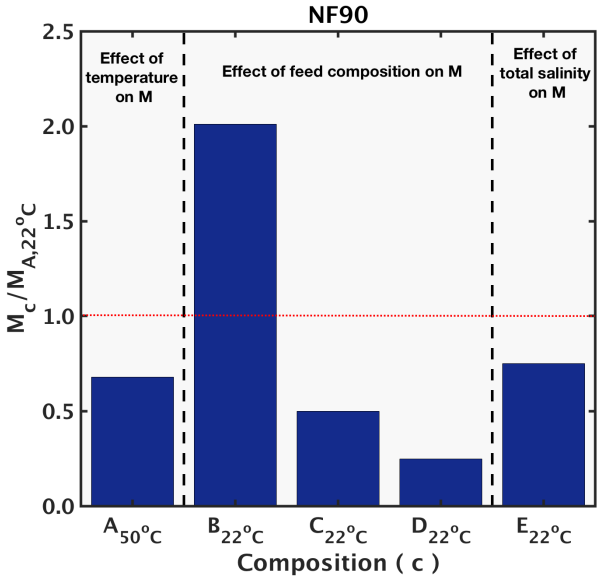

Fig. 4-2a

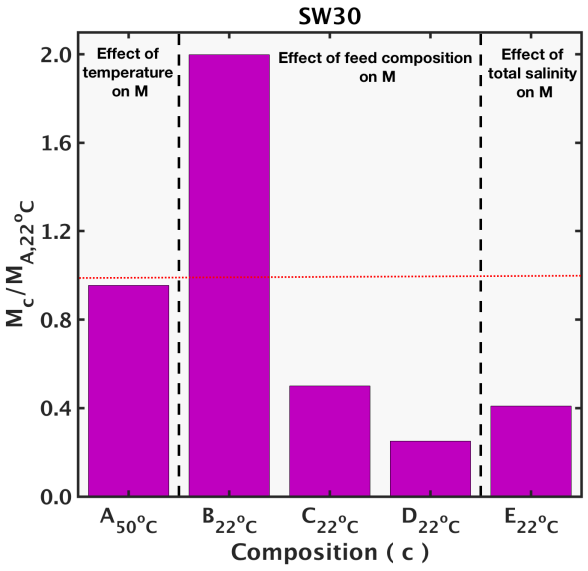

Fig. 4-2b

Fig.4-2: Increase or decrease of M compared to the reference state of composition A (22°C and 10 bar applied pressure) for various feed compositions, from ROSA. For both the nanofiltration (NF90) and reverse osmosis membrane (SW30), M decreases at the higher temperature; values

for compositions B, C and D are in decreasing order of magnitude, with B greater than 1; and the M value for a higher salinity feed (E) is smaller than A under the same operating conditions.

4.4. Results and Discussion

In this section, the variation of M due to change in temperature, pressure and membrane charge will be studied using the NF modeling mentioned in Section 4.2.2. Trends obtained from this modeling match those obtained from ROSA, as described in Section 4.3. However, this modeling approach provides values of salt and water flux necessary for explanations in subsequent sections. Furthermore, the membrane charge and mass transfer coefficient can be independently varied, thereby allowing the study of these effects individually on M. A small patch of membrane is modeled (so that there is no variation of flow conditions along the membrane surface), instead of a full-scale NF unit. Trends obtained from ROSA are qualitatively reproduced using this model and results on salt flux (J_s) and water flux (J_w) obtained can be used to explain these trends. Other than Section 4.5, applied pressure is kept constant at 10 bar.

4.4.1. Why fractionation worsens at higher temperature

As shown earlier, the primary metric for fractionation performance, $M = \left({C_{p,NaCl}}/{C_{p,Na_2SO_4}}\right)$ decreases with an increase in temperature. From Section 4.2.1, the decrease in M occurs when the relative change in permeate concentration of sodium-chloride is less than that of sodium-sulfate. Re-writing Eq. 4-5a and 4-5b for the change in temperature, the conditions can be expressed as:

$$\left(\frac{\Delta C_{p,Na_2SO_{4|22\ to\ 50^oC}}}{C_{p,Na_2SO_{4|22^oC}}} > \frac{\Delta C_{p,NaCl_{|22\ to\ 50^oC}}}{C_{p,NaCl_{|22^oC}}}\right) \tag{4-7a}$$

$$\left(\frac{\Delta J_{Na_2SO_{4|22\ to\ 50^oC}}}{J_{Na_2SO_{4|22^oC}}} > \frac{\Delta J_{NaCl_{|22\ to\ 50^oC}}}{J_{NaCl_{|22^oC}}}\right) \quad \text{(4-7b)}$$

The above conditions are satisfied because the denominators in the ratios for Na_2SO_4 are significantly smaller than those for NaCl. Given that the NF and RO membranes are typically negatively charged, the restricting factor in sodium-sulfate flux is the membrane's repulsion of the sulfate ion. Consequently, the sodium-sulfate flux is small enough to result in a large value of the ratios in Eqs. 4-7a and 4-7b. Solute flux and permeate concentrations for both salts increase with temperature, but the relative changes are different, which ultimately determines the change in M. Figures 3a and b show the relative (percentage) change in permeate concentration and salt flux for sodium chloride and sodium sulfate going from 22 to 50ºC (used in Eqs. 4-7a and 4-7b respectively) at constant applied pressure of 10 bar).

As indicated in section 4.1, the rejection ratio (defined as $\left(1 - {C_{f,s}}/{C_{p,s}}\right)$ for NF (7,22,46)) can mislead the membrane operator to conclude that selective removal of sodium sulfate is higher at the higher temperature. Referring to Fig. 4-3d, the decrease in rejection ratio for Na_2SO_4 is much smaller (less than 1%) than that of NaCl (around 20%) from 22 to 50ºC. The small drop in rejection ratio for Na_2SO_4 seems to indicate that its permeate concentration barely changed with temperature. However, the permeate concentration of Na_2SO_4 increased by several factors more than NaCl as shown in Fig. 4-3a.

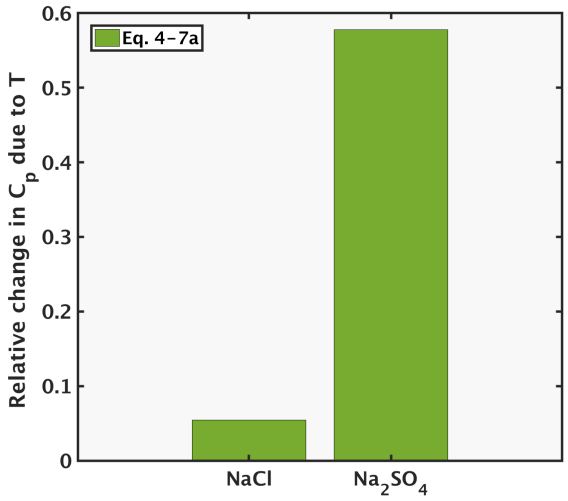

Fig. 4-3a.

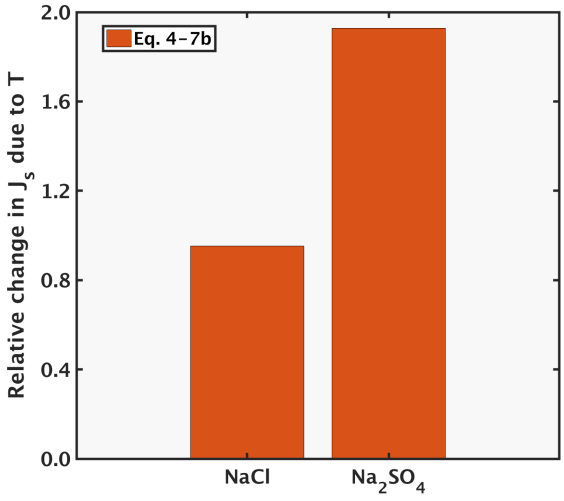

Fig. 4-3b.

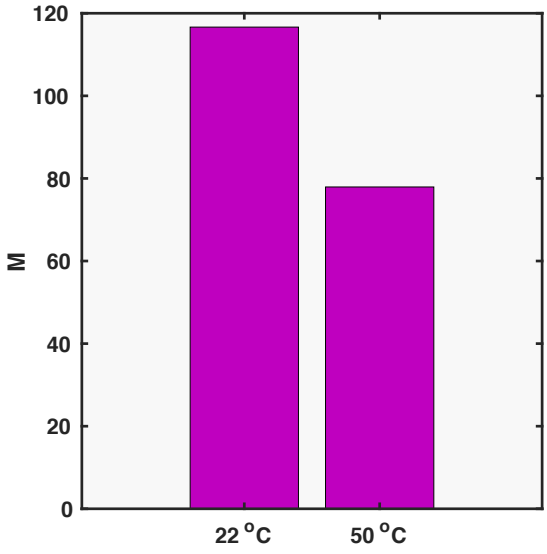

Fig. 4-3c

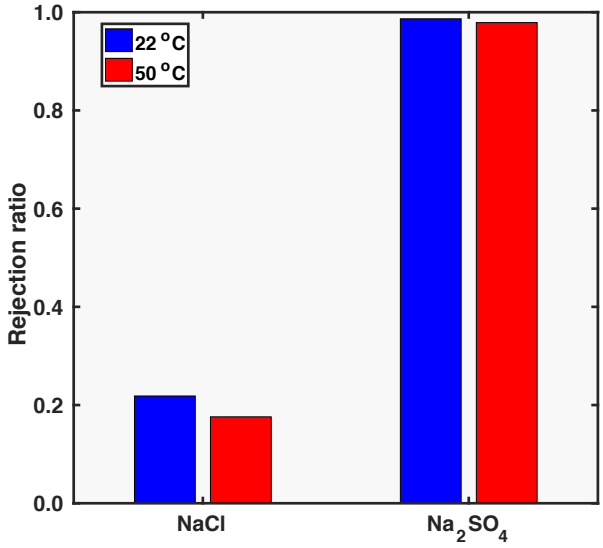

Fig. 4-3d

Fig. 4-3: The selectivity metric, M, decreases at the higher temperature. Figures 4-3a and 4-3b show the relative (percentage) increase in permeate concentration and salt flux $\left(\frac{\Delta C_{p,s}}{C_{p,s}}\Big|_{22\ to\ 50^{oC}}\right)$ and $\left(\frac{\Delta J_s}{J_s}\Big|_{22\ to\ 50^{oC}}\right)$ respectively (used in terms in Eqs. 4-7a and 4-7b) and depict the larger relative increase in sodium-sulfate permeate concentration and solute flux, compared to those of

sodium-chloride. The larger magnitudes of relative change for sodium sulfate result in the decrease in M at the higher temperature, as shown in Fig 4-3c. Figure 4-3d shows the rejection ratio $\left(1 - {C_{f,s}}/{C_{p,s}}\right)$ for the two salts at both temperatures. Results in Fig. 4-3 are for feed composition A but similar trends hold for the others.

4.4.2. Negatively charged membranes are advantageous for fractionation

Nanofiltration membranes develop a charge in solution, determined by feed solution pH and ion adsorption propensity from the feed solution. As shown in Fig. 4-4a, the fractionation metric, M, is higher when the membrane is negatively charged under the operating conditions. The improved selectivity between NaCl and Na_2SO_4 with negatively charged membranes is due to the stronger response of the bivalent SO_4^{2-} ion to the increased Donnan exclusion, compared to the monovalent Cl^- ion. Figures 4-4b and c show that the flux of both ions reduces going from a neutral membrane charge ($C_X = 0\ mol/m^3$) to a negative charge value ($C_X = -|C_X|\ mol/m^3$). However, the relative decrease in solute flux is higher for sodium-sulfate.

Re-writing Eq. 4-5b to reflect these changes,

$$\frac{\left(J_{Na_2SO_4\,|C_{X=-|C_X|}} - J_{Na_2SO_4\,|C_{X=0}}\right)}{J_{Na_2SO_4\,|C_{X=0}}} < \frac{\left(J_{NaCl\,|C_{X=-|C_X|}} - J_{NaCl\,|C_{X=0}}\right)}{J_{NaCl\,|C_{X=0}}} \tag{4-8}$$

Hence, the selectivity to sodium-sulfate measured by the M value increases moving to more negatively charged membranes. The above explanation is similar for the positive membrane

charge, where sulfate ions still experience stronger exclusion due to their larger size. Accordingly, the change in M from $C_X = 0$ to $+|C_X|\ mol/m^3$ is less significant compared to that from $C_X = 0$ to $-|C_X|\ mol/m^3$.

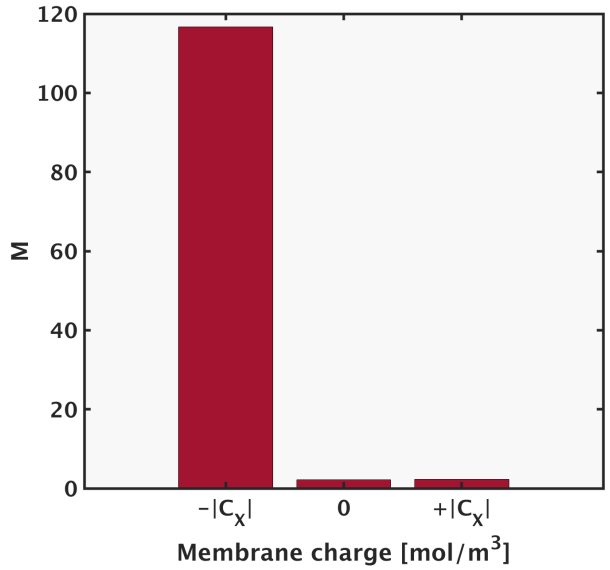

Fig. 4-4a

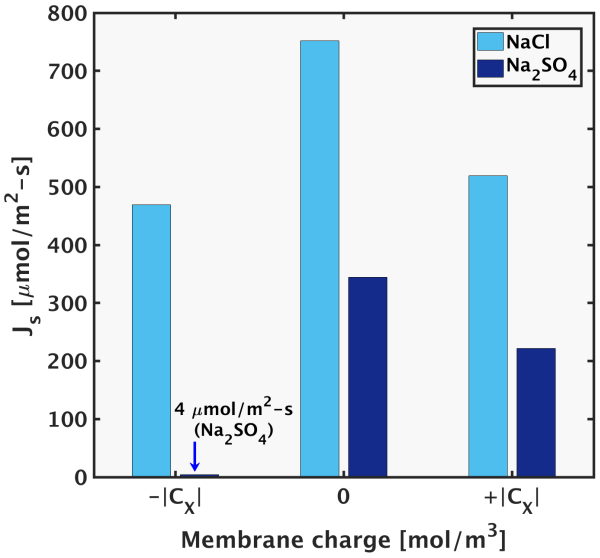

Fig. 4-4b

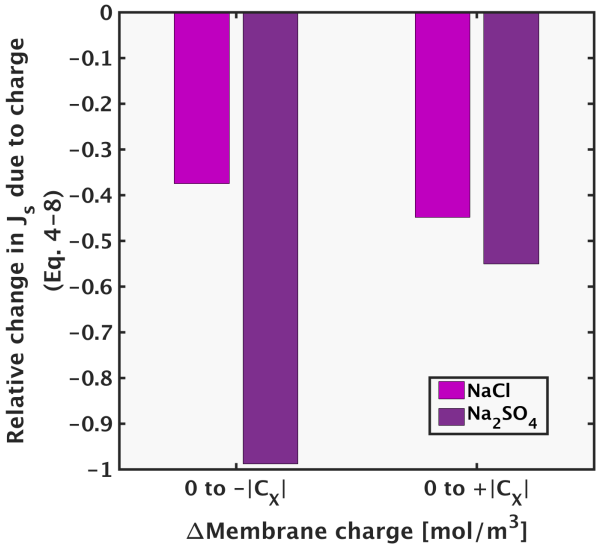

Fig. 4-4c

Fig. 4-4. Negatively charged membranes have better selectivity to sodium-sulfate than neutrally charged or positively charged membranes, as shown by the M values in Fig. 4-4a. This enhanced selectivity is due to the stronger Donnan exclusion of sulfate ions, resulting in a more significant relative decrease in its solute flux compared to sodium-chloride.

4.4.3. Observations on *M* at different compositions

In this section, the four feed compositions, A, B, C and D shown previously in in Fig. 4-1 will be compared. All feed compositions considered in this section contain the same overall equivalents of anionic species, as explained in Section 4.1. As shown in Fig. 4-5a, M decreases in the order of the ratio of feed concentrations of NaCl by Na_2SO_4 $\left({C_{f,NaCl}}/{C_{f,Na_2SO_4}}\right)$. For all cases, however, $M = \left({C_{p,NaCl}}/{C_{p,Na_2SO_4}}\right)$ is larger than 1 (including composition D where the feed molar concentration of Na_2SO_4 is higher than NaCl), since in a negatively charged membrane, the Donnan exclusion will affect the SO_4^{2-} ions in sodium sulfate more strongly. Since the same temperature-dependent parameters are used for all compositions, $\frac{C_{p,NaCl|50^oC}}{C_{p,NaCl,22^oC}}$ and $\frac{C_{p,Na_2SO_4|50^oC}}{C_{p,Na_2SO_4,22^oC}}$ are equal for all compositions. Hence, the following expression is equal for all compositions (Fig. 4-5b):

$$\left(\frac{C_{p,NaCl|50^oC}}{C_{p,NaCl,22^oC}}\right) \Bigg/ \frac{C_{p,Na_2SO_4|50^oC}}{C_{p,Na_2SO_4,22^oC}} = \frac{M_{50^oC}}{M_{22^oC}} \tag{4-9}$$

To summarize, for feed compositions that differ only in the ratio of chloride to sulfate charge equivalents in the feed, (total anionic charge equivalents in the feed is the same for compositions A, B, C and D, ref. Section 4.1) fractionation is easier for those with less sodium sulfate. For all such solutions, selective removal of sulfate is less effective at higher temperatures and decreases by the same extent.

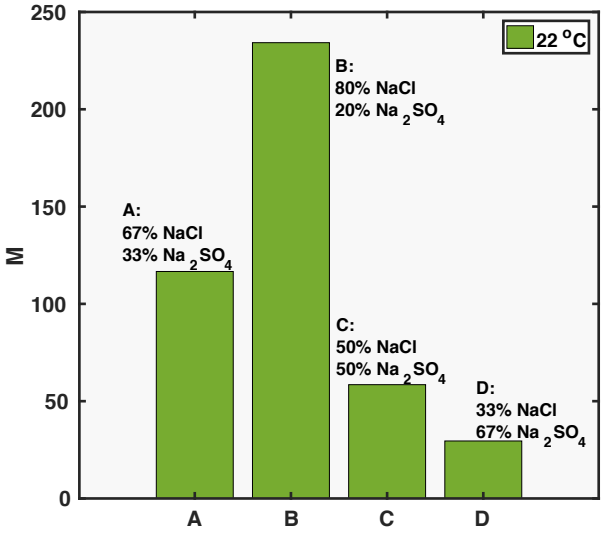

Fig. 4-5a

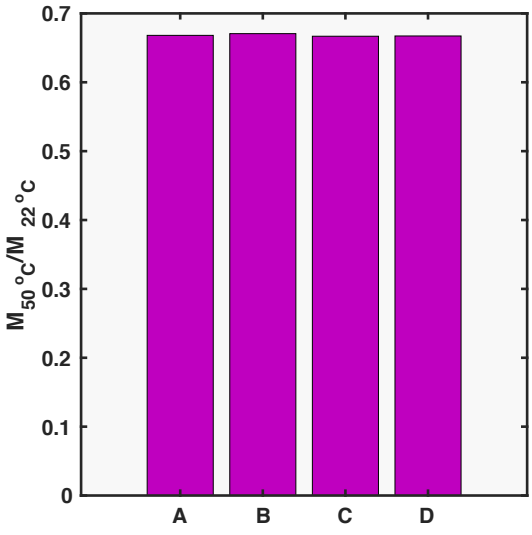

Fig. 4-5b

Fig. 4-5. The ratio of NaCl by Na_2SO_4 concentration in the feed (decreasing as B,A,C,D) is reflected in the order of decreasing M values. M for all feed compositions decreases by the same factor at the higher temperature.

4.4.4. Fractionation of higher TDS solutions - reduced *M* and negative Cl- rejection

In this section, performance metrics for feed compositions A and E (low and high total salinity) will be compared. As reported in previous literature, the rejection ratio of any salt is lower at a higher concentration, attributed to the lower Donnan exclusion by the membrane (3,31,59). When the feed concentration of a salt is increased, the number of ions available to cross the membrane per unit time, i.e., ion flux, is increased. To allow the increased passage of membrane co-ions (ions with the same charge as the membrane), the Donnan potential (and hence Donnan exclusion) decreases in magnitude. Since sulfate ions have higher negative charge than chloride ions, the decrease in Donnan exclusion allows the increase in $J_{Na_2SO_4}$ to be several times larger than that of

J_{NaCl}. The relative increase in salt flux (Eq. 4-5b) is higher for sodium sulfate than sodium chloride (from composition A to E, the feed concentration of both salts increase by 10 times, and the salt flux increased by 12 times and 305 times for NaCl and Na_2SO_4 respectively). Consequently, the metric M reduces at the higher concentration.

A further consequence of the significant increase in sodium sulfate flux is that $\Delta J_{Na_2SO_4|22\ to\ 50^oC} \Big/ J_{Na_2SO_4|22^oC}$ is lower for the higher concentration mixture (the denominator is significantly larger than lower concentration case). Hence, the decrease in M, $\left(dM \Big/ M\right)$, is lower for the higher salinity case. Mathematically expressed by re-writing Eq. 4-5b (also shown in Fig. 4-6b):

$$\frac{dJ_{Na_2SO_4}}{J_{Na_2SO_4}} - \frac{dJ_{NaCl}}{J_{NaCl}}\bigg|_{E,22\ to\ 50^oC} < \frac{dJ_{Na_2SO_4}}{J_{Na_2SO_4}} - \frac{dJ_{NaCl}}{J_{NaCl}}\bigg|_{A,22\ to\ 50^oC} \tag{4-10a}$$

$$\Rightarrow \frac{dM}{M}\bigg|_{E,22\ to\ 50^oC} < \frac{dM}{M}\bigg|_{A,22\ to\ 50^oC} \tag{4-10b}$$

Several studies have reported negative rejection ratio in a ternary mixture of ions (26,66). As mentioned earlier, the rejection ratio decreases when the total salinity increases. Hence, the possibility of negative rejection is enhanced at higher salinity. In a negatively charged membrane (the case for most polyamide NF membranes), the rejection ratio of NaCl is smaller than that of Na_2SO_4. As shown in Fig. 4-6c, the reduction of rejection ratio at the higher salinity is large enough so that the value for NaCl becomes negative (compare Fig. 4-3d for the lower salinity case).

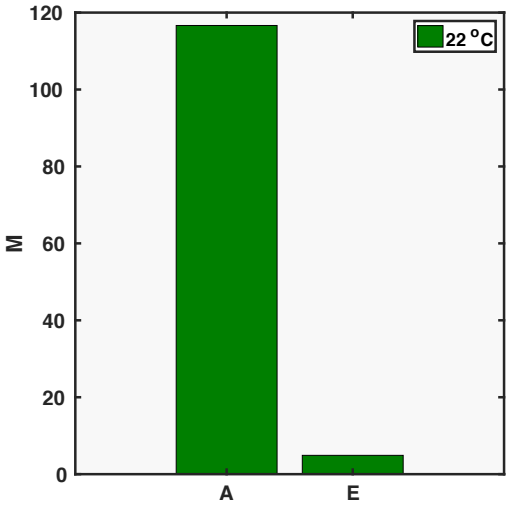

Fig. 4-6a

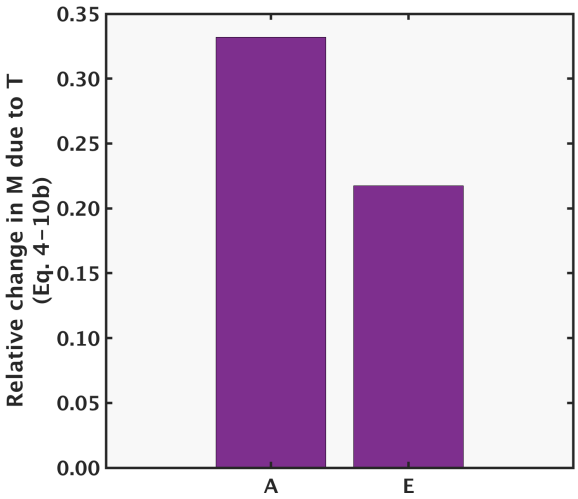

Fig 4-6b

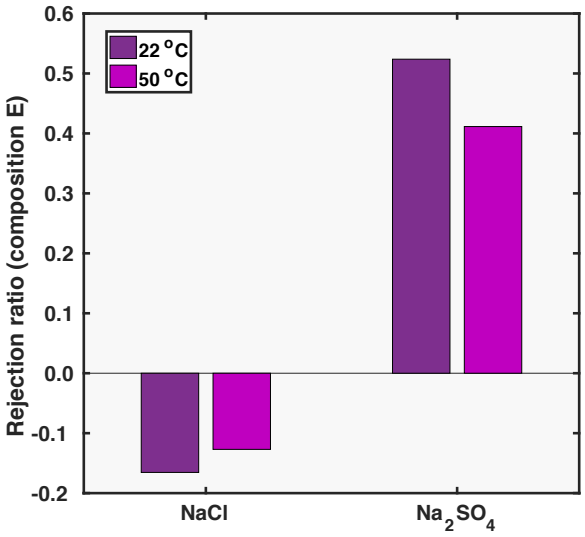

Fig. 4-6c

Fig. 4-6 The *M* value for the higher salinity composition is lower due to decreased Donnan exclusion, which affects sulfate ions more significantly. Rejection ratio of both salts decreases at higher feed salinity, and can result to negative rejection for sodium-chloride.

4.4.5. Response of M to pressure variation

4.4.5.1. Change in Selectivity

The framework developed above can be used to explain the pressure-dependence of metric M. As shown in Fig. 4-7a, M decreased at the higher applied pressure of 20 bar, compared to values at 10 bar for both compositions A and E. Furthermore, the decrease is less significant for the higher salinity composition E. The lower M at higher pressure is explained similarly to the effect of increased temperature on both compositions (section 4.4.1.): relative increase in $J_{Na_2SO_4}$ due to pressure increase is larger than that for J_{NaCl} due to the smaller denominator in the expression for $\Delta J_s / J_s$.

As explained in the previous section, M is smaller for a higher salinity mixture under given operating conditions due to reduced Donnan exclusion. Hence, the denominator in the expression for relative change in solute flux $\Delta J_{Na_2SO_4|10\ to\ 20\ bar} / J_{Na_2SO_4|10\ bar}$ is larger at higher salinity (causing the ratio to be smaller):

$$\frac{dJ_{Na_2SO_4}}{J_{Na_2SO_4}} - \frac{dJ_{NaCl}}{J_{NaCl}}\bigg|_{E,10\ to\ 20\ bar} < \frac{dJ_{Na_2SO_4}}{J_{Na_2SO_4}} - \frac{dJ_{NaCl}}{J_{NaCl}}\bigg|_{A,10\ to\ 20\ bar} \tag{4-11a}$$

$$\Rightarrow \frac{dM}{M}\bigg|_{E,10\ to\ 20\ bar} < \frac{dM}{M}\bigg|_{A,10\ to\ 20\ bar} \tag{4-11b}$$

The reduced value of the ratio $\Delta J_{Na_2SO_4|10\ to\ 20\ bar} / J_{Na_2SO_4|10\ bar}$ at higher concentration can extend to the case that $\Delta J_{Na_2SO_4|10\ to\ 20\ bar} / J_{Na_2SO_4|10\ bar} < \Delta J_{NaCl|10\ to\ 20\ bar} / J_{NaCl|10\ bar}$, in which case Mincreases at higher pressure.

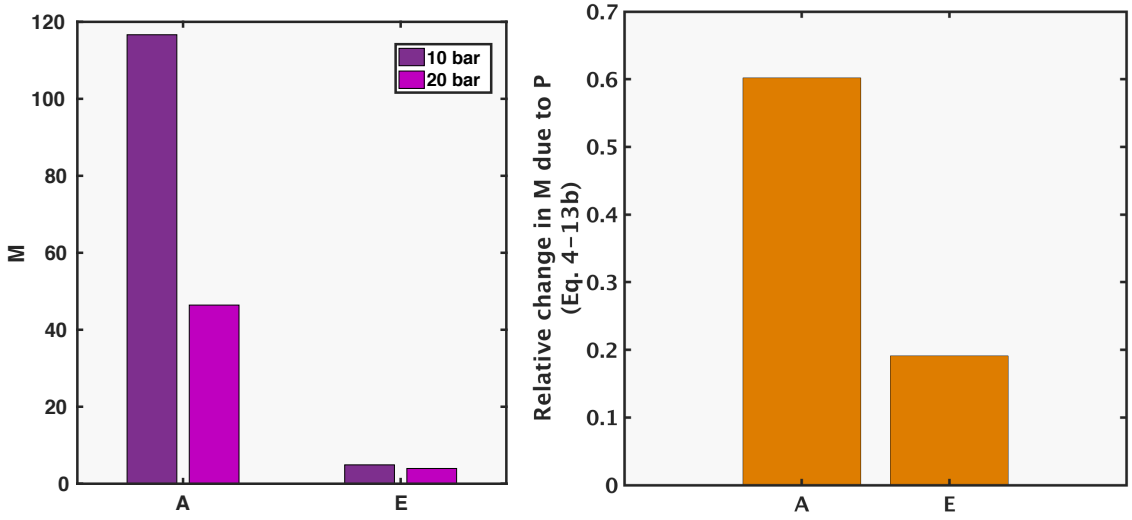

Fig 4-7a **Fig 4-7b**

Fig. **4-7** M values are smaller for the higher salinity composition, and the relative change with pressure increase is lower.

4.4.5.2. The concept of 'Breakthrough'

When concentration polarization (CP) exists in the system, rejection ratio will decrease beyond a particular pressure (67,68). The point at which this reduction occurs is referred to as 'breakthrough' in this work. A mathematical description for why this occurs and the implications on the change of M with pressure change are discussed in this section.

Equation 4-8b can be written in words to show the terms that contribute to salt build-up ($J_w C_{m,s}$)or reduce salt build-up ($-K_{eff}(C_{m,s} - C_{f,s})$) in the CP boundary layer. These two components can be referred to as 'towards membrane' (TM) or 'towards feed' (TF) respectively:

$$J_w C_{p,s} = towards\ membrane\ (TM) + towards\ feed\ (TF) \tag{4-12a}$$

$$\Rightarrow C_{p,s} = \frac{(TM)}{J_w} + \frac{(TF)}{J_w} \tag{4-12b}$$

Equation 4-12b can be written for any pressure P, and a pressure value a slightly lower than P ($= P - \delta P$). The subtraction of the latter equation from the first can be written as:

$$\Delta C_{p,s}\big|_{(P-\delta P)to\ P} = \Delta\frac{(TM)}{J_w}\bigg|_{(P-\delta P)to\ P} + \Delta\frac{(TF)}{J_w}\bigg|_{(P-\delta P)to\ P} \tag{4-12c}$$

Breakthrough occurs for each salt when the following condition is satisfied i.e. TM grows faster than TF (depicted in Figs. 4-8a and 4-8b):

$$\left|\frac{\Delta\frac{(TM)}{J_w}}{\Delta\frac{(TF)}{J_w}}\right| > 1 \tag{4-12d}$$

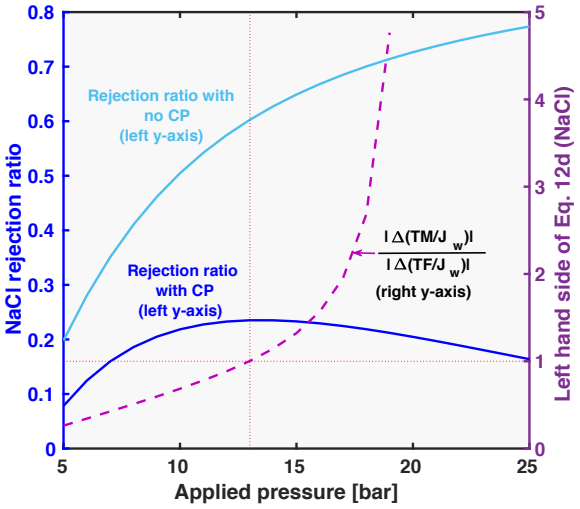

Fig 4-8a

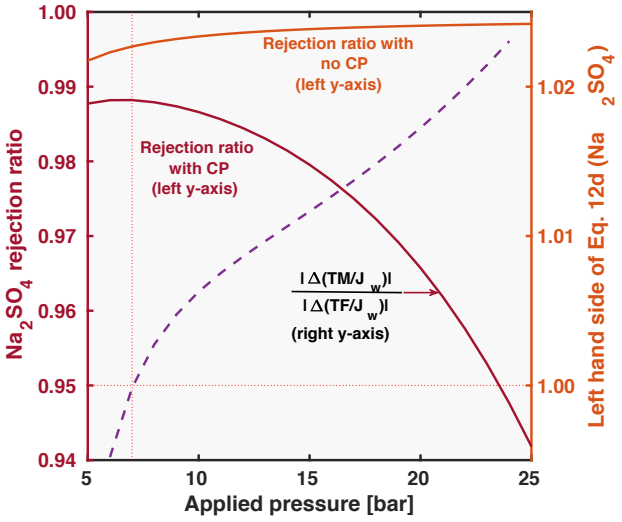

Fig 4-8b

Fig. 4-8 When concentration polarization exists in a system, the rejection ratio (left y-axis) decreases beyond a certain pressure. At this pressure, the convective transport towards the membrane grows faster than the diffusive salt flux back to the feed (the ratio on the left-hand side of Eq. 4-12d becomes > 1). The breakthrough point for both salts (when concentration

polarization (CP) exists in the system) is shown at the point where rejection ratio starts dropping and the left-hand side of Eq. 4-12d (dashed lines) rises above 1.

Figure 4-8 also shows that when CP is not present, the rejection ratio continues to increase with pressure (and will at some point reach a plateau). For the pressure range plotted, the continuing increase of rejection ratio indicates a decrease in permeate concentration with pressure. Consequently, the relative change in $C_{p,s}$ is negative for both salts in this regime (Fig. 4-9a). Furthermore, the magnitude of relative decrease in M without CP is smaller than if breakthrough occurs, as shown in Fig. 4-9b. These findings indicate that in an industrial system, if the decrease in M due to pressure increase is to be minimized, increasing flow rate (or other steps to increase mass transfer coefficient K_s) should be undertaken.

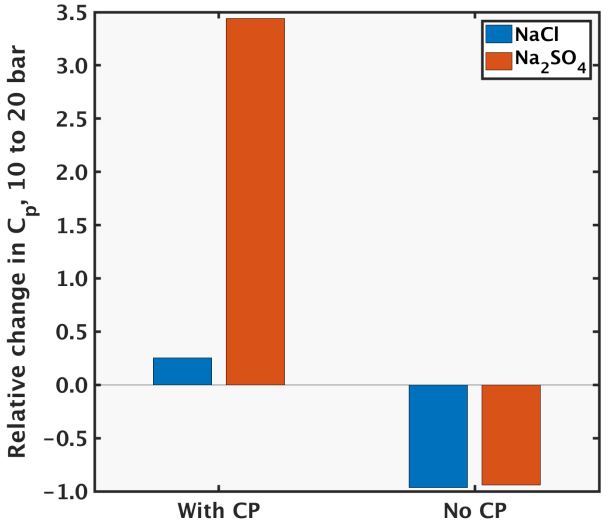

Fig 4-9a

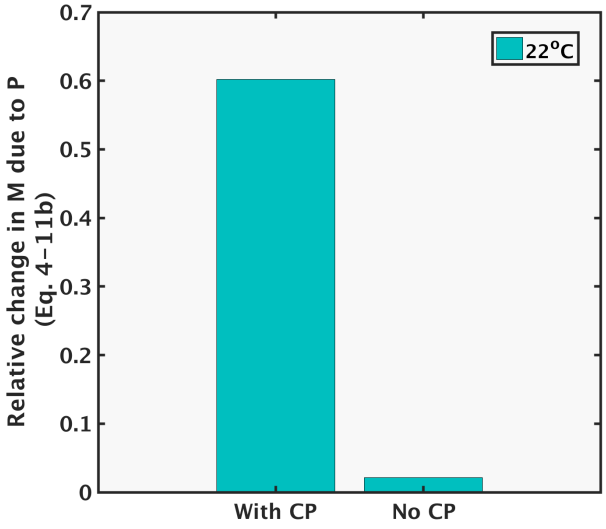

Fig 4-9b

Fig. 4-9 The increasing rejection ratio with applied pressure when there is no CP indicates that the relative change in permeate concentration is negative for this regime. When CP is present in the system and 'breakthrough' occurs, the permeate concentration increases. The relative decrease in selectivity metric M is lower when there is no CP, so taking measures to increase mass transfer coefficient will improve membrane selectivity.

4.5. Chapter 4 conclusions

The framework to analyze membrane selectivity applied to explain the effect of temperature, pressure, feed composition and membrane charge provides the following insights:

1. The ability of a membrane to selectively remove multivalent ions over monovalent ions reduces at higher temperature.
2. Membranes that acquire negative charge in solution are best for sulfate-chloride fractionation. Consequently, for higher temperature applications, operating conditions and membrane characteristics that favor a negative acquired charge are desirable. For example, higher operating feed pH, membranes that exhibit enhanced anion-adsorption capacity or functional-group dissociation to enhance negative membrane charge, are preferred at higher temperature.
3. The desired membrane properties at higher temperature also depends on the feed composition. For example, fractionation efficiency for solutions with higher TDS will not decrease as drastically at higher temperature, hence the requirement of increasing negative membrane charge will not be as significant, compared to applications involving lower TDS feed.
4. Selectivity reduces at higher operating pressure, especially if concentration polarization (CP) is present in the system. Consequently, steps to increase mass transfer coefficient in the system, such as increased feed flow rate and improved feed spacers are desirable. Furthermore, controlling the 'build-up' of the CP layer, by reducing permeate flux will also improve selectivity.

5. Generalized pore flow model for forward osmosis, reverse osmosis, and nanofiltration

5.1. Introduction

In recent literature, reverse osmosis (RO) and forward osmosis (FO) are commonly modeled by the solution–diffusion (SD) theory (13–16). However, over the years, several authors have proposed several different models, especially for RO and nanofiltration (NF) (3,37,43,69–71). These models are broadly classified as either SD or pore flow (72). The major difference between these two approaches is the lack of convective solute transport in the SD model, i.e., the SD model considers no solute motion as a result of being carried by water flux through the membrane (73). Because SD is both mathematically simple and commonly used, its use is widespread. However, the SD model has limitations. For example, SD neglects solute convection, and it is impossible to capture potential effects of convective solute transport using this model. In the current study, a general model that works for NF as well as dense membranes (RO and FO) is developed. This model includes all possible modes of transport and is validated against experimental data for FO and RO. The governing equations shown have been widely implemented for NF (3,25,29) and in this work they are extended to use in RO and FO.

5.1.1. Traditional pore flow versus traditional solution–diffusion (SD)

Table 5-1 delineates the differences between the traditional pore flow and SD models. The traditional SD model denotes the model discussed by Wijmans and Baker (72), which is the most commonly used form of the SD model (13–16).

Table 5-1: Comparison between the traditional pore flow and solution–diffusion (SD) models

Characteristic	Traditional pore flow	Traditional solution–diffusion
Primary difference: inclusion of convective solute transport	Yes	No
Nature of modeling parameters	Physical membrane characteristics (e.g., pore radius, etc.)	Phenomenological coefficients that quantify individual fluxes (e.g., solute permeability)
Factors determining solute entry into membrane	Exclusion (based on size, charge, etc.)	Sorption coefficient
Mode of water entry into membrane	Flow	Sorption

A more sophisticated SD model is discussed by Yaroschuk et al. (73,74) (cf. Section 5.1.3) in which the transport of solute species through the membrane occurs by diffusion and electromigration and the phenomenological coefficients can provide information on the extent of exclusion by means of mechanisms other than sorption.

As mentioned previously, the SD model is the most prevalent model for RO and FO. This wide use is partly the result of its inherent simplicity and partly because it provides reasonably good fits to experimental data (15,72). Indeed, as stated by Wijmans and Baker (72), the solution diffusion model has been considered since the 1980s to be the most accurate theory for membrane processes that use dense membranes such as RO. Furthermore, Wijmans and Baker prescribe the pore diameter lower limit for the applicability of the pore flow model to be ~0.5 nm, implying that the usefulness of the pore flow model disappears for membranes tighter than NF membranes (such as those in RO).

Nevertheless, pore flow models of RO have been introduced and validated in several cases (69,75,76). These models fall within the purview of the traditional pore flow models described in Table 5-1. The pore flow model discussed by Wijmans and Baker (72) (initially introduced by Okada and Matsuura (77)) was only the precursor to several more sophisticated models. The simple model introduced by Okada and Matsuura considered steric exclusion to be the sole rejection mechanism, assumed that solvent transport is governed by the Darcy equation, and approximated solute transport by a simple expression using a solute transport parameter. Models that included both the diffusive and convective modes of solute transport and solute-membrane interaction potentials were introduced by many authors. Those introduced by Anderson et al. (35,36), Matsuura and Sourirajan's Surface Force-Pore Flow (SF-PF) (75) and Mehdizadeh and Dickson's Modified Surface Force-Pore Flow (MD SF-PF) (78) are among the best-known models that emerged.

5.1.2. The evolution of sophisticated pore flow models for electrolytes

Subsequently, pore flow models for electrolyte transport that used the Extended Nernst-Planck (ENP) equation for solute transport were introduced (3,37,70). The Extended Nernst-Planck equation adds an electromigrative term to the convective and diffusive terms that were already accounted for in the models of Anderson (35,36), the SF-PF (75) and MD SF-PF models (78). The Space Charge (SC) model (79) and the Teorell-Meyer-Sievers (TMS) (37) model were two such models. Tsuru et al. (70) were the first to use the TMS model for reverse osmosis. The Donnan Steric Pore Model (DSPM) (31,80) and its variant, the Donnan Steric Pore Model with Dielectric Exclusion (DSPM-DE) were introduced for NF (the two most well-known versions of the DSPM-DE were that by Geraldes et al. (29), considering only the Born solvation effect, and that by Bandini et al. (30), considering primarily the effect of image charges). The DSPM is very similar

to the TMS model, but also considers steric (size-based) exclusion at the pore entry in addition to the Donnan (charge-based) exclusion effect included in the TMS model. The DSPM-DE includes yet another exclusion mechanism: dielectric exclusion (29).

5.1.3. Generalized SD for loose and dense membranes

In more recent years, Yarhoshchuk et al. (73,74) have implemented a model that is mathematically simpler than the aforementioned models for NF (the DSPM and the DSPM-DE), and can be used for both NF and RO. Yarhoshchuk et al. use phenomenological permeation coefficients that account for both the resistance to motion within the membrane and the exclusion effects at the pore openings. This model is derived from the Nernst-Planck equation and includes only the electromigrative and diffusive terms, effectively making it an SD model. Yaroshchuk et al. (73) were able to validate this solution diffusion model for even a loose NF membrane, the NF270 membrane, thus establishing that high solute permeability is not necessarily associated with convective coupling.

5.1.4. Free volume elements in membranes

Despite the success of the SD model in simulating RO, FO, and NF, evidence supports the occurrence of pore flow in dense membranes such as RO membranes: pores (free volumes) have been detected in RO membranes (11,12). Researchers at Toray Industries published measurements of free-volume diameter in their RO membranes using positron-annihilation lifetime spectroscopy (PALS); they also found that increasing membrane pore size correlated with decreasing rejection of boron (in the form of boric acid) (12). Other researchers have also conducted PALS on commercial RO and NF membranes and have detected free volume elements (11,81). Recent molecular dynamics simulations have considered free voids in reverse osmosis membranes (82).

The presence of free volume elements in membranes is not surprising; a perfectly dense material is an idealization. However, the permanence of free voids in dense membranes is the subject of some debate. Wijmans and Baker (72) conjectured that the presence of pores and hence the validity of the pore flow mechanism in membranes is based on the "relative permanence" of the free volume elements/pores. They state that the free voids in RO membranes are merely statistical fluctuations which appear and disappear on a time scale similar to that of the motion of species within the membrane and hence they cannot be considered as discrete pores. However, as mentioned previously, the authors of References (11,12) have stated that there is a direct correlation between free volume radius and permeability of water and solutes in RO membranes, which demonstrates that the free voids play an important role in determining RO membrane performance. The work of Paul (83), in addition to a revised version of Wijmans' SD model, considers the Maxwell-Stefan model for RO. Paul discusses the possibility of frictional coupling of solute and solvent fluxes and concludes that while such coupling is possible, the observable effect on experimental measurements (of rejection ratio) in RO are likely to be negligible in most cases. Moreover, Fujioka et al. (11) showed, using PALS measurements, that the free volume radius has only a small difference among NF, low pressure RO and seawater RO membranes. This finding conflicts with the thought that NF membranes are porous (3) and RO membranes are non-porous (72).

In some cases, the failure of the SD model to agree with experimental data can be explained only by the presence of convective flow within the membrane (84,85). Indeed, some authors have shown that many RO membranes cannot be modeled accurately by the SD approach due to imperfections in the membrane active layer, the occurrence of convective flow in the active layer,

and various solute-solvent-membrane interactions that are not captured by the SD theory (69,70,84,85).

5.1.5. Focus of the present work

In the present work convective transport of solutes, in addition to diffusion and electromigration, is incorporated into a general model of transport through RO and FO membranes. Size-based (steric) and charge-based (Donnan) exclusion mechanisms are included. All transport modes within the membrane are modified according to the hindered transport theory to account for the similar size of water and solutes relative to the pores. The incorporation of convective transport, size-based exclusion, and hindered transport theory qualify the current model as a pore flow model. The approach taken in this work is to try, at first, to validate the general model that includes all possible modes of transport with RO and FO experimental data from multiple sources. If the model fails to match experiments, the model will be modified based on physical insights on solute transport in RO and FO in literature until the model predictions match experimental data.

As will be discussed, the findings indicate that the RO model agrees with experimental data in the unaltered form, even better than the SD model. However, the current model cannot agree with experimental data for FO unless the convective mode of solute transport is removed. This conclusion implies that the transport of solutes through the membrane in FO mode is diffusion-dominated, thereby requiring the modeling approach to reduce to SD. The difference in the RO and FO modeling approaches can be explained by the difference in states of pressurization of the membrane. In the RO mode, the application of pressure may lead to a significant convective coupling effect, such that the solute is ‘carried’ by the water flow. This effect is absent in FO. Another possible explanation is that the convective coupling in FO may be present, but would be more accurately accounted for by a more sophisticated approach such as the Maxwell-Stefan

model, which accounts for each type of inter-species interaction individually. Moreover, our conclusion establishes a connection between the concepts of diffusion-dominated transport with the detection of free volume in membranes. As explained in Table 5-1, by definition, pore flow models are traditionally considered to include the convective mode of transport. Our conclusion is that a membrane can contain pores (free volume) and thus solute selectivity can be due to a combination of steric and charge-based effects while the convective coupling effect is absent, as found in the FO mode. From the perspective of modeling convenience, the current approach is advantageous over the traditional SD model in two ways: first, the model gives individual solute fluxes of each ion present. Second, the number of fitting parameters required by the model does not depend upon the number of constituents in solution, but rather on the physical characteristics of the membrane.

5.2. Governing equations

Figures 5-1a and 5-1b show the governing equations on schematic diagrams of an asymmetric polymeric membrane in pressurized and unpressurized modes, respectively. Since the governing equations are nonlinear ordinary differential equations, numerical implementation was done by linearization and discretization in a manner similar to that in Ref. (29). The solution was obtained by Newton's method and was implemented using MATLAB v2015b.

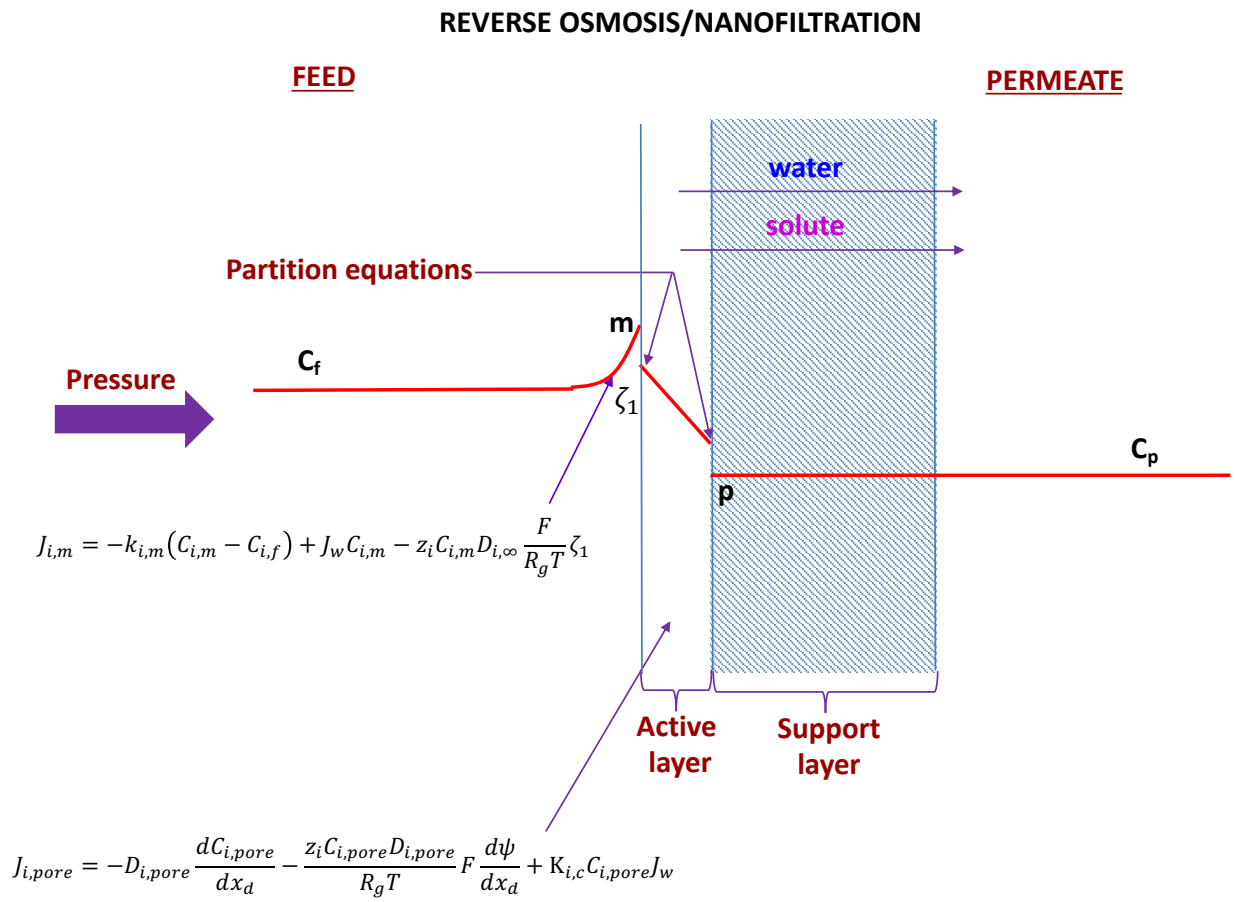

Figure 5-1a: Schematic diagram of an asymmetric polymeric membrane in a pressure-driven mode, such as RO or NF. Refer to the nomenclature for variable definitions.

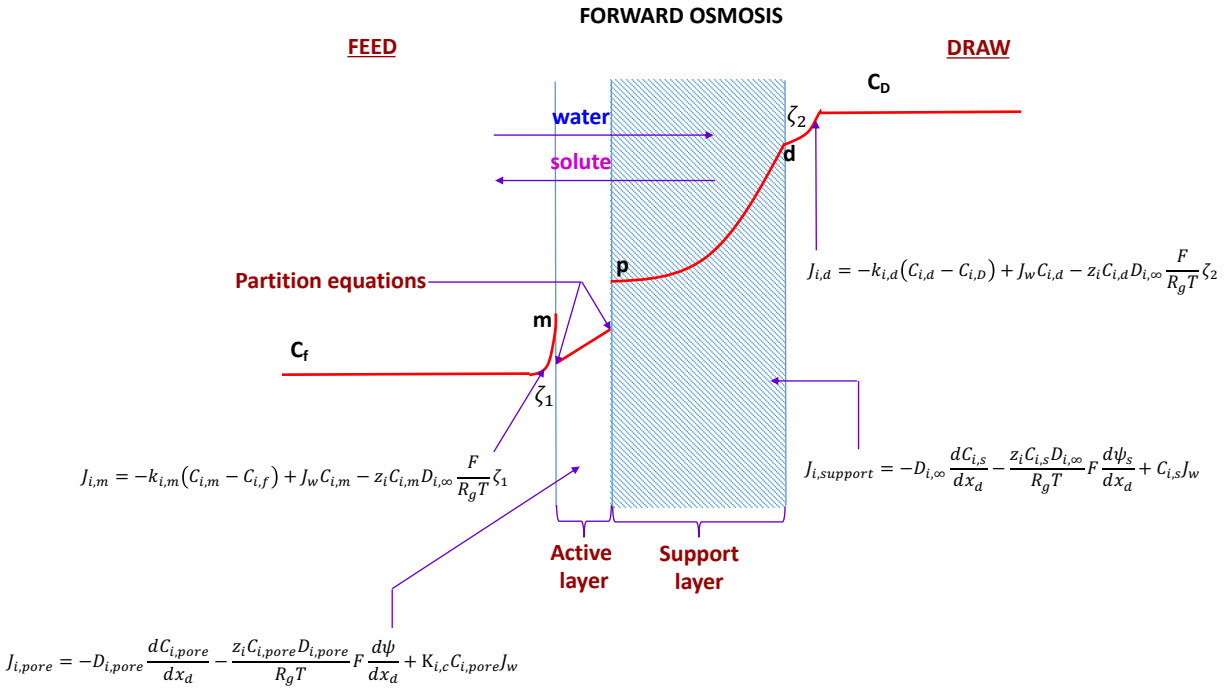

Figure 5-1b: Schematic diagram of an asymmetric polymeric membrane in FO mode. In this mode of use, salt and water transport are driven by the osmotic pressure gradient across the membrane. Refer to the nomenclature for variable definitions.

5.2.1. The Extended Nernst-Planck equation for ion transport in the active layer

In the current work, the transport of each ionic species i through the active layer is modeled using the Extended Nernst-Planck equation (ENP) (69). The ENP considers three simultaneous and linearly additive modes of ionic transport through the membrane: diffusion, electromigration, and convection. Applied to a porous medium, the ENP is:

$$J_{i,pore} = -D_{i,pore}\frac{dC_{i,pore}}{dx_d} - \frac{z_i C_{i,pore} D_{i,pore}}{R_g T} F \frac{d\psi}{dx_d} + \mathrm{K}_{i,c} C_{i,pore} J_w, \quad (5\text{-}1)$$

where x_d is the effective distance for diffusion through a porous medium. As mentioned in Ref. (84), the ENP provides a complete framework for modeling ionic transport through membranes; the only major assumptions being the linear relation between the diffusive flux and its activity gradient and the neglect of solute–solute interactions. The main purpose of models based on the ENP is to model membrane properties and transport mechanisms as realistically as possible. Implementation of molecular dynamics to model polymeric membranes is limited due to their complexity and the lack of adequate knowledge of membrane structure and properties (86).

5.2.2. Hindered motion through pores in the active layer

The 'Hindered transport theory' accounts for the constricted motion of solutes within membrane pores and the resulting interactions between the solute species and the pore wall. This is

implemented by modifying each term of the ENP by hindrance coefficients. The hindered transport theory has already been implemented successfully for transport of uncharged solutes through FO membranes (87). In Ref. (87), the authors used the simplified expression for rejection ratio derived by Bowen et al. (3) for uncharged solutes to characterize pore radius. They consider concentration polarization using film theory, which can be derived from the ENP if the electromigration term is removed (cf. Eq. 5-1 below). In Ref. (87), the pore radii of FO membranes were determined to be similar to that of loose NF membranes, such as the NF270 ($r_{pore} \cong 0.43$ nm). In other studies, empirical measurement of the pore radii of certain RO and NF membranes indicated pore radii of these membranes were between 0.24-0.3 nm; the pore size of NF membranes fell on the larger end of the spectrum compared to RO membranes (11,12). As explained in detail in Section 5.6.2, the large values of FO pore size fitted in Ref. (87) compared to those in the current work is explained by the smaller Stokes radius of sodium and chloride ions compared to that of uncharged solutes used in (87).

The intra-pore diffusion coefficient is the product of the hindrance coefficient for diffusion and the bulk diffusivity of a given solute:

$$D_{i,pore} = K_{i,d} D_{i,\infty}. \tag{5-2}$$

This modified diffusion coefficient is used in the diffusion and electro-migration terms of the ENP (Eq. 5-1). Similarly, the factor $K_{i,c}$ is used to modify the convection term in Eq. 5-1 to account for hindered convective transport within the membrane (third term in Eq. 5-1). For NF studies, correlations have been derived semi-empirically for $K_{i,d}$ and $K_{i,c}$ and are given in Appendix D. Although termed "hindrance" coefficients (3,29), $K_{i,d}$ and $K_{i,c}$can be interpreted as weighting factors for their transport mode. The value of $K_{i,d}$ ranges from 0 to 1. It takes a value of zero when

the solute is as large as or larger than the pore (in which case there is no diffusion i.e. diffusion is entirely hindered leading to zero intra-pore diffusivity). $K_{i,d}$ is equal to 1 when the solute is much smaller than the pore because the ion can diffuse freely in the pore without hindrance (i.e., the intra-pore diffusivity is equal to the bulk diffusivity). The trend of variation of $K_{i,c}$ with variation in the solute radius to pore radius ratio, $\left(\frac{r_i}{r_{pore}}\right)$, is more complicated. $K_{i,c} \rightarrow 1$ for $\left(\frac{r_i}{r_{pore}}\right) \rightarrow 0$ and $\left(\frac{r_i}{r_{pore}}\right) \rightarrow 1$ in the case of cylindrical pores (88). For intermediate values of $\left(\frac{r_i}{r_{pore}}\right)$, $K_{i,c}$ is greater than 1 and reaches a maximum value of approximately 1.5. The derivation of $K_{i,c}$ from macroscopic hydrodynamics is discussed in Ref. (88).

5.2.3. Partitioning equations describing ion exclusion at membrane–solution interfaces

Partitioning describes the extent to which entry of ions into the membrane is permitted. Effects such as sieving (steric exclusion) and charge-based exclusion (Donnan exclusion) by the membrane determine the extent of partitioning, which is quantified by the ratio of ions within the membrane to that outside the membrane (cf. Eqs. 5-4 and 5-5).

5.2.3.1. The Steric partitioning factor

The existence of pores in the membrane gives rise to steric hindrance of ionic species attempting to enter the membrane. Steric hindrance is a sieving effect through which solute species larger than the membrane's pores are inhibited from entering the membrane. The steric hindrance effect is quantified by means of the steric partitioning factor Φ_i, which is given by Eq. 5-3 (3,35). The value of Φ_i lies between 0 and 1. The variation of Φ_i is explained as follows: if ion i is comparable in size to the pore, $r_i \cong r_{pore}$ and $\frac{r_i}{r_{pore}} \rightarrow 1$; correspondingly, $\Phi_i \rightarrow 0$ as per Eq. 5-3. Thus, in the

limit of $\Phi_i \rightarrow 0$, the ion cannot enter the membrane due to size-based exclusion. Similarly, in the limit that the ion is much smaller than the pore dimension, $\Phi_i \rightarrow 1$ and the ion experiences no size-based exclusion.

$$\Phi_i = \left(1 - \frac{r_i}{r_{pore}}\right)^2 \tag{5-3}$$

5.2.3.2. Donnan exclusion

A membrane potential develops due to the difference in mobilities of the various ions traversing the membrane (29). This membrane potential serves to balance the transport of membrane counter-ions and co-ions in the membrane and maintain quasi-electroneutrality within the membrane. The difference between the values of the membrane potential just within the membrane on the feed side (at the pore-opening) and that in the bulk feed solution is termed as the Donnan potential on the feed side, $\Delta\psi_{D,m}$. Correspondingly, the difference in potential value at the pore-opening on the permeate side and in the permeate bulk is the Donnan potential on the permeate side, $\Delta\psi_{D,p}$. $\Delta\psi_{D,m}$ and $\Delta\psi_{D,p}$ are schematically represented in Fig. 5-2. These Donnan potentials at each membrane-solution interface give rise to Donnan exclusion on the corresponding faces of the membrane. Donnan exclusion serves to increase the concentration of ions within the membrane that have charge (valence) opposite to the sign of the Donnan potential. Conversely, the intra-membrane concentrations of ions that have the same sign of charge as the Donnan potential are reduced due to the action of the Donnan potential. These effects of the Donnan potential on solute partitioning are termed Donnan exclusion effects, which is slightly misleading because certain ions (depending on their charge) are actually attracted into the membrane due to the Donnan potential.

5.2.3.3. Equilibrium boundary conditions on membrane surfaces

For RO and NF, the combination of the steric and Donnan exclusion effects is quantified in Eqs. 5-4 and 5-5 for the feed and permeate sides, respectively. Since exclusion effects determine the extent of partitioning of concentrations between the bulk solutions and the membrane, they are also known as partitioning equations. These equations provide the ratios between the ionic concentrations for each species within the pore-opening by the concentration outside the membrane. A higher value of this ratio implies that the ion is better able to enter the membrane and experiences less exclusion overall due to the combination of steric and Donnan effects.

$$\frac{\gamma_{i,pore} C_{i,pore}}{\gamma_{i,m} C_{i,m}} = \Phi_i \, exp\left(-\frac{z_i F}{R_g T}\psi_{D,m}\right)\Bigg|_{in} \tag{5-4}$$

$$\frac{\gamma_{i,pore} C_{i,pore}}{\gamma_{i,p} C_{i,p}} = \Phi_i \, exp\left(-\frac{z_i F}{R_g T}\psi_{D,p}\right)\Bigg|_{out} \tag{5-5}$$

For FO, Eqs. 5-4 and 5-5 still apply, except that the subscript p in Eq. 5-5 refers not to the permeate side but to the point within the support layer shown in Fig. 5-1b.

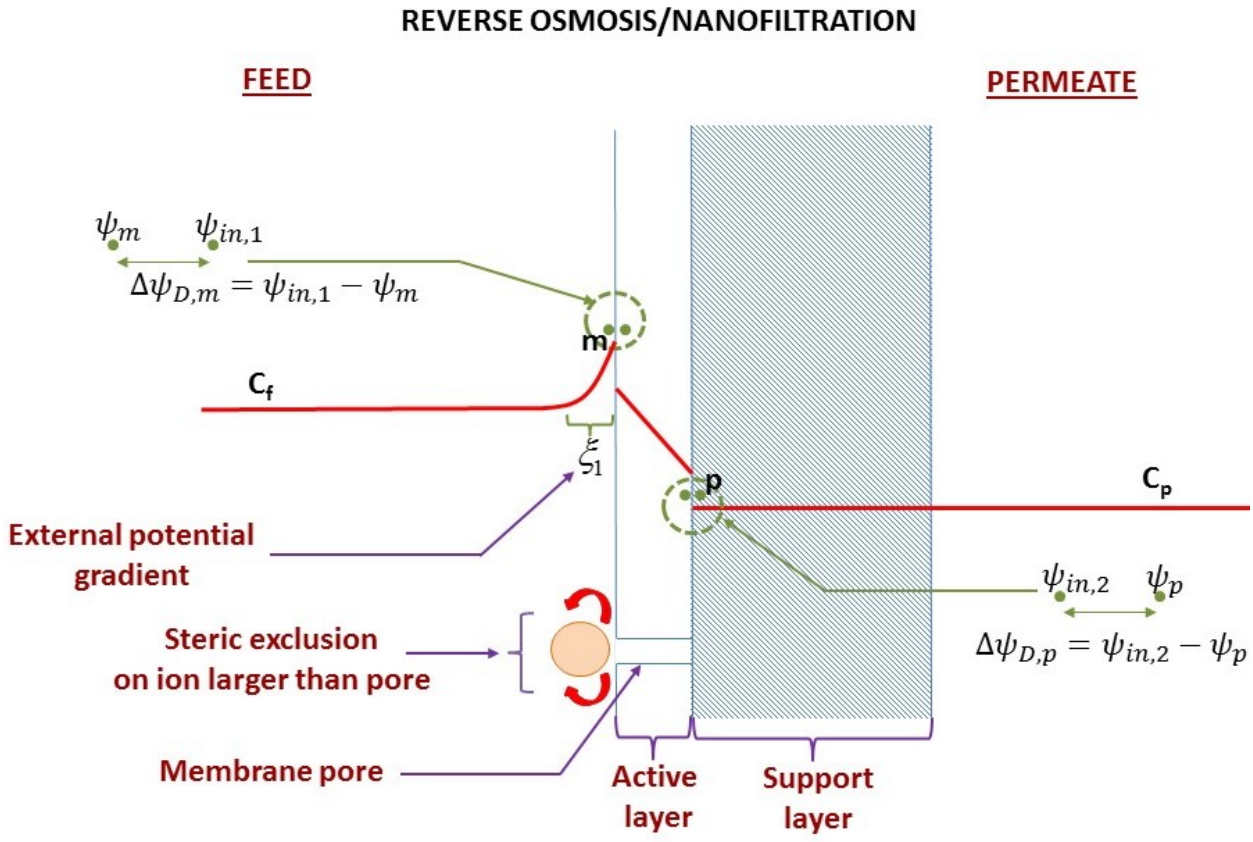

Figure 5-2: Schematic diagram of partitioning mechanisms in an RO/NF membrane. The Donnan potentials on the feed side and permeate side are shown. The mechanism of steric exclusion is represented.

5.2.4. Removal of charge-based exclusion effects

Literature on both molecular dynamics and continuum modeling of NF membranes tends to include effects of both dielectric exclusion and membrane charge. A notable drawback of pore flow models that include these effects is the need for several fitting parameters (73). The most comprehensive existing model of NF (25,29) requires four parameters: pore radius, membrane effective thickness, membrane volumetric charge density and pore dielectric constant. The procedure for fitting these parameters requires an elaborate, multi-step experimental procedure (25,33,39). Membranes used for NF, reverse osmosis and forward osmosis develop a membrane

charge in solution (31,38,69,70,87,89). This membrane charge results from the dissociation of the functional groups in solution and gives rise to a zeta potential, which is most commonly a negative value for solutions at near neutral pH. In terms of modeling, the membrane charge is usually represented by a membrane volumetric charge density, which is assumed to be uniform throughout the membrane active layer (3,25,29). The volumetric membrane charge density is the most problematic fitting parameter because it depends on the concentration of all ions in solution as well as solution pH.

In order to reduce the number of fitting parameters, dielectric exclusion and membrane charge are omitted in the current study. Despite these omissions, the proposed model successfully models both RO and FO membranes, as shown in Section 5.3. Furthermore, Section 5.6.2 discusses how the omission of these effects is necessary to allow simultaneous validation of RO and FO using the same set of fitting parameters. It is to be emphasized that the RO and FO data used for validation in this work are taken from the same source in literature and obtained from the same membrane. Consequently, it was a priority in the current work to use the same membrane parameters for both modes of operation. The remarkable fact that despite the very different mechanisms of RO and FO, the model could be validated for both processes by fitting only membrane geometric parameters indicates that charge effects are not significant for RO and FO. In contrast, NF model validation for even salts with only monovalent ions (e.g. NaCl, KCl and LiCl) requires contribution of charge-based effects (31). This difference is presumably due to the model's increased sensitivity to charge-based effects at larger pore size ranges. From a modeling perspective, for NF membranes, pore sizes of ~1 nm are required to attain a realistic value of membrane solvent permeability. Under these circumstances, to validate the model for solute flux,

the charge-based effects need to be included in order to attain a desired solute permeability, which is over-estimated when only steric effects are considered.

Additionally, the combination of the Donnan and steric exclusion has been found to be adequate for solutions with only sodium chloride (the salt used in the experimental works against which the present model is validated) in other literature (31,80). Some authors also find that the Donnan exclusion by itself describes certain membrane filtration experiments well. One such case is that described by Higa et al. (40), in which the authors validate a model considering only Donnan exclusion with experiments using potassium, calcium and chloride ions. Also, as described earlier (Section 5.1.2), the TMS model that considers only Donnan exclusion has been validated for RO (69,70).

5.2.4.1. Number of fitting parameters

One notable characteristic of the current model is that the fitting parameters characterize the membrane itself, irrespective of the species in solution. As a result, the number of fitting parameters does not increase with the number of ions in solution as occurs in the SD model. In the current work, the model is utilized to simulate the transport of Na^+ and Cl^- only; multi-ionic simulations might necessitate the inclusion of charge-based fitting parameters (membrane charge and/or pore dielectric constant) as. However, these charge-based parameters also convey information about the membrane itself, rather than being specific to each individual solute species.

5.2.5. Salt transport in the support layer (internal concentration polarization)

The ENP is used to model the ionic transport in the support layer as well. However, since the support layer is essentially an ultrafiltration membrane, with pores of the micrometer range (90–92), the effect of hindered transport is not required. The form of the ENP used is given as follows:

$$J_{i,support} = -D_{i,\infty}\frac{dC_{i,s}}{dx_d} - \frac{z_i C_{i,s} D_{i,\infty}}{R_g T} F \frac{d\psi_s}{dx_d} + C_{i,s} J_w, \tag{5-6}$$

where x_d is the effective distance for diffusion in the porous support layer, which accounts for support layer tortuosity or porosity. The most notable difference between the above equation and Eq. 5-1 is in the absence of the hindrance factors; as a result, the bulk ion diffusivities, $D_{i,\infty}$, are used. The solution of the above equation and the resulting concentrations within the support layer determine the extent of internal concentration polarization (ICP), which significantly reduces the osmotic pressure difference across the membrane in FO, and hence is undesirable (13,63).

5.2.6. External concentration polarization

External concentration polarization (ECP) occurs in membrane desalination processes due to the development of a concentration boundary layer between the membrane surface and the bulk solutions on both sides of the membrane. The net solute flux at the feed–membrane interface is the sum of diffusive, convective, and electromigrative components as shown in Eq. 5-7 and Figs. 5-1a, 1b (29):

$$J_{i,m} = -k_{i,m}\left(C_{i,m} - C_{i,f}\right) + J_w C_{i,m} - z_i C_{i,m} D_{i,\infty}\frac{F}{R_g T}\zeta_1. \tag{5-7}$$

In the case of FO, the corresponding mass balance for the ECP layer between the support layer and the draw solution (see Fig. 5-1b) is:

$$J_{i,d} = -k_{i,d}\left(C_{i,d} - C_{i,D}\right) + J_w C_{i,d} - z_i C_{i,d} D_{i,\infty} \frac{F}{R_g T} \zeta_2. \quad (5\text{-}8)$$

In the two equations above, the bulk ion diffusivities are used because hindered transport does not occur outside the membrane.

The FO experimental data for validation was taken from Ref. (15) in which the crossflow velocity on both sides of the membrane was 0.232 $m \cdot s^{-1}$, but the modeling in that reference does not consider ECP. In the current modeling, an expression for external mass transfer coefficient from Ref. [4] was used to calculate a value of 1.095×10^{-4} $m \cdot s^{-1}$ for the external mass transfer coefficient.

5.2.7. Constraints on solute fluxes and concentrations

To ensure no net electrical current through the membrane (since there is no applied potential across the membrane) (37,73),

$$\sum_{i=1}^{N_c} z_i J_{i,pore} = 0. \quad (5\text{-}9)$$

Furthermore, to represent steady, one-dimensional salt flux through the membrane, the solute flux must be the same across each interface of the membrane:

$$J_{i,pore} = J_{i,m} = J_{i,support} = J_{i,d}. \quad (5\text{-}10)$$

Electroneutrality (no net charge in the bulk solution) is imposed within the solutions on both sides of the membrane and within the support layer. Since the membrane charge effect is omitted from the current modeling, Eq. 5-11 holds within the active layer as well.

$$\sum_{i=1}^{N_c} z_i C_i = 0 \tag{5-11}$$

5.2.8. Water Transport

The expression for water flux used in the current model was derived from the hindered transport theory (3,35,36):

$$J_w = \left(\frac{r_{pore}^2}{8\nu\rho_w \Delta x_{flow}}\right) \Delta P_{net} = \left(\frac{r_{pore}^2}{8\nu\rho_w \Delta x_{flow}}\right) \left((P_f - P_p) - \Delta\pi\right). \tag{5-12a}$$

This expression is almost identical to the Hagen-Poiseuille equation for laminar flow through a bundle of straight pipes with length equal to the active layer thickness δ and open area fraction equal to the porosity φ, resulting to an effective length defined as $\Delta x_{flow=\delta/\varphi}$. However, in Eq. 5-12a, the driving pressure across the length of the pipes is the net driving pressure across the membrane, ΔP_{net} instead of the applied hydraulic pressure difference $\left(P_f - P_p\right)$ used for traditional pipe-flow. The $\Delta\pi$ enters the expression due to the interrelation between intra-pore pressure and solute concentration given by the Gibbs-Duhem equation, as described in detail in Ref. (36). In the expression for water flux derived in Ref. (36), $\Delta\pi$ is multiplied by the Staverman reflection coefficient which represents the effect of the solute-pore wall interaction potential; however, this water flux equation was later adjusted as described by Bowen et al. (3). As per the formulation of Bowen et al. (3), the solute-pore wall interactions are modeled as exclusion mechanisms and are represented in the partitioning equations (Eq. 5-4 and 5-5 shown previously); for example, the expression for steric partitioning factor given by Eq. 5-3 appears in the expression for reflection coefficient in Eq. 20 of Ref. (36).

In the current modeling, the osmotic pressure difference across the membrane is given by the van 't Hoff relation shown in Eq. 5-12b. This relation is chosen because validation in Section 5.3 will be done with respect to data in Ref. (15), in which the applicability of the van 't Hoff relation for the considered concentration range is demonstrated. The authors of Reference (15) validate the use of Eq. 5-12b i.e. a linear relationship between osmotic pressure and feed concentration over the range of NaCl concentrations used in their experiments.

$$\Delta \pi = i_v R_g T (C_m - C_p) \tag{5-12b}$$

Previous implementations of the DSPM in modeling NF assume that the effective lengths for flow and diffusion (Δx_{flow} from Eq. 5-12a and Δx_d from Eq. 5-1) are equal (3,31). This work will similarly assume that $\Delta x_{flow} = \Delta x_d$ in the bulk of the modeling, but will also test the effect of relaxing this assumption in Section 5.3.4. The potential for these effective lengths to differ depending upon the transport mechanism is explained in Appendix F.

5.2.9. Model inputs

Table 5-2 below provides a list of input parameters to the model. Model validation, which will be described in Section 5.3, involves fitting these parameters and using the resulting values to elucidate the physics of membrane transport.

Table 5-2: Summary of input parameters that will be used in model validation

Parameter	Name	Description
r_{pore}	Pore radius of membrane active layer	Determines steric hindrance to the entry of ions and resistance to water flow into the membrane (a larger value allows more passage of both ions and water)
Δx	Effective active layer thickness	Effective active layer thickness when $\Delta x_{eff,f} = \Delta x_{eff,d}$. Determines water flux through the membrane as per Eq. 5-12a. Also influences salt flux (a larger value reduces salt flux)
$L_{support}$	Support layer structural parameter	Determines the extent of internal concentration polarization (ICP) in the support layer (Fig. 5-1b)
K_d	Hindrance factor for diffusion	Modifies diffusion rates of ions in active layer according to the relation $D_{i,pore} = K_{i,d} D_{i,\infty}$ (cf. Eq. 5-2)
K_c	Hindrance factor for convection	Modifies convection rates of ions in active layer (cf. Eq. 5-1)

5.3. Results: the persistence of solution–diffusion in unpressurized mode

In this section, the general model will be validated with respect to RO and FO data from Tang et al. (15). In Section 5.3.5, a flow chart summarizing the pathway to achieve validation is provided. The results in the following sections demonstrate that while the inclusion of convective salt transport improves model agreement with RO experimental data compared to SD, removal of this mode of transport was essential to allow model validation for the FO mode. Thus, convective coupling between water and solute transport is significant for the pressure-driven mode, while it

is negligible for the unpressurized FO mode. The modeling results from Tang et al. for both RO and FO were obtained by those authors using the traditional SD model.

5.3.1. Fitting active layer geometric parameters in RO

As a first step, the pore radius, r_{pore}, and effective thickness of the active layer, Δx of a Hydration Technology Innovations (HTI) cellulose triacetate (CTA) membrane were determined from fitting experimental RO water flux and sodium-chloride rejection ratio data from Ref. (15) (cf. Fig. 5-3 in that reference). The HTI CTA membrane was modeled because that membrane was used in the validation datasets (15,16). The fitting procedure for the pore radius and effective active layer thickness is summarized in Appendix E. RO data cannot be used to fit the support layer structural parameter because there is no internal concentration polarization (ICP). The values of the hindrance coefficients $K_{i,d}$ and $K_{i,c}$ for each ion (where i is either Na^+ or Cl^- in this case) are obtained from correlations in Ref. (29), which are used widely for modeling NF membranes (25,29) and are reproduced in Appendix D. Table 5-3 provides a summary of the model inputs used for fitting the pore radius and effective active layer thickness from RO data.

Table 5-3: A summary of model inputs used for fitting pore radius and active layer effective thickness

Parameter	Value
r_{pore}	To be fitted
Δx	To be fitted
$L_{support}$	Not applicable in RO
K_d	Calculated using expressions from Appendix D.
K_c	Calculated using expressions from Appendix D.

An exhaustive search across an acceptable range of pore radii (0.19 nm to 0.30 nm in increments of 0.001 nm) was performed to determine the value of pore radius and the corresponding active layer thickness that minimized the difference between the simulated and experimental water fluxes and salt rejections (cf. Appendix E for optimization details). The lower bound of the range was chosen to be just above the Stokes radius of the sodium ion (the larger of the two ions in a sodium chloride solution), which is approximately 0.184 nm (80). The upper bound of the range was initially set at 0.3 nm, and it was later confirmed that this radius was greater than the optimum radius, as shown in Fig. 5-3.

The fitting procedure uses experimental bulk feed concentration, water permeability, water flux and rejection ratio values as inputs. For each guess value of pore radius, the extent of concentration polarization and the effective pressure difference across the membrane are calculated. The optimal effective active layer thickness for each pore radius value is calculated by rearranging Eq. 5-12a and using the simulated value of effective pressure difference across the membrane (see Appendix E). Fig. 5-3 shows the variation of error (given by Eq. B.4, which accounts for the error in both rejection ratio and water flux) across the pore radius range simulated. The search yielded a local minimum error at 0.205 nm, which corresponds to an active layer effective thickness of 2.68 μm. The error in the plot is given by the expression in Eq. B.4. and accounts for the error with respect to both the experimental rejection ratio and water flux.

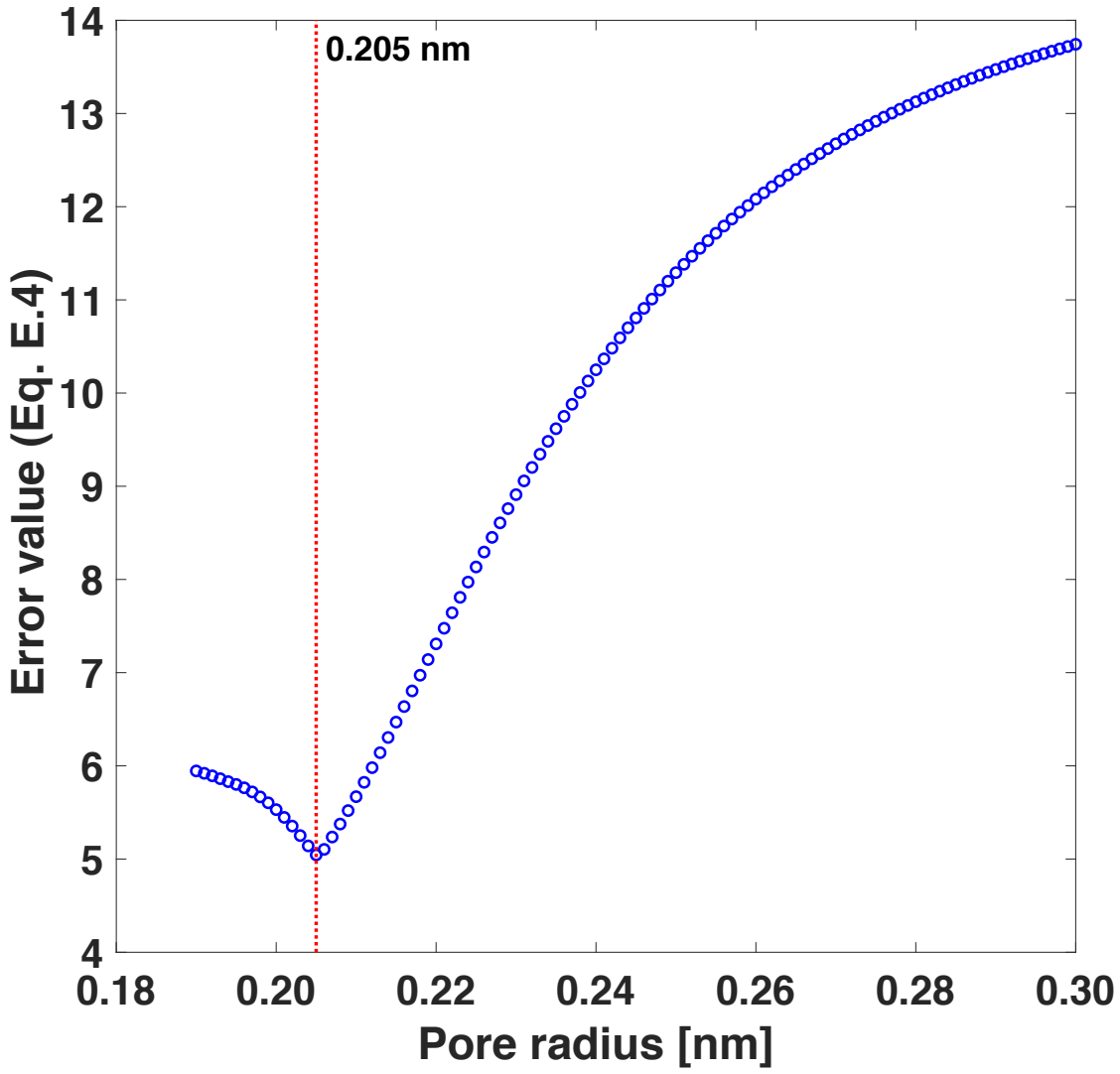

Figure 5-3: Value of the error (Eq B.4.) comparing the experimental and predicted solvent fluxes and sodium-chloride rejection ratios over a range of possible FO membrane pore radii (0.19-0.3 nm). The error function was minimized at a pore radius of 0.205 nm, which corresponds to an effective active layer thickness of 2.68 μm.

Figure 5-4 compares the experimental solvent flux and rejection ratios with the corresponding simulated values obtained using the optimal pore radius of 0.205 nm and active layer thickness of 2.68 μm. Hindrance coefficients were obtained from Appendix D. The mean error in rejection ratio across all data points was approximately 0.5%, while the mean error values in water flux and solute flux values were 0.03% and 4% respectively (the latter is not shown). The low error for all three quantities indicates that the model captures the physics of RO well.

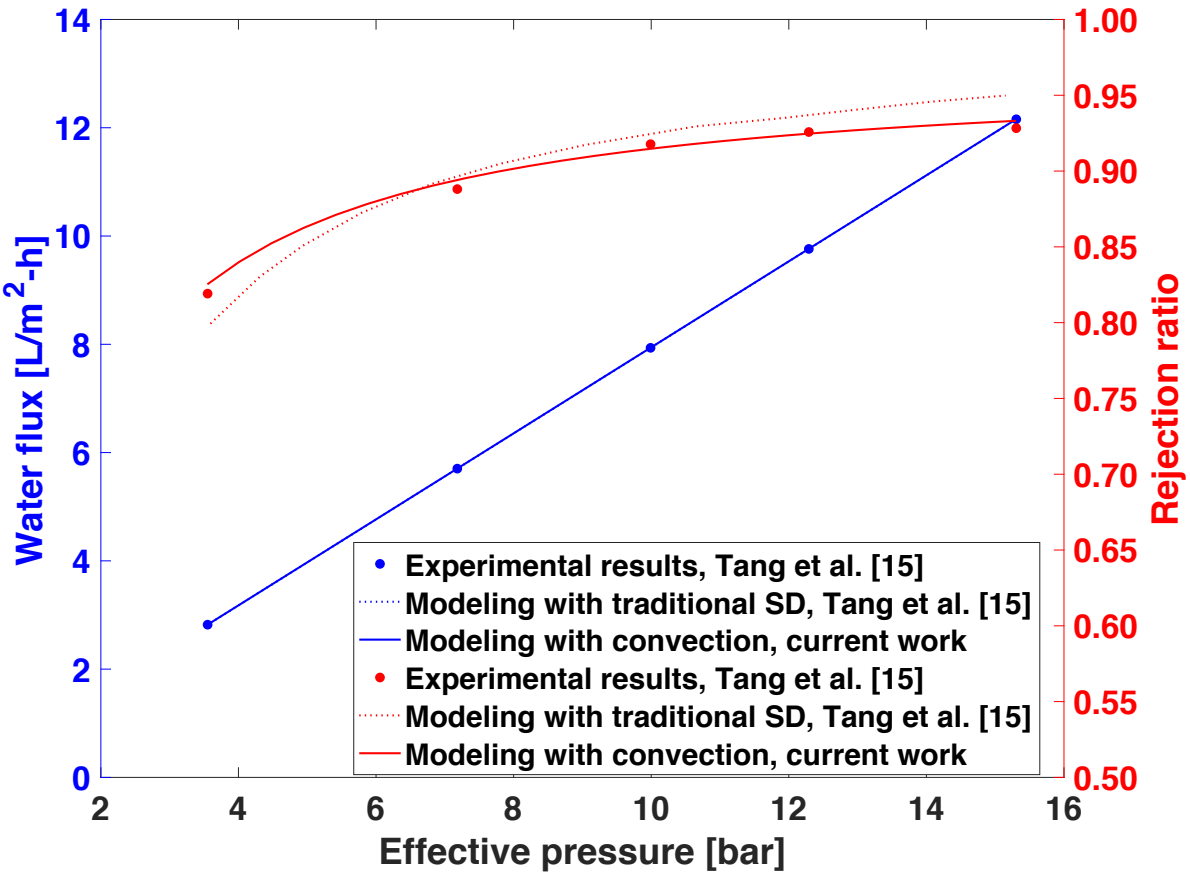

Figure 5-4: A comparison of the experimental and simulated solvent fluxes and rejection ratios with pressure variation in RO; the simulated values were obtained using a pore radius of 0.205 nm, an active layer thickness of 2.68 μm and hindrance coefficients from Appendix D. The mean percentage error between the experimental and simulation values of solvent flux and rejection ratio were ~ 0.03% and 0.5% respectively. Although not plotted, the mean percentage error on solute flux was calculated to be 4%.

5.3.2. Attempted extension of model to FO

The r_{pore} and Δx fitted in Section 5.3.1 lead to model agreement with RO experimental data. The next step is to check if these values allow the FO model to match experimental data for water flux and salt flux in FO. A summary of the input parameters used during this step is given in Table 5-4 below.

Table 5-4: A summary of the input parameters used to model FO in Section 5.3.2.

Parameter	Value	Source
r_{pore}	0.205 nm	Section 5.3.1
Δx	2.68 μm	Section 5.3.1
$L_{support}$	400 μm	Best-fit value
K_d	0.0035 (Na^+), 0.1172 (Cl^-)	Expression in Appendix D.
K_c	1.1216 (Na^+), 1.3269 (Cl^-)	Expression in Appendix D.

Experimental FO data for water flux and salt flux (of sodium chloride) was obtained from Fig. 5-4 in the study of Tang et al. (15), which shows the results of experiments using a bench-scale cross-flow setup with a fixed feed concentration of 10 mol m^{-3} (10 mM) and variable draw concentration. Figure 5-5 below shows the water flux and salt flux obtained from the current model using the input parameters given in Table 5-4, along with experimental results from Fig. 5-4 in Ref. (15). As shown in Figs. 5-5a and 5-5b, the predicted water and solute fluxes using the best-fit value of $L_{support}$ did *not* agree with the experimental data from Ref. (15); the mean percentage errors were 4.7% and 71%, respectively. Assuming that the governing equations of Section 5-2 are correct and that the active layer geometric parameters are independent of the membrane's mode of use, the only remaining explanation for failure to validate the proposed model is that the hindrance coefficients, although valid for NF and RO, failed to capture the relative magnitudes of the diffusive and convective modes of ion transport in FO (ref. Sections 5.6.3. and 5.7.1. for further details).

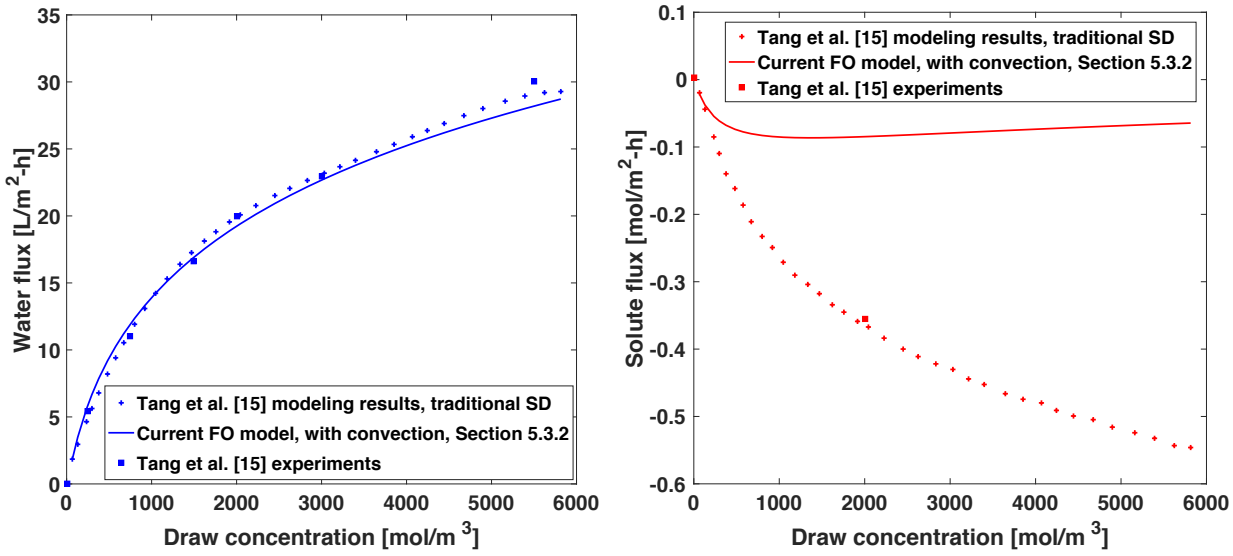

a. **b.**

Figure 5-5: (a) Water flux and (b) solute flux in FO: results from the current model (Section 5.3.2) as well as model predictions and experiments by Tang et al. (15). A comparison of the experimental and simulated solvent and solute fluxes at various draw concentrations for FO; the predicted solute fluxes are not in agreement with the experimental values with a mean percentage error of 71%. The agreement between experimental and simulated solvent fluxes is reasonably good, with the mean error being 4.7%. The simulated values were obtained using the active layer parameters fitted from RO in Section 5.3.1. (Table 5-4), while the best fit value of support layer structural parameter, L_s, was fitted from the data (400 μm).

5.3.3. Establishing the requirements for successful RO and FO modeling

The previous section suggests that the unsuccessful model validation with FO experimental results thus far is due to the failure of the correlations for $K_{i,c}$and $K_{i,d}$ (cf. Appendix D). In the light of the longstanding success of (solute convection-free, i.e., traditional) SD for FO modeling as reflected in literature (15,16,63), the success of the model after the removal of the convective mode of transport is evaluated. The removal of convective ion transport is achieved by setting the convective hindrance coefficients for each ion to zero ($K_{i,c} = 0$) in Eq. 5-1. Ideally, the active layer parameters should be the same for both RO and FO, so that the user does not need to re-fit these parameters for each case. Although using the same active layer geometric parameters for RO

and FO neglects membrane compaction due to high pressure in RO mode, that idealization will allow the use of the same active layer characteristics (r_{pore} and Δx) regardless of the desalination process.

5.3.3.1. RO after removal of the convective mode of transport

Re-fitting the RO model with experiments after removing the convective mode of transport gave an optimal pore radius of 0.207 nm and a corresponding active layer thickness of 2.73 μm. The mean errors between the experimental and simulated values of rejection ratio (see Fig. 5-6), solvent flux and solute flux were found be 1% , 0.06% and 11% respectively, which are higher than the corresponding values when solute convection is included (Section 5.3.1), most notably for the solute flux. From Fig. 5-6, it is clear that the modeling results excluding convection match those from the traditional SD from reference (15).

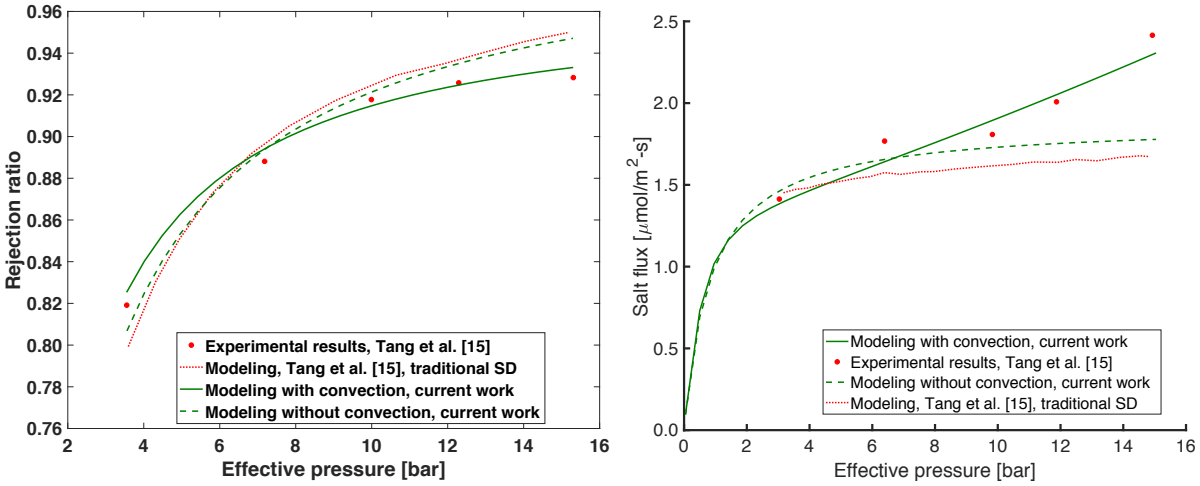

Figure 5-6. A comparison of the experimental and simulated rejection ratios at various applied pressures for RO with and without convection. The optimal value of pore radius after the removal of convection in RO was found to be 0.207 nm, and the corresponding optimal effective active layer thickness was 2.73 μm. The removal of convection caused a higher error in water flux, rejection ratio and solute flux (0.06%, 1% and 11% respectively) compared to the modeling results with convection included.

5.3.3.2. FO after removal of the convective mode of transport

After removing the convective mode of transport and employing the active layer parameters obtained from RO (Section 5.3.3.1), the mean errors for the water flux and solute flux in FO were 4.1% and 27.5% respectively, lower than those seen in Section 5.3.2 where convection was included, most significantly for the solute flux. The reduction in error on both water flux and solute flux for FO after the removal of convection indicates that accuracy in modeling this process is improved by moving toward an SD-based approach, and other considerations discussed in subsequent sections will further improve the agreement. (Fitting with respect to $K_{i,d}$ was also done but did not lead to successful modeling of FO, as described in Appendix G.)

Table 5-5: A summary of the inputs used for FO modeling in the current section

Parameter	Value
r_{pore}	0.207 nm
Δx	2.73 μm
$L_{support}$	Best-fit value is 390 μm
K_d	0.0044 (Na^+), 0.1213 (Cl^-)
K_c	0 (Na^+), 0 (Cl^-)

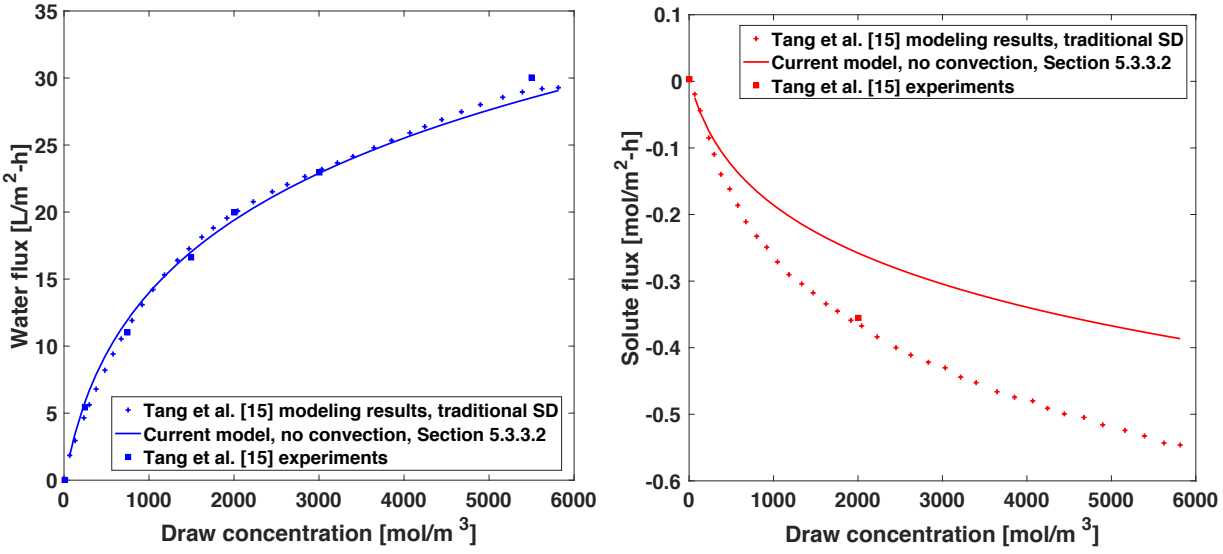

a. **b.**

Figure 5-7: (a) Water flux and (b) solute flux in FO: results from the current model (Section 5.3.3.2) as well as model predictions and experiments by Tang et al. (15). The experimental and simulated values of solvent and solute fluxes at various draw concentrations for FO; the mean percentage error between the experimental and simulated values were 4.1% and 27.5% respectively for water and solute fluxes. Both errors were reduced after the removal of convection, but more notably that of solute flux, which reduced to 27.5% from 71%.

5.3.4. Effect of unequal effective thicknesses for diffusion and flow

In order to improve the agreement in solute flux between the present model and the experimental results beyond that achieved in previous sections, more detailed modeling of the length of travel of species through the active layer is necessary. As explained in Section 5.2.8, the effective thickness of the membrane can be different for water flow and solute diffusion for tortuous pore structures (refer to Eqns. C.1. and C.2.). When the membrane is treated as a bundle of tubes with effective length greater than the physical membrane thickness, the ratio of Δx_{flow} to Δx_d is the tortuosity. A reasonable range for tortuosity for a wide range of porous materials is between 1 and 2 (93), so the value of $\Theta = \Delta x_{flow}/\Delta x_d$ was varied within these bounds. In addition to the parameters required for FO up to Section 5.3.3 (r_{pore}, Δx_{flow} and $L_{support}$), Θ is a fourth fitting parameter. $\Theta = 1.4$ was determined to be the optimal value that minimized the combined fractional

error (cf. Appendix E. for further details) between the model and experimental data for FO water flux and solute transport. The values of r_{pore}, $L_{support}$, $K_{i,d}$ and $K_{i,c}$ mentioned in Table 5-5 are used in this section. However, the effective active layer thickness has been differentiated to two forms as shown in Table 5-6. Since the RO model results had better agreement when the convective mode was included (Section 5.3.1), and it is desirable to use the active layer geometric parameters from RO-fitting for FO, the values from fitting in Section 5.3.1. will be used in this section.

Table 5-6: Summary of parameters used in FO model with unequal thicknesses for diffusion and flow ($K_{i,d}$ values were identical to those in Table 5-4, while $K_{i,c} = 0$ for both ions)

Parameter	Value
r_{pore}	2.05 nm
Δx_d	2.68 μm
Θ	1.4
Δx_{flow}	$\Theta \times \Delta x_d$ = 3.75 μm
$L_{support}$	Best-fit value is 310 µm

Figures 5-8a and 5-8b show the agreement between the experimental and modeling results after relaxing the assumption that $\boldsymbol{\Delta x_{flow} = \Delta x_d}$ to include the effect of tortuosity. The mean error with respect to experimental data for the solute flux decreased from 27.5% to 5.1% while the mean error

in water flux reduced from 4.1% to 3.4%. The results presented in this section indicate that the effect of pore tortuosity on membrane selectivity may warrant further study.

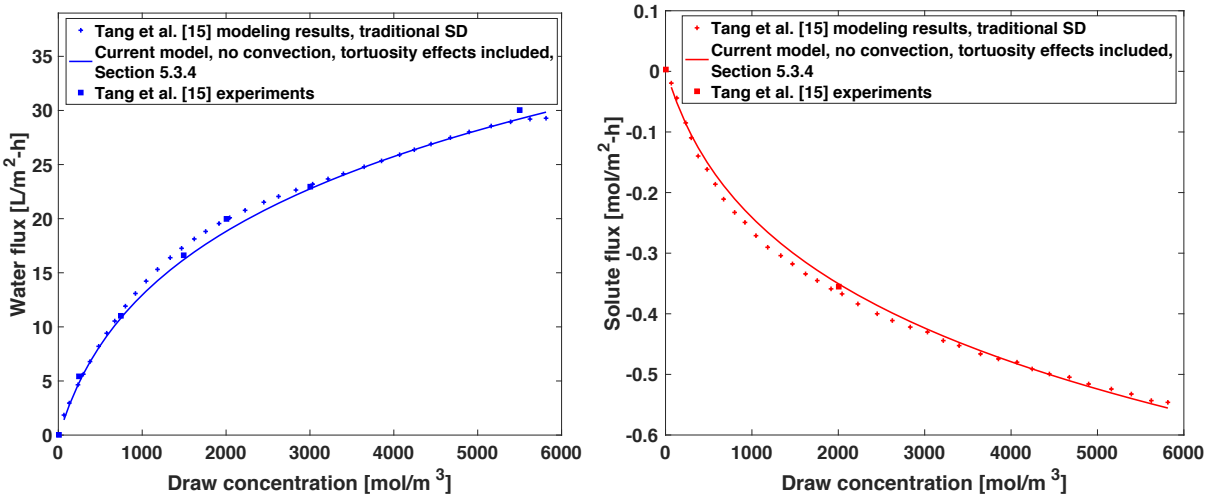

a. **b.**

Figure 5-8: (a) Water flux and (b) solute flux in FO: results from the current model (Section 5.3.4) as well as model predictions and experiments by Tang et al. (15). The experimental and simulated values of solvent and solute fluxes at various draw concentrations for FO when the effect of tortuosity is included; the mean percentage error between the experimental and simulated values were 3.4% and 5.1% respectively for water and solute fluxes.

5.3.5. Summary of model validation procedure for RO and FO

Figure 5-9 below shows a summary of the model validation procedure for RO and FO that was explained in Sections 5.3.1.- 5.3.4.

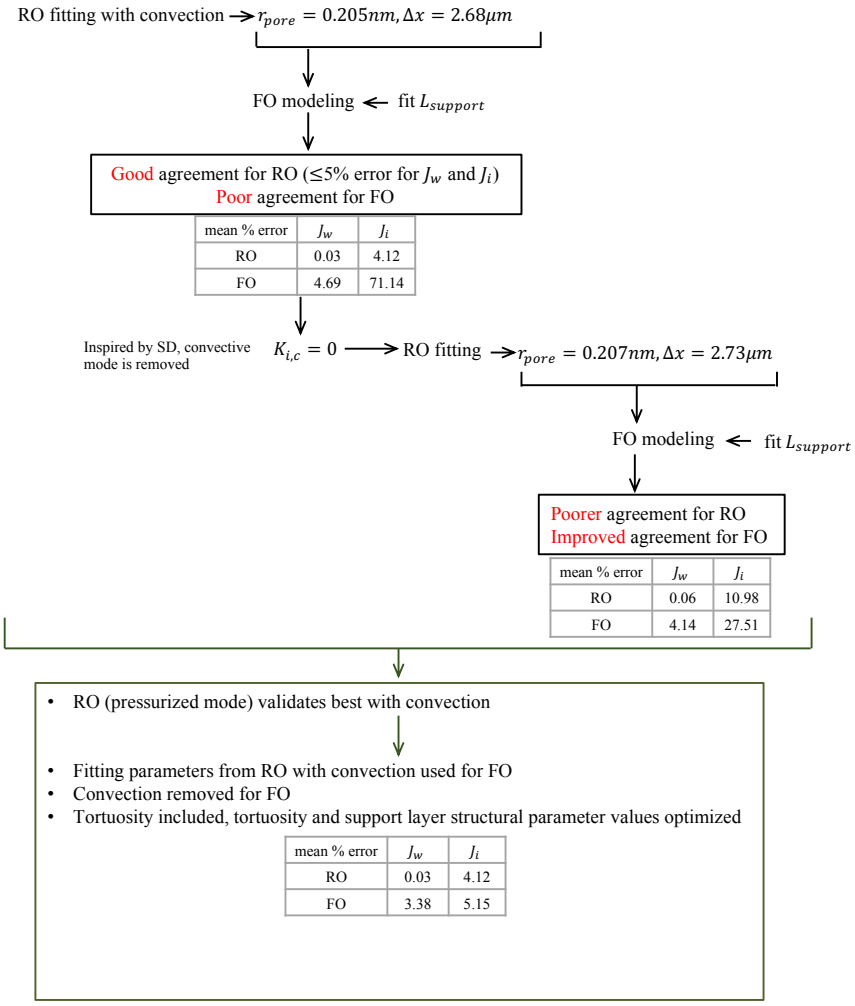

Figure 5-9. Flowchart summarizing validation procedure followed in Section 5.3. The modeling approach was improved until error for water and in fluxes was below 5% for both RO and FO, using the same active layer parameters.

5.4. Reinforcement of model validation

As a test of robustness, the model was validated with an additional FO dataset. This data was obtained from Fig. A.2 in Ref. (16) for FO water flux measured using the same membrane type used in Ref. (15) i.e. the HTI CTA. The active layer parameters used for these simulations are the same as those in Table 5-6, while the best-fit support layer structural parameter for this data-set was closer to that obtained in Section 5.3.3 (after removal of convection but without tortuosity for the data from Tang et al. (15)). These values are summarized in Table 5-7 below. The optimal tortuosity value for this data set was found to be $\Theta = 1.3$. Of the fifteen data points, the percentage error is below 5% for nine, between 5–10% for two and between 10–20% for four. Figure 5-10 shows the absolute error between the data and the current model along with those from the two modeling approaches shown in Ref. (16) (traditional SD and SD with dispersion). The SD model with dispersion shows the smallest error at all data points, but this model requires "dispersivity"[1] as an additional fitting parameter (16). Using the fitting parameters shown in Table 5-7, the current model gives a similar level of accuracy to traditional SD. The SD model with dispersion notably reduces the error compared to the other two modeling techniques but requires one more fitting parameter (a total of four). Although the modeling approach introduced in this work does not reduce the number of fitting parameters compared to the traditional SD approach, the fitted parameters are directly related to membrane properties. For example, the pore radius and membrane active layer thickness provide information about the membrane structure, in contrast to

[1] Dispersion is the apparent enhancement of diffusion by convection in a porous medium such as the FO membrane's support layer. In Ref. (16), "dispersivity" was introduced as an additional fitting parameter (a constant of proportionality between the increase in effective diffusion coefficient and the transmembrane flux) to improve agreement between the SD model and measured flux.

the phenomenological coefficients used in the SD model which need to be refitted for different solutes.

Table 5-7: Summary of parameters used in FO model for validation with Tow et al. (16).

Parameter	Value
r_{pore}	2.05 nm
Δx_d	2.68 μm
Θ	1.3
Δx_{flow}	$\Theta \times \Delta x_{eff,d}$ = 3.48 μm
$L_{support}$	Best-fit value is 390 µm
K_d	0.0035 (Na^+), 0.1172 (Cl^-)
K_c	0 (Na^+), 0 (Cl^-)

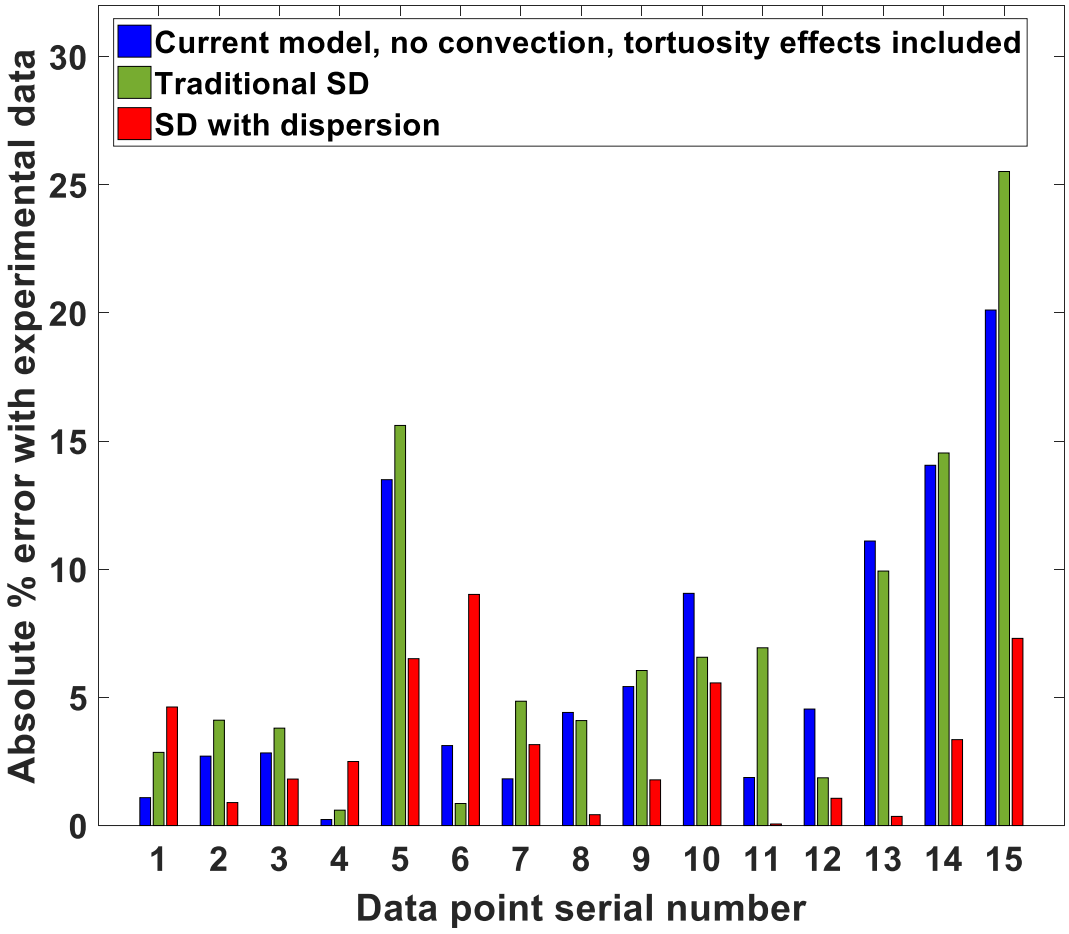

Figure 5-10. The three modeling approaches for FO are compared to experimental water flux data from Tow et al. (16). The current model attains error values comparable to traditional SD. The SD with dispersion has the lowest error, but also requires an additional fitting parameter.

5.5. Comparison of fitted membrane parameter values with measured values

Table 5-8: Comparison of fitted and measured values of membrane active layer.

Property	Ref. value (various cellulose ester FO membranes)	Current model
Pore radius	0.309-0.326 nm (94) 0.302 nm (95)	0.205 nm
Active layer thickness	0.2 μm (82)	$\Delta_{x_{eff,d}} = 2.68$ μm (if thickness $\delta \approx 0.2$ μm, area-based porosity $\phi = 7.5\%$)
Free volume fraction/porosity[2]	17.7-18.1% (by Bondi method) (94), 1.33-1.91% (from PALS measurement) (94) 5.28% (from PALS) (95)	
Tortuosity	1-2 (96)	1.4

Table 5-8 shows a comparison between fitted values of the active layer parameters of the HTI CTA membrane, and those measured by various experimental methods, for various cellulose ester FO membranes. References (94) and (95) mention results for various cellulose ester membranes, such as CA-398-10, CA-436-80S (CTA) and CAP-482-20, and only the ranges of values in these references over all studied membranes are mentioned in Table 5-8. Although the membrane is in wet state during operation, the measured value of pore radius reported in Table 5-8 are for dry FO membrane samples. However, these values are indicative of the relevant pore size in FO, because the maximum extent of variation between cellulose ester membranes is only about 5% (94). The

[2] A notable point is that the model uses surface porosity (i.e., the ratio of the surface area covered by pore openings to the total active layer surface area), while experimental measurements are reported in literature for free volume fraction through the active layer (the ratio of empty volume through the active layer to its total volume). This difference is attributed to the ease of measurement of free volume fraction using techniques such as PALS, while the present modeling approach was developed using surface porosity.

measured value of active layer thickness shown in Table 5-8 is that for a TFC membrane (FT-30), but, due to the lack of a specific value for cellulose acetate membranes in literature, the active layer thickness is assumed to be similar to that of a TFC membrane.

A notable observation from Table 5-8 is that the measured value of pore radius is consistently larger than that used in the current model. The smaller value of the fitted pore radius is attributed to the fitting being done using the Stokes radii of Na^+ and Cl^- ions, which are smaller than the corresponding hydrated radius values. As explained further in Section 5.6.2, if the larger hydrated radii had been used, the fitting procedure would have resulted in a larger pore size. Although ions in aqueous solution occur in a hydrated state, the hindered transport theory is based on the validity of Stokes equation in the pore, thereby necessitating the use of the Stokes radii of ions.

Since the model uses an effective value of active layer thickness, which is approximately the ratio between the actual active layer thickness and porosity, these values may only be estimated individually from the model fitting. Given that the model predicts an active layer thickness by porosity ratio of 2.68 μm, it can be inferred that if an active layer thickness of 0.2 μm is considered (as per the measured values quoted in literature), the porosity value is calculated to be 7.5%. As explained further below, this value of porosity is reasonable, given that measurements using PALS and other the Bondi method predict porosity to be between 5 and 20%.

The free volume fraction calculated by Bondi's method (the ratio of solvent-filled volume to total polymer volume, per unit mass) is much higher than that measured by PALS (94). This trend is commonly observed in literature and is attributed to the fact that PALS can only detect free volumes that are accessible by positrons (94). Factors such as the repulsion to the entry of positrons contribute to the lower measured value of free volume fraction by PALS, thereby qualifying PALS as a tool to compare various samples rather than give an accurate value of the free volume fraction

(94). Due to similar reasoning, the difference of ~0.1 nm between the pore radius obtained from PALS and that from modeling is not considered significant, since the PALS readings might not include the contribution of those voids that are not accessible by positrons. Furthermore, the fitted value of pore radius is lower than those used in literature for NF membranes, although of the same order of magnitude; thus showing that the model is able to capture the change in pore radius value between NF and RO/FO.

Overall, Table 5-8 shows that the fitted parameters are similar to measured values, suggesting it is no coincidence that the proposed model accurately predicts RO and FO experimental data. Not only does the proposed modeling technique predict membrane performance, but does so on the basis of measurable, geometric membrane properties. The closeness of the values from model fitting and those from direct measurements is particularly remarkable given that the model was obtained from the hindered transport theory, which was derived for macroscopic systems. As such, the model can be used to predict and explore the potential of new desalination membrane materials and designs.

5.6. Discussion

5.6.1. Error reduced in model validation

As illustrated in Fig. 5-11 and Figs. 5-4 and 5-6 earlier, the pore-based modeling approach employed in this work was successfully implemented for FO and RO. The approach of implementing the ENP for ion transport, along with the charge and steric-based exclusion effects, has been widely implemented for NF (29,31) and in some cases RO (70); however, to the best of the authors' knowledge, this is the first successful application of such a model to charged solutes' FO membrane transport. Furthermore, the implementation of the model for FO has been shown to

be possible using active layer parameters fitted from RO, thereby requiring additional fitting of only FO-specific parameters to implement the model for this mode. The success of this modeling approach required removal of the convective mode of solute transport in FO. The agreement of the model with RO data was best (and requiring only 2 fitting parameters, $r_{pore}$and Δx) when convection was included, but the mean error for both water flux and solute flux did not change very significantly for RO even in the SD (no convective transport) mode. However, the FO case was highly sensitive to the presence of the convective mode. The error in solute flux in FO was reduced dramatically from 71% to 25.7% upon the removal of ion convection in the active layer, and further to 5.1% upon optimizing the support layer structural parameter and tortuosity.

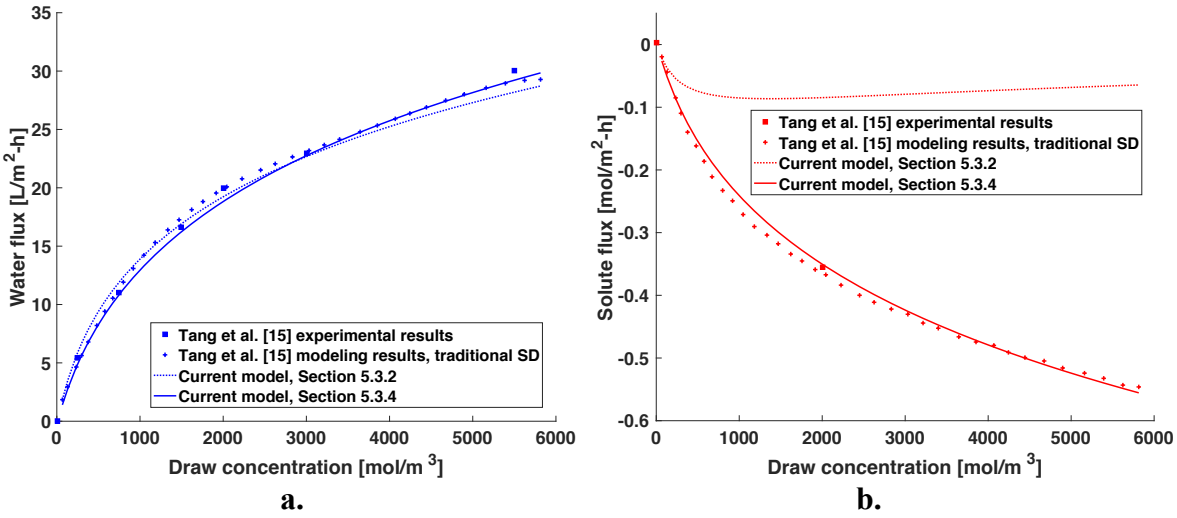

Figure 5-11. (a) Water flux and (b) solute flux in FO: results from the current model (Section 5.3.2 and 3.4) as well as model predictions and experiments by Tang et al. (15). Improvement in model agreement for FO after the convective mode of transport is removed and the effect of tortuosity included, as compared to the initial case when the unaltered ENP is used. The mean percentage error for FO water flux (a) reduced slightly from 4.7% to 3.4%, while that for the solute flux (b) decreased considerably from 71% to 5.1%.

5.6.2. Justification of removal of convection in FO modeling

In order to match the current model with experimental FO data, the convective mode of transport had to be eliminated. It was then possible to validate the model for FO using active layer

parameters fitted from RO. The $K_{i,d}$ values used for both FO and RO modeling can be obtained from established correlations. Subsequently, $L_{support}$ and Θ need to be fitted independently for FO modeling. Table 5-9 summarizes how the input parameters for the FO modeling are obtained. While the removal of convection and use of parameters shown in Table 5-9 allowed the major reduction in FO solute transport error (71% to 25.7%), further improvement (25.7% to 5.1%) was obtained upon the inclusion of a fourth parameter, Θ, as described in Section 5.3.4.

Table 5-9: Summary of how the final model input parameters are obtained for the current model of FO

Parameter	Method
r_{pore}	Obtained from fitting with RO data, as described in Section 5.3.1
Δx	Obtained from fitting with RO data, as described in Section 5.3.1
$L_{support}$	Obtained from fitting with respect to FO data
K_d	Obtained from correlations (cf. Section 5.3.1 and Appendix D)
K_c	0

The values of active layer geometric parameters shown in Section 5.3 are fitted based on hindered transport theory. The hindered transport theory assumes low intra-pore Reynolds number and therefore the Stokes equation governs water flow in the pore (88). The Stokes radius is therefore the natural choice for the definition of ion radius. The Stokes radius of an ion is generally smaller than its hydrated radius (97). Therefore, a smaller value of pore radius will be fitted when the Stokes radius is used for a given set of experimental data. In Ref. (87), uncharged solutes were used for fitting the pore radius of the HTI CTA membrane. Since the Stokes radii of all uncharged

solutes used in that study were larger than those of sodium and chloride, their fitted values of pore radius were found to be larger than those in the current work. If those values of pore radii were used in the modeling of sodium chloride, the removal of the convective mode of transport would not be sufficient to result in model validation, and the charge and dielectric exclusion effects would need to be incorporated. However, in that case, it would not be possible to achieve validation for both RO and FO using a unique set of fitting parameters. Thus, the approach of removing convection and using the Stokes radii of sodium and chloride for fitting allows for the simplest method of validation of RO and FO using the same set of fitting parameters.

5.6.3. Justification of the physics of no convective coupling in FO

As a consequence of the removal of the convective coupling effect on solute transport, the model reduces to a pore-based model with diffusion-dominated transport, similar to the conclusions of Yaroschuk et al. (73,74). However, in the current work, model agreement was better for RO when convective coupling was included, compared to the traditional SD model. Indeed, the current model with convection allows better fitting with the experimental data in Tang et al. (15) than the modeling results obtained from the traditional SD method used in that work. For the FO case, however, validation of the model was not possible when convection was included. The requirement for no convective coupling between the water and solute fluxes in FO could be due to the absence of the pressure-driven effects (that exist in RO and NF). In other words, convective coupling maybe a consequence of the pressurized mode. The presence of convective coupling as a result of applied pressure is hypothesized by Kook et al. (98). Those authors suggest that membrane deformation occurs upon application of pressure beyond a certain yield limit, thereby magnifying the effect of membrane free volume and allowing the water to carry solute with its flow (convective coupling). Another possibility is that the effects of convective coupling, if any, in FO would be

better accounted for by a more sophisticated model such as the Maxwell-Stefan model. While Paul (83) examines this model for RO and concludes that there may be convective coupling in RO, no such examination has been done for FO, to the best of our knowledge. The implementation of the Maxwell-Stefan approach for FO would allow one to account for interactions between each solute species, which may be more significant in FO than RO due to the opposite directions of water and solute flux in this mode.

5.7. Chapter 5 conclusion

5.7.1. Summary

In this work, a generalized pore flow model that has been widely implemented for NF (3,25,26,29), is extended to two other water-purification techniques, namely RO and FO. RO and FO membranes, unlike those for NF, are generally considered non-porous and solute flux in these membranes is modeled as diffusion-dominated (13,15). Recent experimental work as well as molecular dynamics studies, however, indicate RO and FO membranes have free voids (11,82). Based on traditional modeling approaches, the concept of diffusion-dominated transport and existence of pores are considered mutually exclusive. In this work, it is concluded that these two apparently disparate theories are in fact, reconcilable. We show that both RO and FO can be successfully modeled using a porous-membrane based model. The difference between the two modes is in the occurrence of convective coupling between water and solute fluxes (present in RO, absent in FO). As shown in Section 5.3.3.1, the model in RO mode (pore-based model with convection) agrees with the experimental data even better than the traditional SD model despite requiring only two fitting parameters. These results on RO are in agreement with the recent work of Kook et al (98), who suggest that inclusion of convection is necessary to account for transport

of solutes through the membrane in a pressurized state. However, the model must be reduced to a diffusion-dominated pore flow model for successful validation in the FO mode.

From a modeling perspective, the defining feature of the traditional pore flow models is the presence of convective coupling between solute transport and water transport (hence the existence of pores implies convective coupling and vice versa). On the other hand, the traditional definition of SD is that the transport is diffusion-dominated and there are no distinct pores in the membrane. The current work concludes that it is possible to have a porous membrane in which ion transport may or may not be diffusion-dominated depending on the mode of operation of the membrane. Thus, an outlook to FO modeling similar to the generalized SD model introduced by Yaroshchuk is preferable (73,74). This generalized SD approach accounts for various exclusion mechanisms, including steric and charge-based, by means of phenomenological coefficients. The approach of generalized SD thus considers diffusion-dominated transport while also allowing for membrane porosity and charge-based transport and exclusion effects, in contrast to the traditional SD approach which considers only non-porous membranes with concentration-gradient driven transport. The pore flow approach developed in the current work therefore paints the same picture of the physics inside the membrane but is implemented differently from a mathematical perspective. Finally, incorporation of tortuosity improved the model's agreement with experimental results for FO. The proposed model is of intermediate mathematical complexity between molecular dynamics and solution-diffusion. A summary of the various approaches to modeling solute flux in membranes is provided in Fig. 5-12. It is shown that the existence of pores in RO/FO membranes is not in contradiction to diffusion-dominated transport if the generalized SD model is considered.

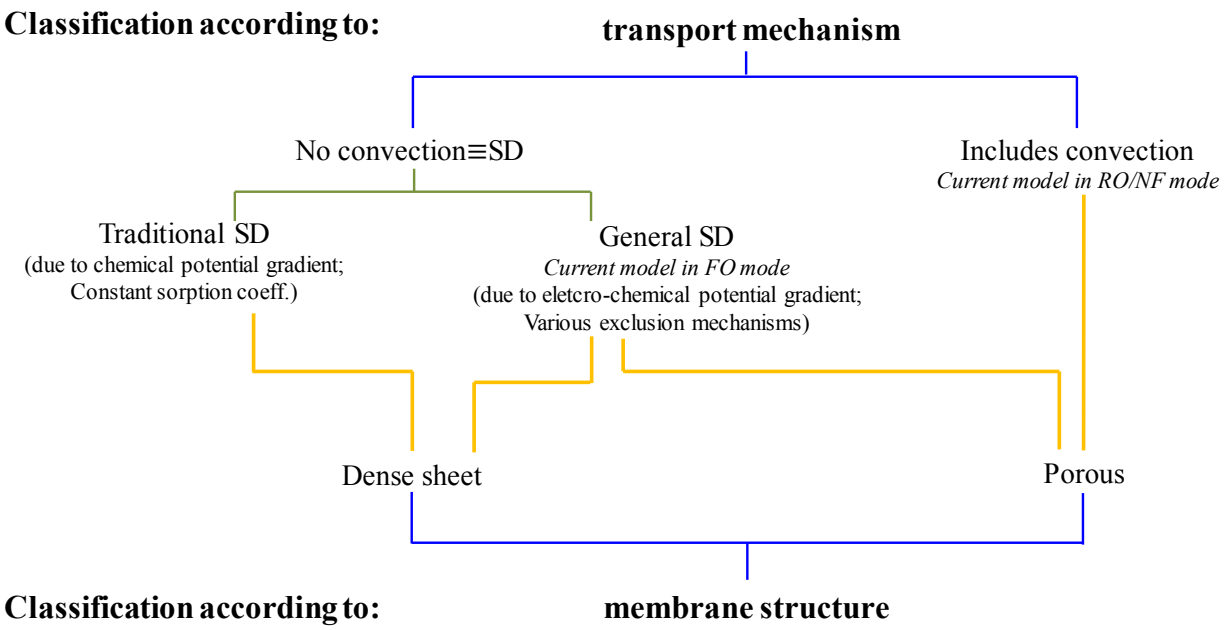

Figure 5-12. The different classifications of transport in membranes and their connection with the various classifications of membrane structure is summarized. While the presence of convection implies a porous membrane, a porous membrane does not necessarily imply convective solute transport.

5.7.2. Concluding remarks

The salient features of the current model and the key findings from the analysis are summarized below:

1) Generality: The model described above offers a general framework for species transport in FO and RO membranes; the model allows for three possible modes of transport (diffusion, convection and electromigration) without explicit assumptions about the relative contributions of each of the mechanisms. Furthermore, compared to solution–diffusion, this model is able to incorporate several realistic characteristics of the membrane, such as the existence of free voids (pores) and the membrane active layer thickness and support layer thickness Thus, the current modeling strategy sits between the basic solution–

diffusion and highly complex molecular dynamics approaches in terms of its fidelity in modeling physical phenomena.

2) Emergence of solution–diffusion for FO: Even though the model captures various modes of species transport within the membrane, comparison with experimental data reveals that the dominant mode of solute transport in the FO configuration is diffusion. Convective coupling in FO may be better accounted for by a more sophisticated modeling approach that the Extended Nernst-Planck equation, such as the Maxwell-Stefan approach. Using the current modeling approach, however, it was found that the RO model fit experimental data notably better when convective coupling existed, compared to the traditional SD model.
3) Suitability for membrane design: The proposed model relates membrane performance to geometric membrane properties and therefore enables design of new membranes with optimized performance in FO and RO applications.
4) Improved choice and number of fitting parameters: As described in Section 5.3.1, the independent fitting parameters in the case of RO are the membrane pore radius and effective active layer thickness. For modeling FO, the three independent fitting parameters are the pore radius, effective active layer thickness, support layer thickness and tortuosity (Section 5.3.4). It was also shown that the active layer fitting parameters obtained for RO can be used for FO, thus requiring only the additional fitting of FO-specific parameters in that mode (L_s and Θ). In contrast to the solution–diffusion model which uses phenomenological permeability coefficients, the current model uses parameters that reflect membrane geometry. Furthermore, the number of phenomenological coefficients used in models such as solution–diffusion scales with the number of independent solute species, which is not the case in the current model, where a fixed number of membrane-specific

parameters are used. Although in this work we have not considered salts with multivalent ions, it is possible in those cases that the effect of the charge-based fitting parameters will be more critical for model validation. Under those circumstances, the number of fitting parameters would be increased, but would still be directly related to a membrane property rather than individual phenomenological coefficients for each ion as would be necessary for SD.

5) Independent modeling of individual ions: The model allows for the independent modeling of each ion while simultaneously respecting electro-neutrality. This feature allows the user to analyze the effects of different membrane parameters and modes of operation (FO/RO/NF) on the transport of specific ions. It is noteworthy that the approach of using the Maxwell-Stefan equations as done by Paul (83) accounts for interactions between individual ions as well as between the ions and solvent molecules. However, the implementation of this approach is complicated by the requirement for the experimental determination of frictional coupling factors accounting for each type of interaction (83). Hence this approach is not considered in the current work, which aims to not only provide insight into transport mechanisms but also a practically useful model for membrane scientists. Furthermore, the conclusion of no convective coupling in FO might be relaxed if the Maxwell-Stefan model is better able to account for the inter-species interactions.
6) Explicit modeling of the partitioning effect: The model incorporates a detailed model of partitioning at the boundaries of the active layer. The combination of steric and Donnan partitioning have been included in the current model in order to capture the most important exclusion mechanisms of the membrane. In contrast, solution–diffusion lumps all exclusion effects into one enigmatic coefficient that is not necessarily independent of

solution properties. The partitioning equations of the proposed model allow for prediction of membrane performance across a wide range of solution compositions, without needing to introduce individual fitted parameters for each solute species.

6. The Effect of Increased Top Brine Temperature on the Performance and Design of OT-MSF Using a Case Study

6.1. Introduction

Multi-Stage-Flash (MSF) desalination was the dominant method of large-scale desalination at the advent of desalination technology in the 1960s (99,100). Since that time, it has given way to reverse osmosis (RO) and Multi-Effect-Distillation (MED), which emerged as the two other major large-scale desalination technologies. However, MSF has retained an important status especially in the Middle East and North Africa (MENA), where it occupies 86.7% of the desalination capacity as of 2005 (100). There are clear reasons for it to remain in this position: MSF plants are integrated with power plants to produce both water and electricity; plant operation is unaffected by high feed temperature, salinity, and turbidity and requires minimal manual intervention; and they have long life-times up to 30 years (99). Optimization of MSF performance and identification of design and operational strategies to reduce capital and operational costs thus remain quite important.

Although Brine-Recirculation MSF (BR-MSF) plants are the state of the art MSF technology, Once-Through MSF (OT-MSF) systems serve as a good starting point for analysis of the effect of top brine temperature (TBT) on MSF performance due to their relative simplicity. Furthermore, although OT-MSF plants have been studied widely (101)(102)(103)(104), the effect of increased TBT on required specific heat transfer area (sA) has not been investigated in detail. Although authors have studied the effect of TBT on OT-MSF performance ratio (PR) and sA, they have not considered important aspects that are covered in the current work. For example, in the work by El-Dessouky and Ettouney (104), the authors investigate the effect of TBT on performance ratio (PR)

up to 110ºC. The main development of the current work over that of El-Dessouky and Ettouney is in the significantly increased range of TBT studied which is important, given that NF and other pretreatment for MSF have shown potential to increase TBT up to 160ºC (105)or even 175ºC (106). Studies as recent as 2016 have also discussed design and performance of OT-MSF, indicating the ongoing interest in this field. For example, the work of Hanshik et al. (107) looks into the effect of higher TBT on other aspects of MSF design such as distillate production rate, cooling seawater outlet temperature, electrical power needed for pumps and heating energy required in the brine heater. They do not, however, look into the specific area requirements. Furthermore, they consider a fixed number of stages, and hence higher TBT is attained by changing ΔT at a fixed number of stages. As shown later in the current work, the effect of changing ΔT for a fixed number of stages on PR is much smaller than keeping a fixed ΔT and varying the number of stages. The work of Bandi et al. (108) is a complex cost optimization study on three configurations of MSF, including OT-MSF however it does not look explicitly at the effect of TBT on sA.

The TBT in an MSF plant is restricted by scale formation in the brine heater, especially since scalants such as calcium-sulfate ($CaSO_4$) and calcium-carbonate ($CaCO_3$) exhibit reduced solubility with increase in temperature(109). MSF plants in the Kingdom of Saudi Arabia typically have TBT between 90ºC and 115ºC and performance ratio (PR) between 6.5 and 9.5 (110,111). The reduction of scaling ions would allow a higher TBT and hence an increase of the flashing range and PR in MSF.

Researchers have identified TBT as one of the most dominant parameters determining the performance of MSF (102)(112). Fiorini and Sciubba (112) noticed from a thermo-economic analysis of an MSF plant that the TBT is the most important parameter governing the plant

operation, since it affects both plant performance and cost of steam. They recommended operation at the highest possible TBT. In the work of Tanvir and Mujtaba (113) the authors assume a fixed TBT of 90^{o}C and observe that since seawater temperature inevitably increases during the summer, the temperature driving force and recovery ratio of MSF unavoidably declines in this season. If the plant is instead operated at higher TBT in all seasons, the fluctuation of plant-performance with temperature can be mitigated.

Pretreatment of the incoming feed seawater by nanofiltration (NF) is a well-established means to attain high TBT in MSF. A series of studies performed by the SWCC (Saline Water Conversion Corporation) (111)(105)(114)(24)(115)(116)(117)(118) since the late 1990s describe the two hybrid NF-MSF schemes: one where NF product is the MSF feed, and one where the MSF feed is SWRO (seawater reverse osmosis) reject, which in turn was pretreated with NF. In pilots of both configurations, the MSF TBT reached 130°C, the system design limit, without scale formation in the brine heater; theoretical studies show the potential for a TBT up to 160°C. Al-Rawajfeh (106) theoretically investigated pretreatment with NF, and estimated that a TBT up to 175°C could be reached with a TDS reduction of 37-38%. Mabrouk (119) piloted a CSP (Concentrated Solar Power)-powered NF-MSF system with a TBT of 100°C, reaching a GOR of 15. This work on NF-MSF also showed that the reduction in MSF energy consumption at higher TBT (130°C) outweighs the additional capital cost of the NF pretreatment.

To date, the literature has focused on the hybridization of NF with BR-MSF (105)(114), which dominates installed capacity. The primary advantage of BR-MSF over OT-MSF is its lower consumption of chemical additives to prevent scaling per unit distillate, while its primary setback is the large specific pumping power required to recirculate the brine. If NF can truly replace chemical pretreatment, the advantages of the OT variant – its lower specific pumping power

requirements in particular – become more attractive. This is supported by the study by Tusel et al. (120) on an OT-MSF plant in Sirte, in which the authors mention that although OT-MSF plants were almost entirely switched to BR-MSF plants by the 1970s, the reasons for the switch were reversed by the 1990s due to the emergence of reasonably priced corrosion-resistant materials and cost-effective antiscalants that can withstand high temperature. Thus the costs relating to additional parts such as major pumps and valves in BR-MSF currently outweigh its advantages, especially in the Arabian Peninsula where the high salinity of incoming seawater leads to a small difference in recovery ratio between the two configurations and thus the lower specific-pumping power of the OT-MSF arrangement is reason to prefer this system.

Several researchers are studying novel nanofiltration membranes, such as the composite nanofiltration membrane with a chemically crosslinked rGO laminate film acting as an ion-selective barrier created by Zhang et al. (121) and the low pressure nanofiltration membranes created by researchers in Singapore (26). The work by Roy et al. (25) introduced comprehensive modeling of large-scale NF modules and included an analysis of flat-sheet and spiral-wound modules. Their model allows the user to vary membrane parameters and thus model various kinds of NF membranes under various operating conditions. These developments indicate that as nanofiltration membranes continue to improve, there is impetus for improvement in NF-thermal desalination hybrids.

In this work, the effect of increasing the TBT of once-through MSF on performance ratio (PR) and required specific area (sA) is investigated. The study first considers the effect of increasing the TBT for a plant with a fixed brine exit temperature (T_{end}) and inter-stage temperature (ΔT) drop by successively adding more stages. Subsequently, the effect of varying the brine exit temperature for a fixed TBT and inter-stage temperature drop is considered, thereby capturing the effect of

seasonal and diurnal variations in incoming feed water temperature at different TBT values. These two modes of analysis are then applied to a case study of the OT-MSF plant in Sirte (120) to investigate the effect of increasing its TBT up to182^{o}C, in order to determine if plant performance can be improved beyond that of the current operation. To the best of the authors' knowledge, investigating the effect of increased TBT on the specific surface area requirement has received little attention for OT-MSF systems.

6.2. Mathematical Model

Figure 6-1 shows a schematic diagram of the Once-Through Multi-Stage Flash system (OT-MSF) investigated. The system contains a brine heater and several stages, each consisting of a feed heater and flashing chamber. The governing equations for this system are given in this section.

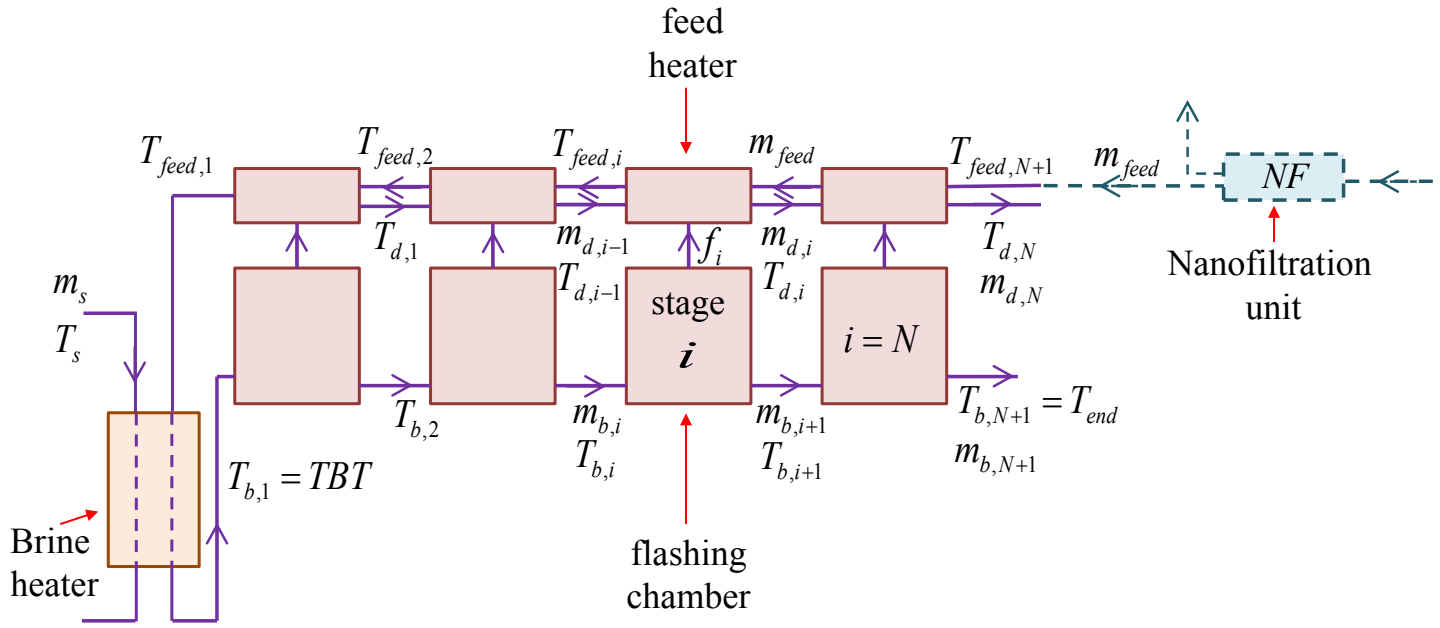

Figure 6-1: Schematic diagram of OT-MSF system

6.2.1. Brine heater energy balance

$$m_{feed}(h_{b,1} - h_{feed,1}) - m_s L_s = 0 \tag{6-1}$$

where m_{feed} is the feed mass flow rate entering the MSF system (the permeate flow rate exiting from the NF unit), m_s is the mass flow rate of steam, L_s is the latent heat of vaporization of the steam, and $h_{feed,1}$ and $h_{b,1}$ are the enthalpies for saturated liquid corresponding to the temperatures $T_{feed,1}$ and $T_{b,1}$ as shown in Fig. 6-1. In this work, $h_{feed,i}$ is calculated by $h_{feed,i} = C_p T_{feed,i}$ where C_p is 4.18kJ/kg-K. For calculation of enthalpies, the reference state is taken at $T_{ref} = 273.15K = 0\,^{o}\text{C}$ so that $h_{ref} = 0$kJ/kg. The variation of C_p with feed temperature is neglected, since going from 25°C to 160°C, more than 100°C increase in temperature, the heat capacity of water changes by only 4%. While attaining high top brine temperature (TBT), it is necessary to pressurize the feed to a pressure slightly above the corresponding saturation pressure in order for flashing to occur upon entering the first evaporator. Thus, although the enthalpy of the heated feed exiting the brine heater is $h(T_{b,1}, P = P_{sat} + \Delta P)$, there is negligible difference of this value with $h(T_{b,1}, P = P_{sat})$. In the current model, the enthalpy of the feed exiting the brine heater is considered to be $h(T_{b,1}, x = 0)$.

6.2.2. Evaporator energy balance

For stages 1 to N

$$m_{b,i+1} h_{b,i+1,x=0} - m_{b,i} h_{b,i,x=0} + f_i h_{v,i} = 0 \tag{6-2}$$

where f_i is the mass flow rate of flashed vapor in stage i, $m_{b,i} = m_{feed} - \sum_{j=1}^{i-1} f_j$ is the brine mass flow rate entering stage i, and $h_{v,i}$ is enthalpy of the flashed vapor in stage i ($h_{v,i} = h(T_{b,i+1}, x = 1)$, is the enthalpy at temperature $T_{b,i+1}$, with quality x=1).

6.2.3. Evaporator salt balance

For stages 1 to N

$$m_{b,i+1} y_{b,i+1} - m_{b,i} y_{b,i} = 0 \tag{6-3}$$

where $y_{b,i}$ is salinity of brine entering stage i and $m_{b,i} = m_{feed} - \sum_{j=1}^{i-1} f_j$ is the brine mass flow rate entering stage i.

6.2.4. Feed heater energy balance

$$m_{feed}\left(h_{feed,i} - h_{feed,i+1}\right) + m_{d,i} h_{d,i,x=0} - m_{d,i-1} h_{d,i-1,x=0} - f_i h_{v,i} = 0 \tag{6-4}$$

where $m_{d,i} = \sum_{j=1}^{i} f_j$ is the mass flow rate of distillate exiting stage i and $h_{d,i}$ is the corresponding distillate enthalpy. The (pure) distillate temperature is given by

$$T_{d,i} = T_{b,i+1} - \delta \tag{6-5}$$

where δ is the boiling point elevation.

The interstage temperature drop is assumed to be constant and is given by

$$\Delta T = \left(\frac{T_{b,1} - T_{b,N+1}}{N} \right) \tag{6-6}$$

The surface area required for heat exchange in each feed heater is calculated using an overall heat transfer coefficient obtained by considering the water-side and steam-side heat transfer coefficients

in series. The water-side heat transfer coefficient is given by Eqn. 6-7 (122), while the steam-side heat transfer coefficient is considered to be 7000 W/m^2-K throughout the range of temperature considered. This is justified by the fact that, as per Fig. 6-3 in the work by Baig et al. (122), the heat transfer coefficient on the steam-side varies by only ~8% from 100^{o}C to 150^{o}C and can be considered almost constant with increase in temperature:

$$h^{\bullet}_{water-side} = (0.656u)^{0.8}\left(\frac{d_{in}}{d_{out}}\right)\left(\frac{3293.5 + T_{feed}(84.24 - 0.1714T_{feed}) - y_{feed}(8.471 + 0.1161y_{feed} + 0.2716T_{feed})}{\left(d_{in}\left(\frac{100}{1.7272}\right)\right)^{0.2}}\right) \quad (6\text{-}7)$$

In Eqn. 6-7, T_{feed} is the feed temperature in the stage under consideration. Further, d_{in} and d_{out} are the internal and external diameters of the tubes carrying the feed water during preheating and are taken as 16 mm and 16.5 mm respectively (120).

The required heat exchange area of the feed heater in the given stage is now calculated using the LMTD as follows:

$$A_i = \frac{m_{feed} C_p (T_{feed,i} - T_{feed,i+1})}{U_i LMTD_i} \quad (6\text{-}8)$$

where

$$LMTD_i = \frac{(\Delta T_{1,LMTD} - \Delta T_{2,LMTD})}{\ln\left(\frac{\Delta T_{1,LMTD}}{\Delta T_{2,LMTD}}\right)} \quad (6\text{-}9)$$

and

$$\Delta T_{1,LMTD} = (T_{d,i} - T_{feed,i+1}) \quad (6\text{-}10a)$$

$$\Delta T_{2,LMTD} = (T_{d,i-1} - T_{feed,i}) \quad (6\text{-}10b)$$

Using a similar procedure, the heat transfer surface area requirement in the brine heater is given by:

$$A_{bh} = \frac{m_{feed} C_p (T_{b,1} - T_{feed,1})}{U_{bh} LMTD_{bh}} \tag{6-11}$$

in which the overall heat transfer coefficient in the brine heater U_{bh} is considered to be constant at 3000 W/m^2-K, as per Fig. 6-4 in the work of Baig et al. (122), where the overall heat transfer coefficient in the brine heater is approximately 3000W/m^2-K from 80^{o}C to 140^{o}C (varying by 8.4% over this range of temperature).

Finally, the required specific area (sA) and performance ratio (PR) are given by:

$$sA = \left(\frac{\sum_{i=1}^{N} A_i + A_{bh}}{m_{d,N}} \right) \tag{6-12}$$

$$PR = \frac{m_{d,N}}{m_s} \tag{6-13}$$

6.3. Validation

The model is validated against an analytical model by El-Dessouky and Ettouney (104). For a 24 stage OT-MSF plant with top brine temperature TBT = 106^{o}C, incoming seawater temperature of 25^{o}C,brine reject temperature T_{end} of 40^{o}C, and seawater salinity 42000 mg/kg, El-Dessouky and Ettouney (104) (case study 6.4.3) report a performance ratio (PR) of 3.96 whereas the current model predicts a PR of 3.97, a deviation of 0.25% from the reference. Figure 6-2a shows the brine salinity and feed temperature across all the stages in the reference and in the present model. The

figure indicates a very good agreement between the current model and the reference with a maximum deviation of 0.49% and 0.39% for the brine salinity and feed temperature, respectively. Validation is also done in reference to Fig. 4a in Baig et al. (102) (cf. Fig. 2b in the current work), observing the effect of inter-stage temperature drop ΔT on the PR for a fixed number of stages (N=24 and N=32). The maximum deviation between the reference and current work was found to be 2.4% and 1.7% for N=24 and N=32, respectively.

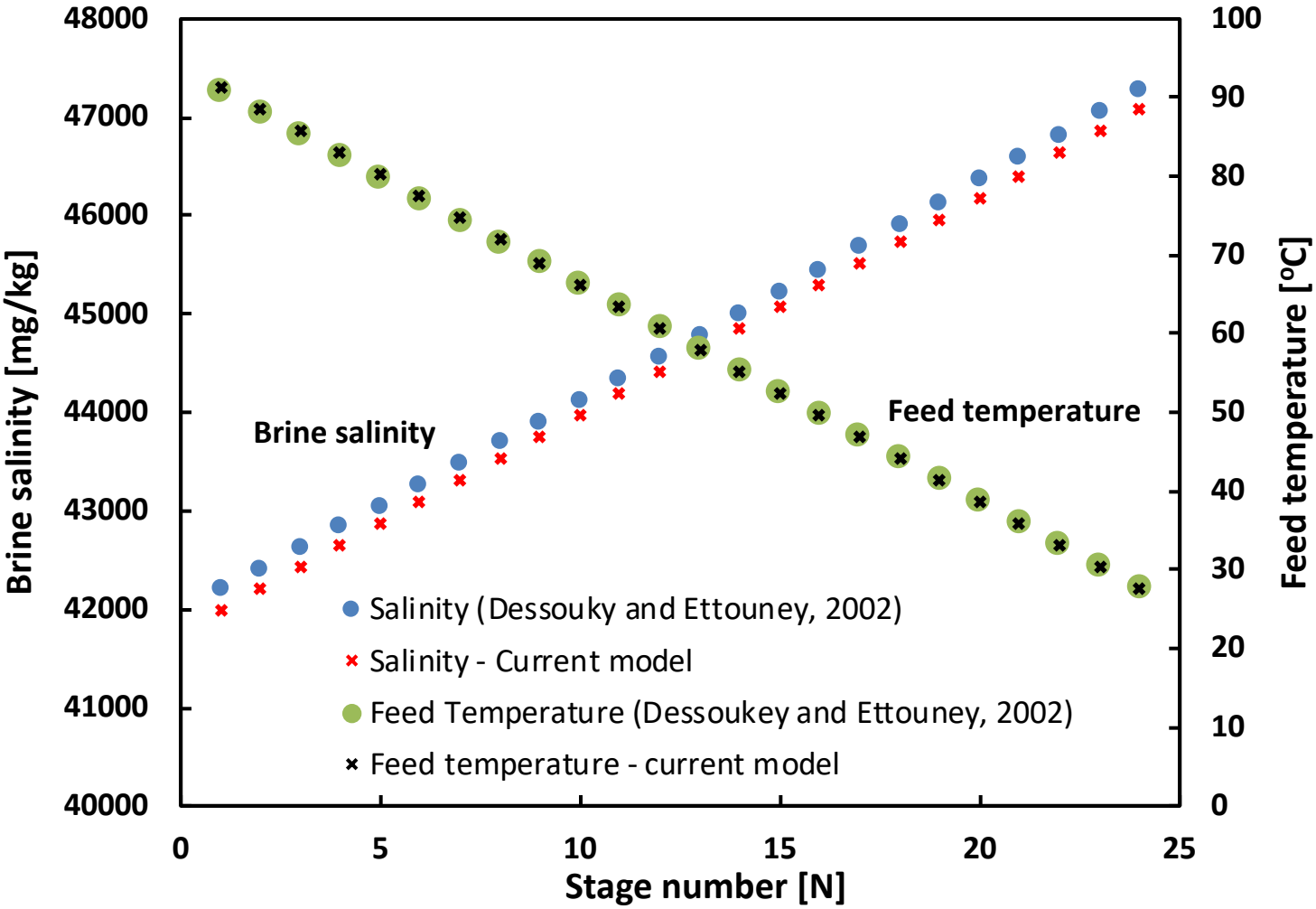

Figure 6-2a. A stage-wise comparison of brine salinities and feed temperatures between El-Dessouky and Ettouney (104) and the present work shows good agreement, with maximum deviations of 0.49% and 0.39%, respectively.

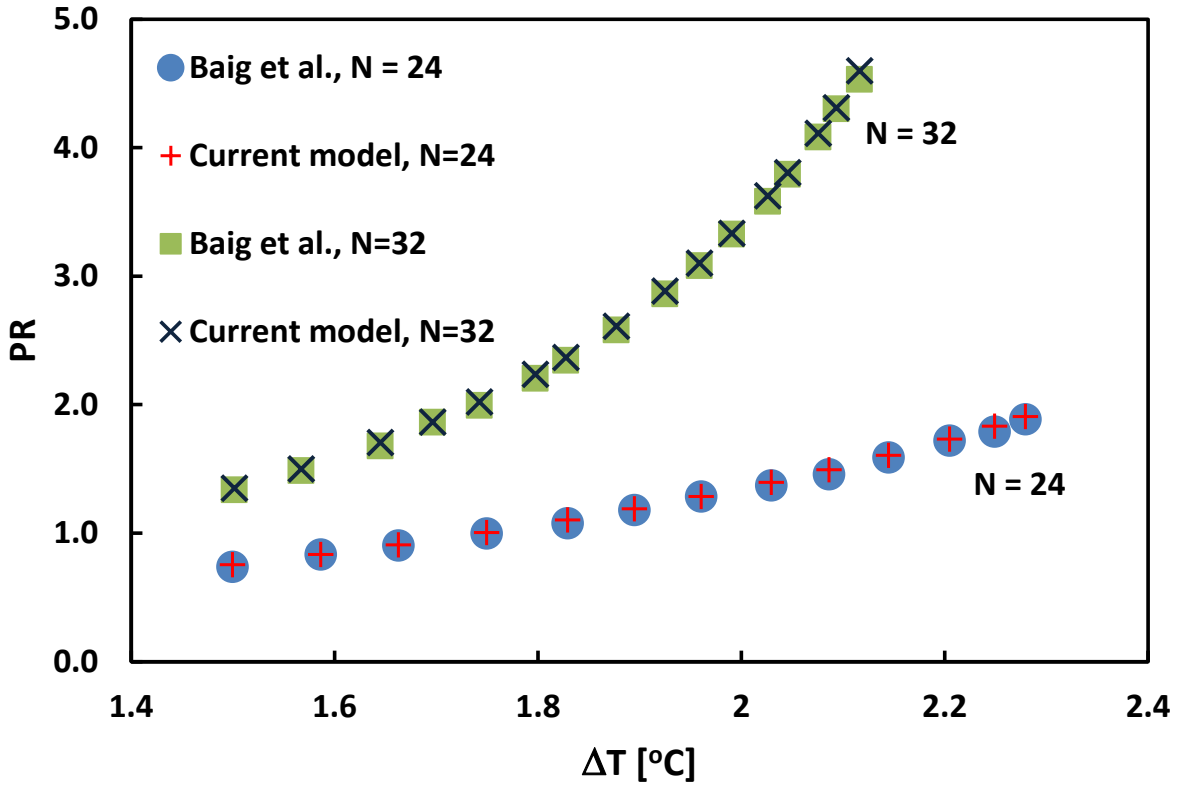

Figure 6-2b. Validation with Baig et al. [4] for the effect of inter-stage temperature drop ΔT on the PR for a fixed number of stages (N=24 and N=32) shows a maximum deviation between the reference and current work to be 2.4% and 1.7% for N=24 and N=32, respectively.

6.4. Results and Discussion

6.4.1. Effect of increased TBT on OT-MSF performance.

Figure 3 shows the variation of the performance ratio (PR) and the specific heat transfer area required (sA) when the TBT is increased by increasing the number of stages and keeping ΔT and T_{end} fixed. Similar to the case study by El-Dessouky and Ettouney(104) considered in the validation section, the brine reject temperature is fixed at 40°C, seawater inlet temperature and mass flow rate are taken as 25°C and 3384 kg/s respectively, the steam temperature is kept 10°C above the TBT and a boiling point elevation of ~1°C is considered in the evaporators. Three values of inter-stage temperature drop 2°C, 2.4°C and 3°C are considered for the parametric study. The figure shows that increasing the TBT has the effect of monotonically increasing the PR for all values of ΔT used, over the given range of TBT considered. The trend of variation of PR with TBT appears linear but is in fact non-linear, which becomes clear especially at temperatures beyond 150°C. Referring to Eqn. 6-13, the reason is that, although the variation of $m_{d,N}$ with TBT is linear, the variation of m_s is non-linear, such that the slope increases with TBT (concave upward). The reason for such variation of m_s is further explained from Eqn. 6-1: the term $m_{feed}(h_{b,1} - h_{feed,1})$ is almost constant with increase in TBT while L_s varies non-linearly such that the slope decreases with increasing TBT (concave downward). Thus, since $m_s \propto \frac{1}{L_s}$, its variation with TBT is also non-linear, but with slope increasing with TBT (opposite curvature to variation of L_s).

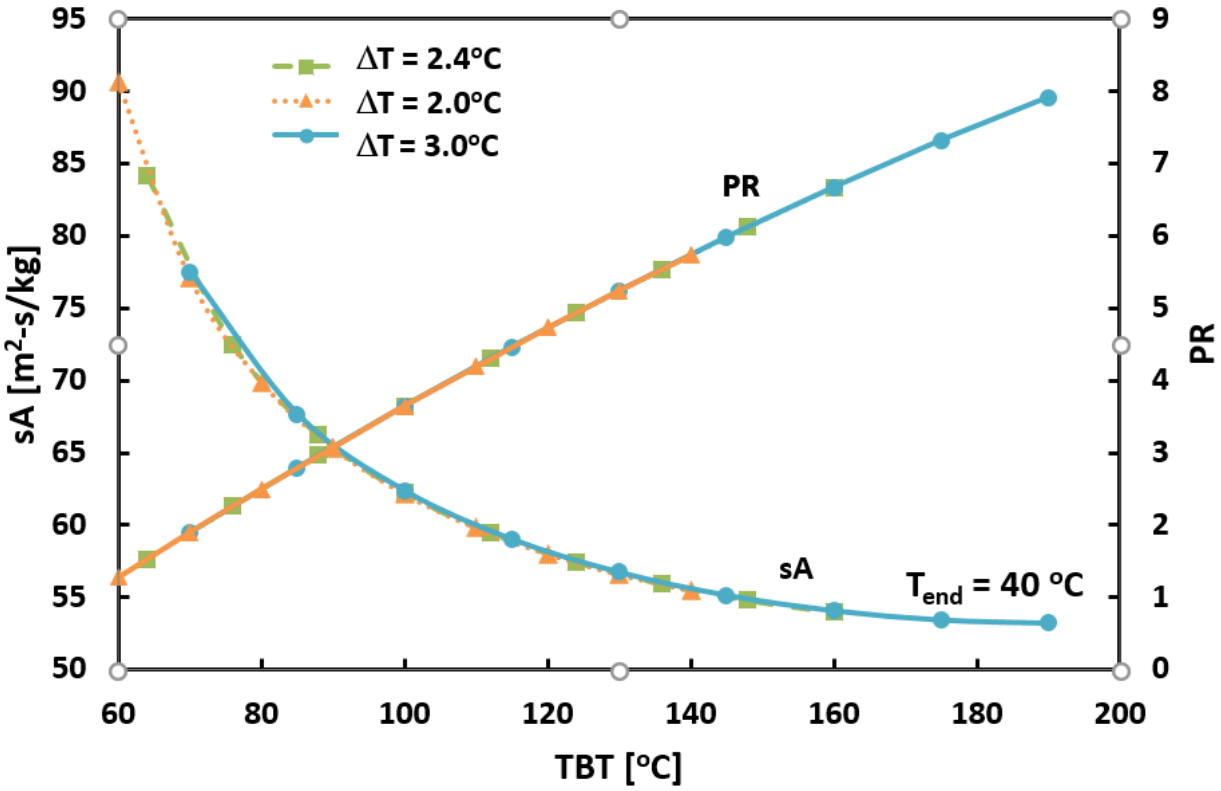

Figure 6-3: Effect of increasing TBT on the PR and sA by adjusting the number of stages when the brine reject temperature and ΔT are fixed. It is seen that the PR increases almost linearly with increase in TBT while the sA decreases and its rate of decrease becomes smaller with increase in TBT.

On the other hand, the sA monotonically decreases over the given range of TBT, but its rate of decrease is less as a higher TBT is approached. This trend in the sA is explained by the nature of variation of total area with increase in TBT. Although the distillate production increases linearly with TBT, the variation of total area with increase in TBT is not linear and there is a small increase in the slope of increase of the total area with TBT. This feature is attributed to the variation of LMTD with increase in TBT.

At all values of ΔT considered, the PR at a TBT of 160°C is ~6.67 (68% higher than that in the case study by El-Dessouky and Ettouney(104), which considered TBT = 106°C and N = 24) and the number of stages required is 60 and 50 for the lowest and highest ΔT considered. Since a

different correlation for heat transfer coefficient (which can be extended to higher TBT) was used for the present work rather than that used in the work of El-Dessouky and Ettouney(104), the value of sA is significantly different from that reported in reference [6]. The correlation used by El-Dessouky and Ettouney gives a value of overall heat transfer coefficient ~2000 W/m^2-K over the range of temperature studied while the current correlations give a value of 3000-4500 W/m^2-K depending on the stage of MSF considered. Furthermore, the upper limit of temperature for the heat transfer coefficient used by El-Dessouky and Ettouney is 110^{o}C as per Appendix C in the reference (104).

From an analysis of PR and sA, the overall recommendation referring to Fig. 3 is to operate the OT-MSF at an intermediate value of TBT so as to maximize PR such that increasing the TBT any further provides diminishing returns. Further, it is recommended to use the lowest value of ΔT that will balance the trade-off between the negative aspects i.e. increased number of stages and lowered PR, with the beneficial aspect of the decreased sA requirement at lower ΔT.

6.4.2. Effect of reduced brine reject temperature on OT-MSF performance

Figure 4 shows the effect of increasing the number of stages (N) at constant TBT and ΔT on the PR and sA by adjusting the brine reject temperature T_{end}. TBT values of 120^{o}C, 140^{o}C and 160^{o}C are considered and ΔT is fixed at 2^{o}C. At lower values of N the values of T_{end} are higher, which implies that a corresponding amount of thermal energy is rejected to the environment during brine rejection. If the number of stages is increased, this energy could be harnessed to increase distillate production and the brine would be rejected at a lower temperature. Such an increase in the number of stages provides the advantage of an increased performance ratio but requires increased specific heat transfer area. It is seen from Fig. 4 that at the lowest TBT of 120^{o}C, decreasing the brine reject temperature from 38^{o}C to 30^{o}C increases the PR by almost threefold from 5.57 to 15.9,

the penalty being that the sA increases almost three times from 65.21 m^2-s/kg to 181.17 m^2-s/kg. The corresponding increase in number of stages is from 41 to 45. At the highest TBT of 160°C, the same drop in brine reject temperature causes, again, a threefold increase in PR from 7.8 to 21.8 while the sA increases by a factor of three, from 61.66 m^2-s/kg to 191.09 m^2-s/kg. The number of stages increases from 61 to 65. As seen from Fig. 4, at a higher TBT, for a given value of T_{end}, PR is higher. Furthermore, while at lower T_{end}, sA is highest for the highest TBT, the trend is inverted for higher T_{end} values.

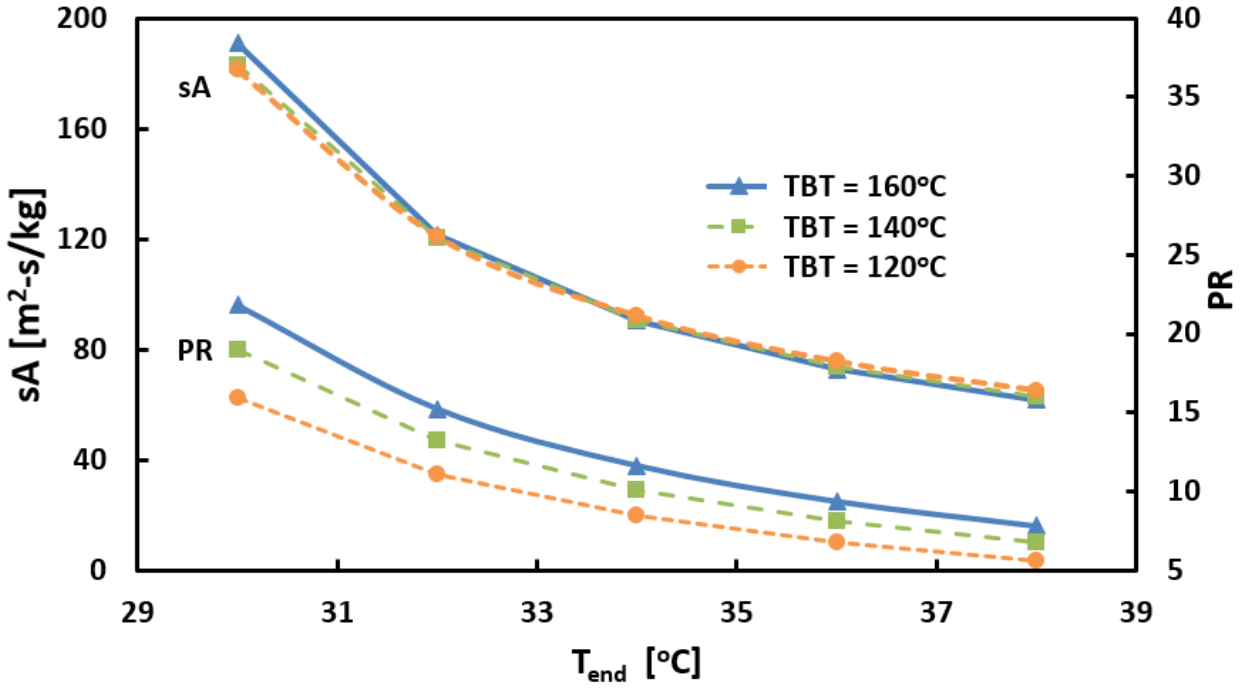

Figure 6-4: Variation of PR when brine reject temperature T_{end} is varied by adjusting the number of stages, keeping TBT and ΔT fixed. It is seen that at a higher TBT, for a given value of T_{end}, PR is higher. While at lower T_{end}, sA is highest for the highest TBT, the trend is inverted for higher T_{end} values.

Practically, T_{end} varies when seawater inlet temperature varies due to factors such as weather change. In areas of cooler weather, it would be beneficial to operate a larger number of stages and select an optimal value of TBT such that the sA requirement and increase in PR are balanced. A

larger number of stages for a given TBT will also allow the brine reject temperature to be as close to the environmental temperature as possible, while keeping ΔT small. As mentioned in case 4.1, the ΔT should be kept at an optimal value so that it is not too large to cause larger sA requirement but also large enough to not require too large a number of stages. In all cases, however, a significant improvement in PR is observed with increasing TBT while incurring a relatively small penalty in sA. This suggests that operation at higher TBT irrespective of environmental temperature is energetically favorable.

6.4.3. Case Study: Effect of increased TBT on Sirte OT-MSF plant

In light of the preceding discussions, the effect of increased TBT by adding stages is studied on an existing OT-MSF plant operating in Sirte. The OT-MSF system described by Tusel et al. (120), 1994 has a TBT of 118^{o}C with 39 stages, ΔT = 2.07^{o}C and operates at a PR of 10. As a starting point, the current operating condition of the Sirte plant is used to validate our model. Figure 5 shows the anticipated change in its PR and required sA if the TBT is increased by increasing the number of stages, keeping the ΔT and brine reject temperature fixed at the original values. As mentioned in section 6.4.1, although the PR increases monotonically with number of stages and hence TBT, the sA poses a restriction by showing a minimum at an intermediate value of TBT. The cause for this trend in the sA can be described similarly to that described in section 6.4.1 and is due to the non-linear variation of total area with TBT such that its slope increases with increase in TBT, hence forming an arc. Thus, the sA, defined as the ratio between total area and distillate production (which varies linearly with TBT) is non-linear and shows a minimum with TBT. As shown in Fig. 5, the red dotted line shows the current performance of the Sirte plant whereas the blue dotted line shows the predicted performance at a TBT of 161.6^{o}C, when 60 stages are employed. At this TBT, the sA curve begins to rise and hence is a good choice of the optimal

operating point. Compared to the original operating conditions, the PR increased by 41.5% to 14.64, while the sA requirement and steam mass flow rate increased by 0.9% and ~5% respectively. These numbers indicate that the penalties of the increased TBT are relatively low and if the shift in the steam extraction point in the power plant is not problematic, operation at elevated TBT is shown to be advantageous. At 70 stages, where a TBT of 182.3°C is attained, although the PR has further increased to 16.52, the sA has increased by 5.7% compared to the current operating conditions. It is, however, worth keeping in mind that the heat exchanger tubes contribute to about 18% of plant capital cost (99), which would help in estimating the additional cost associated with increased number of stages.

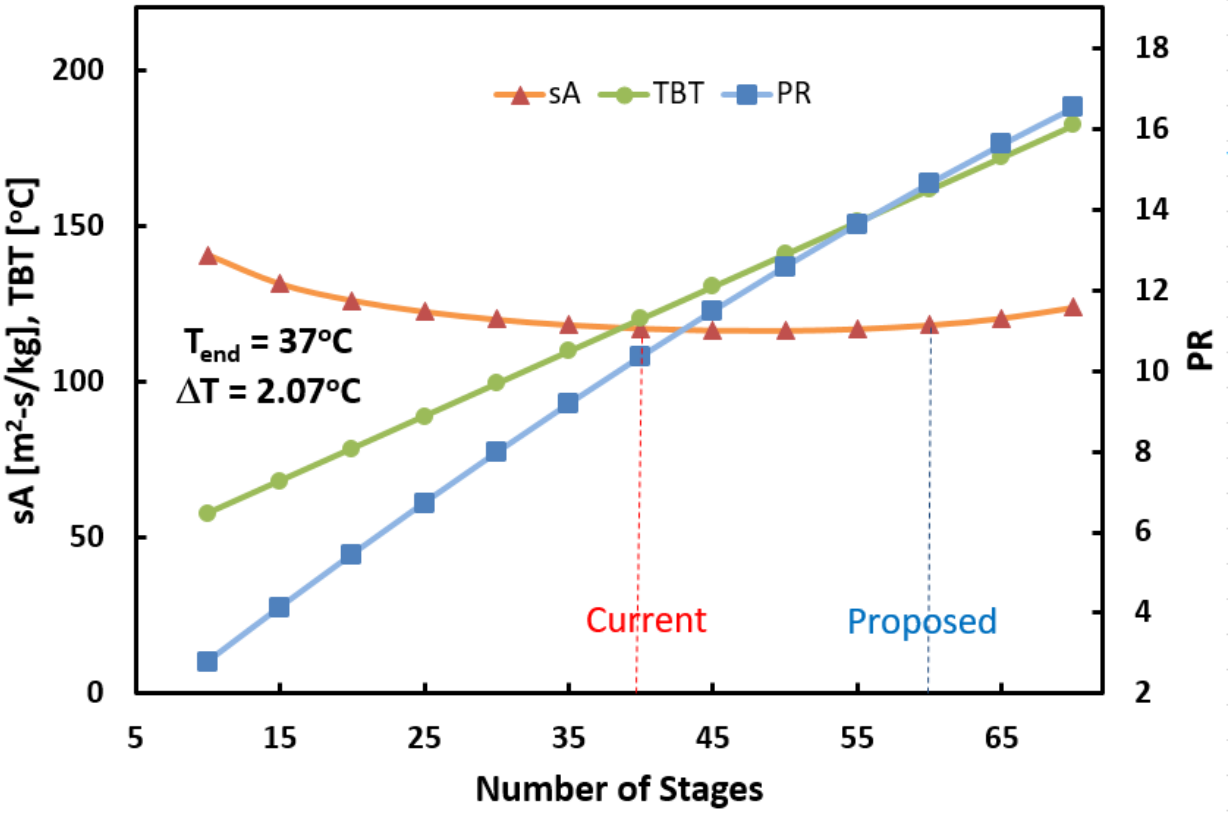

Figure 6-5. Variation of PR and required sA if the TBT of the Sirte plant is increased by increasing the number of stages, keeping the ΔT and brine reject temperature fixed. The red dotted line represents the current performance of the plant, with a TBT of 118°C and 39 stages. The blue dotted line shows the predicted performance at a TBT of 161.6°C and 60 stages, at which

point the PR is increased by 41.5% compared to the current operation while the sA requirement increased by 0.9%, thereby showing that there is a possibility of increasing plant PR with a relatively small compromise in sA requirement.

Figure 6-6 shows the effect of varying the brine reject temperature T_{end} on PR at fixed TBT and ΔT, by adjusting the number of stages. At TBT=118^{o}C i.e. the usual operating temperature of Sirte, decreasing T_{end} from 40^{o}C to 32^{o}C increased the PR almost 6 times while the required number of stages increased from 39 to 43. At a TBT of 160^{o}C the increase in PR due to the same change in T_{end} was similar as that seen for TBT=118^{o}C and the required number of stages increased from 60 to 64. As mentioned previously, T_{end} is a function of inlet feed temperature, which depends on environmental temperature. Thus the study of the variation in T_{end} reflects the plant performance in different seasons or over the span of a day. The relatively small change in the required number of stages with change in T_{end} indicates that the number of operational effects does not need to be changed with seasonal or diurnal temperature variation for optimal plant performance at a given TBT. However, at par with the discussion in section 6.4.2, it is also seen that when T_{end} is lower, the sA is higher and increases rapidly with decreasing T_{end}, thereby indicating that at cooler weather conditions, the plant may not be able to operate optimally due to the increased heat exchange area requirement.

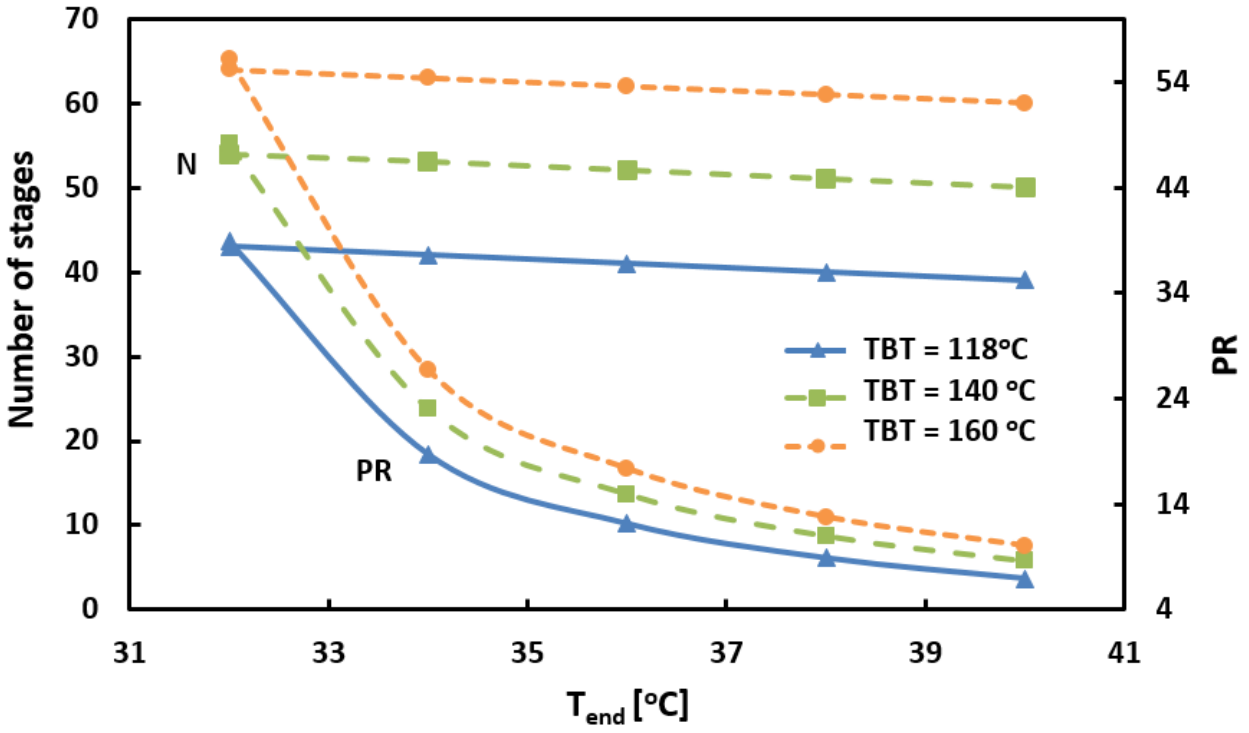

Figure 6-6: The effect of varying the brine reject temperature T_{end} on PR at fixed TBT and ΔT, by adjusting the number of stages.

6.5. Chapter 6 conclusions

The effect of increasing the top brine temperature (TBT) on the performance and design characteristics of an OT-MSF plant has been investigated by observing the performance ratio (PR) and the specific area requirement (sA) at higher TBT and also how these values change due to seasonal variation. The end goal is to determine whether an existing OT-MSF plant would perform better at higher TBT and to suggest changes in its design and operation by suggesting an optimal value of TBT and ΔT within the constraints of environmental conditions.

The conclusions of the study are as follows:

1. For a fixed inter-stage temperature drop ΔT and brine reject temperature T_{end}, if number of stages N is increased, thereby increasing TBT, the performance ratio PR increases

monotonically with N (and hence TBT) whereas sA decreases such that beyond a certain value of TBT, the change in sA with TBT is negligibly small. As seen in Fig. 6-5, if the TBT is allowed to increase even further, the sA will begin to increase again. Thus, an OT-MSF plant should be operated at the optimal TBT where PR is high and sA is minimum. The inter-stage temperature drop must also be kept at an intermediate value, since at higher ΔT, there is the penalty of higher sA, although it should not be too small in order to avoid a large number of stages required to attain the required TBT.

2. When the TBT and ΔT are fixed and the number of stages is increased to reduce T_{end}, the PR and sA are both found to increase sharply. It is seen that at a higher TBT, for a given value of T_{end}, N and PR are each higher. While at lower T_{end}, sA is highest for the highest TBT, the trend is inverted for higher T_{end} values. Thus, for practical purposes, an intermediate value of TBT should be chosen so that the maximum advantage of increased PR can be taken without suffering a high penalty of increased specific area. Furthermore, for cooler regions, an OT-MSF plant should be designed consisting of a larger number of stages than usually used in hotter regions so that the ΔT can be minimized and the brine reject temperature can be kept as close to the environmental temperature as possible.
3. There is potential to improve the PR of the existing Sirte plant in Libya by increasing the TBT to 160^{o}C, keeping all other operational conditions unchanged. At this TBT, PR is expected to increase by 41.5% from the existing value to 14.64, while the sA requirement increases by 0.9%, which is a relatively small penalty.

7. Thesis conclusions

The major conclusions based on this thesis are as follows:

1. Total ion transport and individual modes of transport in nanofiltration (NF) increase with increasing temperature.
2. Membrane properties show clear trends of variation with temperature: pore size, net path length and magnitude of negative membrane charge increase with increase in temperature. These changes cumulatively affect permeate quality in NF significantly. At higher applied pressures, the net effect of membrane parameters increasingly dominates that of mobilities.
3. Changes in membrane geometric properties at higher temperature lower permeate quality (increased permeate concentration) while change in membrane charge improves permeate quality. Therefore, for higher temperature applications, focus on restricting membrane restructuring is advisable.
4. The selectivity between monovalent and multivalent ions deteriorates at higher temperature. This decrease in selectivity applies to all pairs of monovalent-multivalent species as long as the flux of the multivalent species is lower at the original temperature.
5. Reverse osmosis (RO) and forward osmosis (FO) membranes can be modeled as porous. However, the key distinction between the two is in the presence of pressure-induced convective coupling in RO, which is absent in FO.
6. The inclusion of NF as a pretreatment to thermal desalination, such as Multi-Stage-Flash (MSF) allows for increased energetic efficiency with relatively low increase in specific surface area (indicating plant capital costs) to the MSF plant.

Appendix A: Membrane structural parameters at different temperatures

Membrane structural parameters at different temperatures from the fitting by Amar et al. (22):

Parameter	r_{pore} [nm]	$\Delta x / A_k$ [µm] (solute)	$\Delta x / A_k$ [µm] (water)
22°C	0.58	0.98	2.20
40°C	0.59	0.46	2.11
50°C	0.67	0.56	2.67

Appendix B: Structural properties used for fractionation modeling

Nanofiltration membrane structural change with temperature:

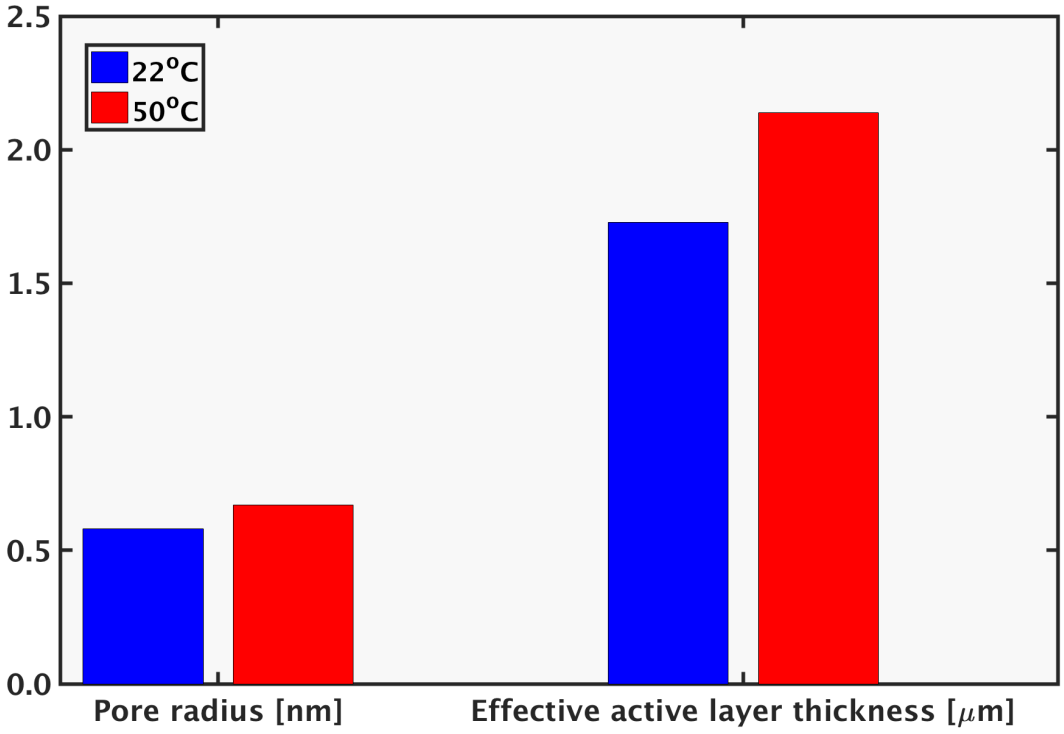

As explained in detail in references (57,65), membrane pore radius and the effective path length (tortuosity) through the membrane increase with increase in temperature.

Appendix C: Derivation of the boundary layer equation:

The mass balance equation for external concentration polarization is given by Eq. C.1 (2,29):

$$J_i = -k_i\left(C_{m,i} - C_{f,i}\right) + J_w C_{m,i} - z_i C_{m,i} D_{\infty,i} \frac{F}{RT}\zeta \tag{C.1}$$

In a salt containing two ions,

$$z_{i1}J_{i1} = z_{i2}J_{i2} = \mathbb{J} \tag{C.2}$$

Multiplying Eq. C.1 for both ions by their respective valencies,

$$z_{i1}J_{i1} = -z_{i1}k_{i1}\left(C_{m,i1} - C_{f,i1}\right) + z_{i1}J_w C_{m,i1} - z_{i1}z_{i1}C_{m,i1}D_{\infty,i1}\frac{F}{RT}\zeta \tag{C.3a}$$

$$z_{i2}J_{i2} = -z_{i2}k_{i2}\left(C_{m,i2} - C_{f,i2}\right) + z_{i2}J_w C_{m,i2} - z_{i2}z_{i2}C_{m,i2}D_{\infty,i2}\frac{F}{RT}\zeta \tag{C.3b}$$

Subtracting Eq. C.3b from C.3a, and using C.2,

$$\begin{aligned} -z_{i1}k_{i1}\left(C_{m,i1} - C_{f,i1}\right) + z_{i1}J_w C_{m,i1} - z_{i1}z_{i1}C_{m,i1}D_{\infty,i1}\frac{F}{RT}\zeta + z_{i2}k_{i2}\left(C_{m,i2} - C_{f,i2}\right) \\ - z_{i2}J_w C_{m,i2} + z_{i2}z_{i2}C_{m,i2}D_{\infty,i2}\frac{F}{RT}\zeta = 0 \end{aligned} \tag{C.4}$$

$$\begin{aligned} -z_{i1}k_{i1}\left(C_{m,i1} - C_{f,i1}\right) + z_{i1}J_w C_{m,i1} + z_{i2}k_{i2}\left(C_{m,i2} - C_{f,i2}\right) - z_{i2}J_w C_{m,i2} \\ + \zeta\frac{F}{RT}\left(z_{i2}z_{i2}C_{m,i2}D_{\infty,i2} - z_{i1}z_{i1}C_{m,i1}D_{\infty,i1}\right) = 0 \end{aligned} \tag{C.5}$$

Similar to the relation between ion fluxes (Eq. C.2), the relationship between concentrations is given by:

$$z_{i1}C_{i1} = z_{i2}C_{i2} = \mathbb{C} \tag{C.6}$$

Therefore, Eq. C.5 can be re-written as:

$$-\left(k_{i,1} - k_{i,2}\right)\left(\mathbb{C}_m - \mathbb{C}_f\right) = \mathbb{C}_m\left(z_{i,1}D_{\infty,i1} - z_{i,2}D_{\infty,i2}\right)\frac{F}{RT}\zeta \tag{C.7}$$

$$\Rightarrow \zeta = \frac{-\left(k_{i,1} - k_{i,2}\right)\left(\mathbb{C}_m - \mathbb{C}_f\right)}{\mathbb{C}_m\left(z_{i,1}D_{\infty,i1} - z_{i,2}D_{\infty,i2}\right)\frac{F}{RT}} \tag{C.8}$$

Substituting into Eq. C.3a,

$$\mathbb{J} = -k_{i1}\left(\mathbb{C}_m - \mathbb{C}_f\right) + J_w\mathbb{C} + z_{i1}\mathbb{C}_m D_{\infty,i1}\frac{F}{RT}\frac{\left(k_{i,1} - k_{i,2}\right)\left(\mathbb{C}_m - \mathbb{C}_f\right)}{\mathbb{C}_m\left(z_{i,1}D_{\infty,i1} - z_{i,2}D_{\infty,i2}\right)\frac{F}{RT}} \tag{C.9}$$

$$\Rightarrow \mathbb{J} = -k_{i1}\left(\mathbb{C}_m - \mathbb{C}_f\right) + J_w\mathbb{C}_m + z_{i1}D_{\infty,i1}\frac{\left(k_{i,1} - k_{i,2}\right)\left(\mathbb{C}_m - \mathbb{C}_f\right)}{\left(z_{i,1}D_{\infty,i1} - z_{i,2}D_{\infty,i2}\right)} \tag{C.10}$$

$$\Rightarrow \mathbb{J} = -\frac{\left(k_{i1}z_{i2}D_{i2} + k_{i2}z_{i1}D_{\infty,1}\right)}{\left(z_{i,1}D_{\infty,i1} - z_{i,2}D_{\infty,i2}\right)}\left(\mathbb{C}_m - \mathbb{C}_f\right) + J_w\mathbb{C}_m \tag{C.11}$$

$$\Rightarrow \mathbb{J} = -\mathbb{K}_{eff}\left(\mathbb{C}_m - \mathbb{C}_f\right) + J_w\mathbb{C}_m \tag{C.12}$$

J_s is obtained by dividing $\mathbb{J}$ by the larger ion valency,

$$\Rightarrow J_s = -K_{eff}(C_{m,s} - C_{f,s}) + J_w C_{m,s} \tag{4-6a}$$

Appendix D: Hindrance factors and steric partitioning factor

Expressions for the diffusive and convective hindrance coefficients as a function of $\left(\frac{r_i}{r_{pore}}\right)$ are given below. For convenience, $\lambda_i = \left(\frac{r_i}{r_{pore}}\right)$ is used. The value of r_{pore} is fixed from the RO fitting at 0.205 nm.

For $\lambda_i \leq 0.95$ (29),

$$K_{i,d} = \left(\frac{1 + (9/8)\lambda_i \ln\lambda_i - 1.56034\lambda_i + 0.528155\lambda_i^2 + 1.91521\lambda_i^3 - 2.81903\lambda_i^4 + 0.270788\lambda_i^5 - 1.10115\lambda_i^6 - 0.435933\lambda_i^7}{\Phi_i} \right) \tag{D.1}$$

and for $\lambda_i > 0.95$ (29),

$$K_{i,d} = 0.984\left(\frac{1-\lambda_i}{\lambda_i}\right)^{5/2} \tag{D.2}$$

For convection, the hindrance factor for $\lambda_i \in [0, 1]$ is (29):

$$K_{i,c} = \left(\frac{1+3.867\lambda_i - 1.907\lambda_i^2 - 0.834\lambda_i^3}{1+1.867\lambda_i - 0.741\lambda_i^2}\right) \tag{D.3}$$

The expression for the steric partitioning factor is given by:

$$\Phi_i = (1-\lambda_i)^2 \tag{D.4}$$

Appendix E: Procedure to fit membrane geometric parameters for RO and FO

The fitting procedure for pore radius and effective active layer thickness in RO is described here. The experimental bulk feed concentration, bulk permeate concentration, water permeability, water flux and rejection ratio values are inputs to the fitting code. As mentioned in Section 5.3.1, the code is provided with a possible set of pore radius values and at each of these values, it calculates the extent of concentration polarization, and hence finds the effective pressure difference across the membrane. The optimal effective active layer thickness for a given pore radius is then calculated using the value of effective pressure difference thus obtained by rearranging Eq. 5-13a. In the current fitting method, the deviation between the model prediction and experimental values for solvent flux and rejection ratio is calculated using the absolute value of the fractional deviation, as in the following equations:

$$d_{Rej}^k(\omega) = \left|\frac{Rej_{\text{model}}^k(\omega) - Rej_{\text{expt}}^k}{Rej_{\text{expt}}^k}\right| \text{ and } \; d_{J_w}^k(\omega) = \left|\frac{J_{w,\text{model}}^k(\omega) - J_{w,\text{expt}}^k}{J_{w,\text{expt}}^k}\right|, \tag{E.1}$$

where $d_{Rej}^{k}(\omega)$ and $d_{J_w}^{k}(\omega)$ are the fractional deviations between the model prediction (at different values of the membrane parameter to be fitted, ω, at each data point, k) and experimentally obtained values, for the rejection ratio (Rej) and solvent flux (J_w) respectively. For the procedure to fit pore radius, ω represents pore radius.

In general, the fractional deviation in the water flux and that of the rejection ratio could be different by an order of magnitude. Thus, adding the values of d_{Rej}^{k} and $d_{\mathrm{J_w}}^{k}$ as given by Eq. E.1 may not allow for both sets of error to be given equal weight in determining the optimal membrane parameter values. Indeed, if the fractional deviations for the rejection ratio and water flux are simply added together, a higher weight would be given to the quantity (rejection ratio or water flux) whose error magnitude is larger. To equalize the contributions of both the rejection ratio and water flux in minimizing the net error for each data point, the fractional deviation for each quantity is scaled by the mean value over all model runs (across the N_k data points and N_ω values of pore radius (for the procedure to fit pore radius, ω represents pore radius).

$$d_{Rej}^{k\prime}(\omega) = \frac{d_{Rej}^{k}(\omega)}{\left(\frac{\sum_{k,\omega} d_{Rej}^{k}(\omega)}{N_k \times N_\omega}\right)} \tag{E.2}$$

$$d_{J_w}^{k\prime}(\omega) = \frac{d_{J_w}^{k}(\omega)}{\left(\frac{\sum_{k,\omega} d_{J_w}^{k}(\omega)}{N_k \times N_\omega}\right)} \tag{E.3}$$

The equations E.2. and E.3. represent two matrices, such that when the matrices are plotted as meshes, both lie within the same range and intersect. Due to the similar ranges of error values for

both rejection ratio and water flux, the fitting method ensures that the optimal pore radius gives the best possible fit with both water flux and rejection, over all data points. These normalized fractional deviations for rejection ratio and water flux, as given by Eqs. E.2 and E.3, respectively, are then summed to arrive at the final expression for the net error (net deviation), which is the objective function to be minimized (Eq. E.4). Further details of the fitting procedure is given in Reference (123)

$$d'(\omega) = \sum_{k}^{N=6} d_{Rej}^{k\prime}(\omega) + d_{J_w}^{k\prime}(\omega). \tag{E.4}$$

For fitting the support layer structural parameter, the solute and solvent fluxes in FO are used, instead of the rejection ratio and solvent flux as done for RO. However, the formulation of the error function is the same as shown above.

Appendix F : Difference between effective diffusion and flow distances

To illustrate why the effective length for solute diffusion and solvent flow might differ, a membrane with a pore network equivalent to a bundle of bent or angled tubes with length $\tau\delta$ is considered. As in the Carman-Kozeny Equation (see Ref. (96)), the solvent flow rate per unit area through a bundle of tubes with tortuosity τ is proportional to τ^{-2}:

$$J_w = \left(\frac{r_{pore}^2 \varphi}{8\nu\rho_w \delta\tau^2}\right)\left((P_f - P_p) - \Delta\pi\right). \tag{F.1}$$

Solvent flux is inversely proportional to the square of tortuosity because tortuosity affects both solvent flow speed in the pore and the length of the flow path. Equation 5-13c is equivalent to Eq. 5-13a for the following definition of effective flow length:

$$\Delta x_{eff,f} = \frac{\delta \tau^2}{\varphi}. \tag{F.2}$$

In a porous medium, the path length for diffusion is also increased relative to a uniform medium due to the convoluted structure of the free volume. Furthermore, the area for flow by diffusion is reduced compared to a uniform medium. As a result of these two effects, the effective length for solute diffusion through a bundle of tubes constituting a membrane with porosity φ and tortuosity τ is:

$$\Delta x_{eff,d} = \frac{\delta \tau}{\varphi} = \frac{\Delta x_{eff,f}}{\tau}. \tag{F.3}$$

A bundle of tortuous tubes does not precisely align with the active layer geometry all FO or RO membranes. However, it does illustrate a limitation of the assumption that $\Delta x_{eff,f} = \Delta x_{eff,d}$. In order to make a more general adaptation to the DSPM model, an effective thickness ratio Θ is defined in Eq. F.4.:

$$\Theta = \frac{\Delta x_{eff,f}}{\Delta x_{eff,d}}. \tag{F.4}$$

τ and Θ are equal in the bundle-of-tubes model, but real membranes are not bundles of tubes, so Θ may be used to more generally capture differences between effective path lengths for diffusion and flow real membrane active layers. In Section 5.3.4, the effect of treating Θ as an additional fitting parameter that accounts for the differing effect of membrane pore geometry on diffusion and flow will be explored.

Appendix G: Role of $K_{i,d}$ to validate the FO model

For the sake of completeness an attempt to validate with experimental FO data from Ref. (15) by refitting $K_{i,d}$ must be discussed. An extensive number of trials were conducted to refit $K_{i,d}$ when $K_{i,c}$ is fixed at values obtained from correlations (as presented in Table 5-4), and when both $K_{i,c}$ and $K_{i,d}$ are refitted simultaneously, with no marked improvement. Furthermore, no physically plausible best-fit values for the $K_{i,d}$ exist other than those obtained from the correlation; in contrast, the finding of good agreement at $K_{i,c} = 0$ aligns with the transition to SD theory. Finally, the successful validation of the model as shown in Section 5.3.5 using only a fitted value of L_s and a value of $K_{i,c}$ as prescribed by the physics of FO indicates that the model can be very simply matched with experiments once the correct physics is accounted for.

8. References

1. Eriksson P. Nanofiltration extends the range of membrane filtration. Environ Prog [Internet]. 1988;7(1):58–62. Available from: http://onlinelibrary.wiley.com/wol1/doi/10.1002/ep.3300070116/abstract
2. Roy Y, Sharqawy MH, Lienhard JH. Modeling of flat-sheet and spiral-wound nanofiltration configurations and its application in seawater nanofiltration. J Memb Sci. 2015;493.
3. Bowen WR, Welfoot JS. Modelling the performance of membrane nanofiltration — critical assessment and model development. Chem Eng Sci. 2002;57(7):1121–37.
4. Roy Y, Warsinger DM, Lienhard JH. Effect of temperature on ion transport in nanofiltration membranes: Diffusion, convection and electromigration. Desalination. 2017;420:241–57.
5. Hashim A, Hajjaj M. Impact of desalination plants fluid effluents on the integrity of seawater , with the Arabian Gulf in perspective. Desalination. 2005;182:373–93.
6. Mezhoud N, Temimi M, Zhao J, Al Shehhi MR, Ghedira H. Analysis of the spatio-temporal variability of seawater quality in the southeastern Arabian Gulf. Mar Pollut Bull [Internet]. 2016;106(1–2):127–38. Available from: http://dx.doi.org/10.1016/j.marpolbul.2016.03.016
7. Gao J, Sun SP, Zhu WP, Chung TS. Green modification of outer selective P84 nanofiltration (NF) hollow fiber membranes for cadmium removal. J Memb Sci. 2016;499:361–9.
8. Chai X, Chen G, Yue P-L, Mi Y. Pilot scale membrane separation of electroplating waste water by reverse osmosis. J Memb Sci. 1997;123:235–42.
9. Schaep J, Van der Bruggen B, Uytterhoeven S, Croux R, Vandecasteele C, Wilms D, et al. Removal of hardness from groundwater by nanofiltration1. Desalination. 1998;119(1–3):295–301.
10. Mänttäri M, Pihlajamäki A, Kaipainen E, Nyström M. Effect of temperature and membrane pre-treatment by pressure on the filtration properties of nanofiltration membranes. Desalination. 2002;145(1–3):81–6.
11. Fujioka T, Oshima N, Suzuki R, Price WE, Nghiem LD. Probing the internal structure of reverse osmosis membranes by positron annihilation spectroscopy: Gaining more insight into the transport of water and small solutes. J Memb Sci [Internet]. 2015;486:106–18. Available from: http://dx.doi.org/10.1016/j.memsci.2015.02.007
12. Kurihara M, Sasaki T, Nakatsuji K, Kimura M, Henmi M. Low pressure SWRO membrane for desalination in the Mega-ton Water System. Desalination [Internet]. 2015;368:135–9. Available from: http://dx.doi.org/10.1016/j.desal.2015.02.037
13. McCutcheon JR, Elimelech M. Influence of concentrative and dilutive internal concentration polarization on flux behavior in forward osmosis. J Memb Sci. 2006;284:237–47.
14. Banchik LD, Sharqawy MH, Lienhard JH. Effectiveness-mass transfer units (ε - MTU) model of a reverse osmosis membrane mass exchanger. J Memb Sci [Internet]. 2014;458:189–98. Available from: http://dx.doi.org/10.1016/j.memsci.2014.01.039
15. Tang CY, She Q, Lay WCL, Wang R, Fane AG. Coupled effects of internal concentration polarization and fouling on flux behavior of forward osmosis membranes during humic acid filtration. J Memb Sci. 2010;354(1–2):123–33.

16. Tow EW, Lienhard JH. Quantifying osmotic membrane fouling to enable comparisons across diverse processes. J Memb Sci [Internet]. 2016;511:92–107. Available from: http://dx.doi.org/10.1016/j.memsci.2016.03.040
17. Bowen WR, Welfoot JS. Modelling of membrane nanofiltration-pore size distribution effects. Chem Eng Sci. 2002;57(8):1393–407.
18. Hilal N, Al-Zoubi H, Darwish NA, Mohammad AW, Abu Arabi M. A comprehensive review of nanofiltration membranes: Treatment, pretreatment, modelling, and atomic force microscopy. Desalination. 2004;170(3):281–308.
19. Bowen WR, Cassey B, Jones P, Oatley DL. Modelling the performance of membrane nanofiltration - Application to an industrially relevant separation. J Memb Sci. 2004;242(1–2):211–20.
20. Oatley DL, Cassey B, Jones P, Bowen WR. Modelling the performance of membrane nanofiltration - Recovery of a high-value product from a process waste stream. Chem Eng Sci. 2005;60(7):1953–64.
21. Rautenbach R, Gröschl A. Separation potential of nanofiltration membranes. Desalination. 1990;77(C):73–84.
22. Ben Amar N, Saidani H, Deratani A, Palmeri J. Effect of temperature on the transport of water and neutral solutes across nanofiltration membranes. Langmuir. 2007;23(6):2937–52.
23. Snow MJH, de Winter D, Buckingham R, Campbell J, Wagner J. New techniques for extreme conditions: high temperature reverse osmosis and nanofiltration. Desalination [Internet]. 1996;105(1–2):57–61. Available from: http://www.sciencedirect.com/science/article/pii/0011916496000586
24. Al-Sofi MAK, Hassan AM, Hamad OA, Mustafa GM, Dalvi AGI, Kither MNM. Means and merits of higher temperature operation in dual-purpose plants. Desalination. 1999;125(1–3):213–22.
25. Roy Y, Sharqawy MH, Lienhard JH. Modeling of flat-sheet and spiral-wound nanofiltration configurations and its application in seawater nanofiltration. J Memb Sci. 2015;493:360–72.
26. Labban O, Liu C, Chong TH, Lienhard JH. Fundamentals of low-pressure nanofiltration: Membrane characterization, modeling, and understanding the multi-ionic interactions in water softening. J Memb Sci. 2017;521:18–32.
27. Muthumareeswaran MR, Alhoshan M, Agarwal GP. Ultrafiltration membrane for effective removal of chromium ions from potable water. Nat Publ Gr [Internet]. 2017;1–12. Available from: http://dx.doi.org/10.1038/srep41423
28. Levchenko S, Freger V. Breaking the Symmetry : Mitigating Scaling in Tertiary Treatment of Waste Effluents Using a Positively Charged Nano filtration Membrane. 2016;3–7.
29. Geraldes V, Brites Alves AM. Computer program for simulation of mass transport in nanofiltration membranes. J Memb Sci. 2008;321(2):172–82.
30. Bandini S, Vezzani D. Nanofiltration modeling: The role of dielectric exclusion in membrane characterization. Chem Eng Sci. 2003;58(15):3303–26.
31. Bowen WR, Mohammad AW. Diafiltration by nanofiltration: Prediction and optimization. AIChE J. 1998;44(8):1799–812.
32. Oatley DL, Llenas L, Pérez R, Williams PM, Martínez-Lladó X, Rovira M. Review of the dielectric properties of nanofiltration membranes and verification of the single oriented

layer approximation. Adv Colloid Interface Sci. 2012;173:1–11.
33. Kotrappanavar NS, Hussain AA, Abashar MEE, Al-Mutaz IS, Aminabhavi TM, Nadagouda MN. Prediction of physical properties of nanofiltration membranes for neutral and charged solutes. Desalination [Internet]. 2011;280(1–3):174–82. Available from: http://dx.doi.org/10.1016/j.desal.2011.07.007
34. Nilsson M, Tragardh G, Ostergren K. The influence of pH, salt and temperature on nanofiltration performance. J Memb Sci. 2008;312(1–2):97–106.
35. Anderson JL, Quinn JA. Restricted Transport in Small Pores. Biophys J [Internet]. 1974;14(2):130–50. Available from: http://dx.doi.org/10.1016/S0006-3495(74)70005-4
36. Anderson JL, Malone DM. Mechanism of osmotic flow in porous membranes. Biophys J. 1974;14(1):957–82.
37. Wang X, Tsuru T, Nakao S, Kimura S. Electrolyte transport through nanofiltration membranes by the space-charge model and the comparison with Teorell-Meyer- Sievers model. J Memb Sci. 1995;103(94):117–33.
38. Fang Y, Bian L, Bi Q, Li Q, Wang X. Evaluation of the pore size distribution of a forward osmosis membrane in three different ways. J Memb Sci [Internet]. 2014;454:390–7. Available from: http://dx.doi.org/10.1016/j.memsci.2013.12.046
39. Bowen WR, Mohammad AW. Characterization and Prediction of Nanofiltration Membrane Performance—A General Assessment. Chem Eng Res Des [Internet]. 1998;76(8):885–93. Available from: http://www.sciencedirect.com/science/article/pii/S0263876298717253
40. Higa M, Kira A, Tanioka A, Miyasaka K. Mixed Ionic Solution. 1993;89(18):3433–5.
41. Renou R, Ghoufi A, Szymczyk A, Zhu H, Neyt JC, Malfreyt P. Nanoconfined electrolyte solutions in porous hydrophilic silica membranes. J Phys Chem C. 2013;117(21):11017–27.
42. Beckstein O, Tai K, Sansom MSP. Not ions alone: Barriers to ion permeation in nanopores and channels. J Am Chem Soc. 2004;126(45):14694–5.
43. Yaroshchuk AE. Non-steric mechanisms of nanofiltration : superposition of Donnan and dielectric exclusion. Sep Purif Technol. 2001;23:143–58.
44. Kowalik-Klimczak A, Zalewski M, Gierycz P. Prediction of the chromium (III) separation from acidic salt solutions on nanofiltration membranes using donnan and steric partitioning pore (DSP) model. Archit Civ Eng Environ. 2016;9(3):135–40.
45. Huber ML, Perkins RA, Laesecke A, Friend DG, Sengers J V., Assael MJ, et al. New international formulation for the viscosity of H2O. J Phys Chem Ref Data. 2009;38(2):101–25.
46. Ong YK, Li FY, Sun SP, Zhao BW, Liang CZ, Chung TS. Nanofiltration hollow fiber membranes for textile wastewater treatment : Lab-scale and pilot-scale studies. Chem Eng Sci. 2014;114:51–7.
47. Yao L, Zhang L, Wang R, Chou S, Dong ZL. A new integrated approach for dye removal from wastewater by polyoxometalates functionalized membranes. J Hazard Mater [Internet]. 2016;301:462–70. Available from: http://dx.doi.org/10.1016/j.jhazmat.2015.09.027
48. WATER TECHNOLOGY FUTURES : A global blueprint for innovation. In: Singapore International Water Week. 2016.
49. Product Data Sheet DOW ™ Specialty Membrane XUS290508 and XUS290504 Nanofiltration Elements. 2016;

50. Bandini S, Morelli V. Effect of temperature, pH and composition on nanofiltration of mono/disaccharides: Experiments and modeling assessment. J Memb Sci. 2017;533(December 2016):57–74.
51. Sharma RR, Chellam S. Temperature and concentration effects on electrolyte transport across porous thin-film composite nanofiltration membranes: Pore transport mechanisms and energetics of permeation. J Colloid Interface Sci. 2006;298(1):327–40.
52. Ben N, Saidani H, Palmeri J, Deratani A. Effect of temperature on the rejection of neutral and charged solutes by Desal 5 DK nanofiltration membrane. Desalination [Internet]. 2009;246(1–3):294–303. Available from: http://dx.doi.org/10.1016/j.desal.2008.03.056
53. Lee KP, Bargeman G, Rooij R De, Kemperman AJB, Benes NE. Interfacial polymerization of cyanuric chloride and monomeric amines: pH resistant thin film composite polyamine nanofiltration membranes. J Memb Sci. 2017;523(September 2016):487–96.
54. Bowen W., Welfoot J., Williams PM. A linearised transport model for nanofiltration: development and assessment. AIChE J. 2002;48(4):760.
55. Saidani H, Amar N Ben, Palmeri J. Interplay between the Transport of Solutes Across Nanofiltration Membranes and the Thermal Properties of the Thin Active Layer. Langmuir. 2010;26(4):2574–83.
56. Roy Y, Warsinger DM, Lienhard JH. Effect of temperature on the solute transport in nanofiltration : diffusion, convection and electromigration. Desalination. 2017;420C:241–57.
57. Sharma R, Chellam S. Temperature effects on the transport of water, uncharged and charged solutes across polymeric nanofiltration membranes. In: American Water Works Association Membrane Technology Confernce. 2007. p. 17–20.
58. Dang HQ, Price WE. The effects of feed solution temperature on pore size and trace organic contaminant rejection by the nanofiltration membrane NF270. 2014;125:43–51.
59. Peeters JMM, Mulder MHV, Strathmann H. Streaming potential measurements as a characterization method for nanofiltration membranes. Colloids Surfaces A Physicochem Eng Asp [Internet]. 1999;150(1–3):247–59. Available from: http://www.sciencedirect.com/science/article/pii/S0927775798008280
60. Bargeman G, Steensma M, Kate A ten, Westerink JB, Demmer RLM, Bekkenes H, et al. Nanofiltration as energy-efficient solution for sulfate waste in vacuum salt production. Desalination [Internet]. 2009;245(1–3):460–8. Available from: http://dx.doi.org/10.1016/j.desal.2009.02.009
61. Curcio E, Ji X, Matin A, Barghi S, Profio G Di, Fontananova E, et al. Hybrid nanofiltration – membrane crystallization system for the treatment of sulfate wastes. J Memb Sci. 2010;360:493–8.
62. Mousavi SE, Ali SM, Jalali MM, Zahedi P, Karimi E. Sulfate removal from chlor-alkali brine using nanofiltration: Parameters investigation and optimization via Taguchi design method. Desalin Water Treat [Internet]. 2017;100(January):75–90. Available from: http://www.deswater.com/DWT_abstracts/vol_100/100_2017_67.pdf
63. Nagy E. A general, resistance-in-series, salt- and water flux models for forward osmosis and pressure-retarded osmosis for energy generation. J Memb Sci [Internet]. 2014;460:71–81. Available from: http://dx.doi.org/10.1016/j.memsci.2014.02.021
64. Sharma RR. Temperature Effects on the Morphology of Porous Thin Film Composite Nanofiltration Membranes. Environ Sci Technol. 2005;39(13):5022–30.

65. Roy Y, Lienhard JH. Investigation of the temperature-dependence of contributive factors in nanofiltration.
66. Hagmeyer G, Gimbel R. Modelling the salt rejection of nanofiltration membranes for ternary ion mixtures and for single salts at different pH values. Desalination. 1998;117(1–3):247–56.
67. Al-Rashdi BAM, Johnson DJ, Hilal N. Removal of heavy metal ions by nanofiltration. Desalination. 2013;315:2–17.
68. Lin J, Ye W, Zeng H, Yang H, Shen J, Darvishmanesh S, et al. Fractionation of direct dyes and salts in aqueous solution using loose nanofiltration membranes. J Memb Sci [Internet]. 2015;477:183–93. Available from: http://dx.doi.org/10.1016/j.memsci.2014.12.008
69. Tsuru T, Urairi M, Nakao S, Kimura S. Reverse osmosis of single and mixed electrolytes with charged membranes: experiment and analysis. J Chem Eng Japan. 1991;24(4):518–24.
70. Tsuru T, Nakao S, Kimura S. Calculation of ion rejection by extended Nernst-Planck equation with charged reverse osmosis membranes for single and mixed electrolyte solution. J Chem Eng Japan. 1991;24(4):511–7.
71. Wang X, Tsuru T, Togoh M, Nakao S, Kimura S. Evaluation of pore structure and electrical properties of nanofiltration membranes. Vol. 28, J. Chem. Eng. Japan. 1995. p. 186–91.
72. Wijmans JG, Baker RW. The solution-diffusion model : a review. J Memb Sci. 1995;107:1–21.
73. Yaroshchuk A, Martinez-lladó X, Llenas L, Rovira M, de Pablo J. Solution-diffusion-film model for the description of pressure-driven trans- membrane transfer of electrolyte mixtures : One dominant salt and trace ions. J Memb Sci. 2011;368:192–201.
74. Yaroshchuk A, Bruening ML. An analytical solution of the solution-diffusion-electromigration equations reproduces trends in ion rejections during nanofiltration of mixed electrolytes. J Memb Sci [Internet]. 2017;523:361–72. Available from: http://dx.doi.org/10.1016/j.memsci.2016.09.046
75. Matsuura T, Sourirajan S. Reverse Osmosis Transport through Capillary Pores under the Influence of Surface Forces. Ind Eng Chem Process Des Dev. 1981;20(2):273–82.
76. Mehdizadeh H, Dickson JM. Modeling of Reverse Osmosis in the Presence of Strong Solute-Membrane Affinity. AIChE J. 1993;39(3):434–45.
77. Okada T, Matsuura T. A new transport model for pervaporation. J Memb Sci. 1991;59:133–50.
78. Mehdizadeh H, Dickson JM. Theoretical modification of the surface force-pore flow model for reverse osmosis transport. J Memb Sci. 1989;42:119–45.
79. Gross RJ, Osterle JF. Membrane Transport Characteristics of Ultrafine Capillaries. J Chem Phys. 1968;49(1):228–34.
80. Bowen WR, Mohammad AW, Hilal N. Characterisation of nanofiltration membranes for predictive purposes-use of salts, uncharges solutes and atomic force microscopy. J Memb Sci. 1997;126:91–105.
81. Tung K-L, Jean Y-C, Nanda D, Lee K-R, Hung W-S, Lo C-H, et al. Characterization of multilayer nanofiltration membranes using positron annihilation spectroscopy. J Memb Sci. 2009;343:147–56.
82. Shen M, Keten S, Lueptow RM. Dynamics of water and solute transport in polymeric

reverse osmosis membranes via molecular dynamics simulations. J Memb Sci [Internet]. 2016;506:95–108. Available from: http://dx.doi.org/10.1016/j.memsci.2016.01.051
83. Paul DR. Reformulation of the solution-diffusion theory of reverse osmosis. J Memb Sci. 2004;241(2):371–86.
84. Wang J, Dlamini DS, Mishra AK, Pendergast MTM, Wong MCY, Mamba BB, et al. A critical review of transport through osmotic membranes. J Memb Sci [Internet]. 2014;454:516–37. Available from: http://dx.doi.org/10.1016/j.memsci.2013.12.034
85. Mazid MA. Mechanisms of transport through reverse osmosis membranes. Sep Sci Technol. 1984;19:357–73.
86. Oatley-Radcliffe DL, Williams SR, Barrow MS, Williams PM. Critical appraisal of current nano filtration modelling strategies for seawater desalination and further insights on dielectric exclusion. Desalination [Internet]. 2014;343:154–61. Available from: http://dx.doi.org/10.1016/j.desal.2013.10.001
87. Xie M, Nghiem LD, Price WE, Elimelech M. Relating rejection of trace organic contaminants to membrane properties in forward osmosis : Measurements, modelling and implications. Water Res [Internet]. 2013;49:265–74. Available from: http://dx.doi.org/10.1016/j.watres.2013.11.031
88. Dechadilok P, Deen WM. Hindrance factors for diffusion and convection in pores. Ind Eng Chem Res. 2006;45(21):6953–9.
89. Castrillón SR, Lu X, Shaffer DL. Amine enrichment and poly (ethylene glycol) (PEG) surface modification of thin-film composite forward osmosis membranes for organic fouling control. J Memb Sci [Internet]. 2014;450:331–9. Available from: http://dx.doi.org/10.1016/j.memsci.2013.09.028
90. Arena JT, Manickam SS, Reimund KK, Freeman BD, McCutcheon JR. Solute and water transport in forward osmosis using polydopamine modified thin film composite membranes. DesalinationDES [Internet]. 2014;343:8–16. Available from: http://dx.doi.org/10.1016/j.desal.2014.01.009
91. Arena JT, Mccloskey B, Freeman BD, McCutcheon JR. Surface modification of thin film composite membrane support layers with polydopamine : Enabling use of reverse osmosis membranes in pressure retarded osmosis. J Memb Sci [Internet]. 2011;375(1–2):55–62. Available from: http://dx.doi.org/10.1016/j.memsci.2011.01.060
92. Huang L, McCutcheon JR. Impact of support layer pore size on performance of thin fi lm composite membranes for forward osmosis. J Memb Sci [Internet]. 2015;483:25–33. Available from: http://dx.doi.org/10.1016/j.memsci.2015.01.025
93. Hunt AG, Ewing RP, Sahimi M. Tortuosity in Porous Media: A Critical Review. 2012;
94. Zhang S, Zhang R, Jean YC, Paul DR, Chung T. Cellulose esters for forward osmosis : Characterization of water and salt transport properties and free volume. Polymer (Guildf) [Internet]. 2012;53:2664–72. Available from: http://dx.doi.org/10.1016/j.polymer.2012.04.024
95. Zhang S, Wang KY, Chung T, Jean YC, Chen H. Molecular design of the cellulose ester-based forward osmosis membranes for desalination. Chem Eng Sci [Internet]. 2011;66:2008–18. Available from: http://dx.doi.org/10.1016/j.ces.2011.02.002
96. Matyka M, Khalili A, Koza Z. Tortuosity-porosity relation in porous media flow. Phys Rev E. 2008;78(2):026306.
97. Nightingale E. Phenomenological theory of ion solvation. Effective radii of hydrated ions. J Phys Chem. 1959;63(9):1381–7.

98. Kook S, Swetha CD, Lee J, Lee C, Fane T, Kim IS. Forward Osmosis Membranes under Null-Pressure Condition: Do Hydraulic and Osmotic Pressures Have Identical Nature? Environ Sci Technol [Internet]. 2018;acs.est.7b05265. Available from: http://pubs.acs.org/doi/10.1021/acs.est.7b05265
99. Ghiazza E, Borsani R, Alt F. Innovation in Multistage Flash Evaporator Design for Reduced Energy Consumption and Low Installation Cost. Int Desalin Assoc World Congr Desalin Water Reuse/Tianjin, China. 2013;IDAWC/TIAN13-415.
100. Greenlee LF, Lawler DF, Freeman BD, Marrot B, Moulin P. Reverse osmosis desalination: Water sources, technology, and today's challenges. Water Res [Internet]. 2009;43(9):2317–48. Available from: http://dx.doi.org/10.1016/j.watres.2009.03.010
101. Helal AM, Odeh M. The once-through MSF design. Feasibility for future large capacity desalination plants. Desalination. 2004;166(1–3):25–39.
102. Baig H, Antar MA, Zubair SM. Performance characteristics of a once-through multi-stage flash distillation process. Desalin Water Treat. 2010;13(1–3):174–85.
103. El-Dessouky H, Shaban HI, Al-Ramadan H. Steady-state analysis of multi-stage flash desalination process. Desalination. 1995;103(3):271–87.
104. El-Dessouky HT, Ettouney HM. Fundamentals of Salt Water Desalination. Vol. 1, PhD Proposal. 2002. 691 p.
105. Al-Sofi MKM, Hassan A, Mustafa G, Dalvi A. Nanofiltration as a means of achieving higher TBT of ≥120 °C in MSF. Desalination. 1998;118:123–129.
106. Al-Rawajfeh AE, Fath HES, Mabrouk AA. Integrated Salts Precipitation and Nano-Filtration as Pretreatment of Multistage Flash Desalination System. Heat Transf Eng. 2012;33(March 2015):272–279 ST–Integrated Salts Precipitation and N.
107. Hanshik C, Jeong H, Jeong K, Choi S. Improved productivity of the MSF (multi-stage flashing) desalination plant by increasing the TBT (top brine temperature). Energy [Internet]. 2016;107:683–92. Available from: http://dx.doi.org/10.1016/j.energy.2016.04.028
108. Bandi CS, Uppaluri R, Kumar A. Global optimization of MSF seawater desalination processes. 2016;394:30–43.
109. Chong TH, Sheikholeslami R. Thermodynamics and kinetics for mixed calcium carbonate and calcium sulfate precipitation. Chem Eng Sci. 2001;56(18):5391–400.
110. Hamed OA, Al-Sofi MAK, Imam M, Mustafa GM, Ba Mardouf K, Al-Washmi H. Thermal performance of multi-stage flash distillation plants in Saudi Arabia. Desalination. 2000;128(3):281–92.
111. Hamed OA. Overview of hybrid desalination systems - Current status and future prospects. Desalination. 2005;186(1–3):207–14.
112. Fiorini P, Sciubba E. Thermoeconomic analysis of a MSF desalination plant. Desalination. 2005;182(1–3):39–51.
113. Tanvir MS, Mujtaba IM. Optimisation of design and operation of MSF desalination process using MINLP technique in gPROMS. Desalination. 2008;222(1–3):419–30.
114. Hassan AM, Al-Sofi MAK, Al-Amoudi AS, Jamaluddin ATM, Farooque AM, Rowaili A, et al. A new approach to membrane and thermal seawater desalination processes using nanofiltration membranes (Part 1). Desalination. 1998;118(1–3):35–51.
115. Al-Sofi MAK, Hassan AM, Hamed OA, Dalvi AGI, Kither MNM, Mustafa GM, et al. Optimization of hybridized seawater desalination process. Desalination. 2000;131(1–3):147–56.

116. Hassan AM, Al-Sofi MA, Al-Ajlan AM, Al-Azzaz AA, Al-Mohammadi AS. The New NF-SWRO Operation Increased Significantly UmmLujj SWRO Plant Output and Recovery A.M. Hassan, M. AK. Al-Sofi, A.M. Al-Ajlan, A.A. Al-Azzaz, A.S. Al-Mohammadi, Saudi Arabia.
117. Hassan AM, Al-shail K, Bamardouf K, Al-sulami S, Farooque MA, Al-rubaian A. Operational Performance of an Integrated Nf / Msf. In: International Desalination Association BAH03-037. p. 1–8.
118. Hamed OA, Hassan AM, Al-Shail K, Farooque MA. Performance analysis of a trihybrid NF/RO/MSF desalination plant. Desalin Water Treat. 2009;1(1–3):215–22.
119. Mabrouk ANA, Fath HES. Experimental study of high-performance hybrid NF-MSF desalination pilot test unit driven by renewable energy. Desalin Water Treat [Internet]. 2013;51(37–39):6895–904. Available from: http://www.scopus.com/inward/record.url?eid=2-s2.0-84889639919&partnerID=tZOtx3y1
120. Tusel GF, Rautenbach R, Widua J. Seawater desalination plant "Sirte" - an example for an advanced MSF design. Desalination. 1994;96(1–3):379–96.
121. Zhang Z, Zou L, Aubry C, Jouiad M, Hao Z. Chemically crosslinked rGO laminate film as an ion selective barrier of composite membrane. J Memb Sci [Internet]. 2016;515:204–11. Available from: http://dx.doi.org/10.1016/j.memsci.2016.05.054
122. Baig H, Antar MA, Zubair SM. Performance evaluation of a once-through multi-stage flash distillation system: Impact of brine heater fouling. Energy Convers Manag [Internet]. 2011;52(2):1414–25. Available from: http://dx.doi.org/10.1016/j.enconman.2010.10.004
123. Roy Y, Swaminathan J, Bolaji JO, Lienhard JH. Experimental and modeling analysis of the effect of temperature on nanofiltration of sodium-chloride solution using the NF270 membrane (in preparation). 2018;